BIELEFELD UNIVERSITY

Hybrid molecular and spin dynamics simulations of ensembles of magnetic nanoparticles in viscous matrices

Lisa Teich

Dissertation

Department of Physics
Thin Films and Nanostructures

Gedruckt auf alterungsbeständigem Papier gemäß ISO 9706

Declaration of Authorship

I hereby confirm that I wrote this thesis by myself and used none but the indicated resources.

Bielefeld, November 2015

(Lisa Teich)

Reviewers:
Prof. Dr. Andreas Hütten
Prof. Dr. Christian Schröder

"Given for one instant an intelligence which could comprehend all the forces by which nature is animated and the respective situation of the beings who compose it - an intelligence sufficiently vast to submit those data to analysis - it would embrace in the same formula the movements of the greatest bodies of the universe and those of the lightest atom; for it, nothing would be uncertain and the future, as the past, would be present to its eyes."

P. S. de Laplace, A Philosophical Essay on Probabilities, Dover, New York, 1951

Contents

List of Figures

Publications

- L. Teich, C. Schröder, Hybrid molecular and spin dynamics simulations of ensembles of magnetic nanoparticles for magnetoresistive sensor devices, *Sensors*, 15(11), 28826-28841, **2015**
- L. Teich, C. Schröder, Numerical Investigation of the Magneto-Dynamics of Self-Organizing Nanoparticle Ensembles: a Hybrid Molecular and Spin Dynamics Approach, *IEEE T. Magn.*, 51(11), 7209204, **2015**
- L. Teich, C. Schröder, Hybrid molecular and spin dynamics simulations of gel-based Co nanoparticle dispersions, *20th International Conference on Magnetism*, **July 5-10, 2015**, poster presentation, Barcelona, Spain
- L. Teich, C. Schröder, Numerical Investigation of the Magneto-Dynamics of Self-Organizing Nanoparticle Ensembles: a Hybrid Molecular and Spin Dynamics Approach, *Intermag 2015*, **May 11-15, 2015**, poster presentation, Beijing, China
- L. Teich, D. Kappe, T. Rempel, J. Meyer, C. Schröder, A. Hütten, Modeling of Nanoparticular Magnetoresistive Systems and the Impact on Molecular Recognition, *Sensors*, 15(4), 9251-9264, **2015**
- L. Teich, C. Schröder, J. Meyer, A. Hütten, C. Müller, A. Patel, Efficient Calculation of Low Energy Configurations of Nanoparticle Ensembles for Magnetoresistive Sensor Devices by Means of Stochastic Spin Dynamics and Monte Carlo Methods, *Acta Phys. Pol. A* 127, 374-376, **2015**
- L. Teich, C. Schröder, Investigating the magneto-dynamics of magnetic nanoparticle ensembles by hybrid molecular and spin dynamics simulations, *DPG Spring Meeting*, **March 15-20, 2015**, poster presentation, Berlin, Germany

- L. Teich, C. Schröder, J. Meyer, A. Hütten, C. Müller, A. Patel, Investigation of static, dynamic and temperature-dependent properties of nanoparticle ensembles for magnetoresistive sensor devices by means of Monte Carlo and stochastic spin dynamics simulations, *International Conference on Highly Frustrated Magnetism 2014*, **July 7-11, 2014**, poster presentation, Cambridge, UK

- L. Teich, C. Schröder, J. Meyer, A. Hütten, C. Müller, A. Patel, Efficient Calculation of Low Energy Configurations of Nanoparticle Ensembles for Magnetoresistive Sensor Devices by Means of Stochastic Spin Dynamics and Monte Carlo Methods, *Physics of Magnetism 2014*, **June 23-27, 2014**, poster presentation, Poznán, Poland

1 Introduction

In 2007, the Nobel Prize in Physics was awarded to Albert Fert [1] and Peter Grünberg [2] for the independent discovery of the giant magnetoresistance (GMR) effect in Fe/Cr(001) multilayers and Fe/Cr/Fe(001) trilayers in 1988/89. The GMR effect is characterized by a significant variation of the electrical resistance of a system in the presence of an applied magnetic field. Shortly after its discovery, the technical potential of this effect was recognized and the first GMR-based read heads for hard disk drives were manufactured in 1997, not even a decade after the discovery of the effect. At the same time, the GMR effect was extended to granular systems consisting of magnetic granules that are embedded in metallic matrices [3, 4] opening up further possibilities for sensor applications. Recently, it has been shown in [5, 6] that the GMR effect can also be observed in nanoparticle-based systems that consist of magnetic particles that are immersed in conductive gel matrices. Because of their high GMR effect amplitude and the mechanical properties of the gel matrix printable, low-cost, magnetoresistive sensor devices can be developed.

In general, the crucial issue of the development of an arbitrary sensor is to maximize the sensor sensitivity, i.e. to maximize the output quantity of the sensor to a given input quantity. In the case of a nanoparticle-based GMR sensor, an optimal particle material, particle concentration and size distribution as well as an optimal matrix material must be found in order to obtain the maximum GMR effect amplitude and therefore the maximum sensor sensitivity. Information about the properties of the matrix material and the topological particle configuration can precisely be obtained experimentally whereas the magnetic microstructure, i.e. the orientations of the single magnetic moments, cannot be revealed experimentally. At this point, numerical simulations play a critical role and provide the missing information.

In this thesis, a novel method for the simulation of magnetically interacting nanoparticles in liquid environments is presented. With this method, the self-assembly process of the magnetic particles can be investigated step by step and at the same time the

orientations of all the single magnetic moments of the system can be observed. Therefore, the two relevant types of degrees of freedom, i.e. the magnetic and the mechanical degrees of freedom, are addressed by two different highly-specialized algorithms that are combined to one hybrid simulation method. In general, the problem under consideration is described by three coupled sets of equations of motion 1.1-1.3.

$$m_i \frac{d\mathbf{v}_i(t)}{dt} = -\nabla_{\mathbf{r}_i,\mathbf{S}_i}\mathcal{H}_{DD}\left(\mathbf{r}_1,...,\mathbf{r}_N,\mathbf{S}_1,...,\mathbf{S}_N\right) - \mathbf{F}_{visc}\left(\mathbf{v}_1,...,\mathbf{v}_N\right) - \nabla_{\mathbf{r}_i}\mathcal{H}_{WCA} \quad (1.1)$$

$$\frac{d\mathbf{r}_i(t)}{dt} = \mathbf{v}_i(t) \quad (1.2)$$

$$\hbar\frac{\partial\mathbf{S}_i}{\partial t} = \mathbf{H}_{eff}\left(\mathbf{r}_1,...,\mathbf{r}_N,\mathbf{S}_1,...,\mathbf{S}_N\right)\times\mathbf{S}_i - \lambda\left(\mathbf{H}_{eff}\left(\mathbf{r}_1,...,\mathbf{r}_N,\mathbf{S}_1,...,\mathbf{S}_N\right)\times\mathbf{S}_i\right)\times\mathbf{S}_i \quad (1.3)$$

The mechanical equations of motion are provided by equations 1.1 and 1.2. In these equations, the motion of the nanoparticles which is characterized by the particle masses $\mathbf{m}_i$, velocities $\mathbf{v}_i$, and positions $\mathbf{r}_i$ is induced by magnetic dipole-dipole energy contributions $\mathcal{H}_{DD}$ of the magnetic moments $\mathbf{S}_i$ of the particles that are counteracted by viscous drag forces F_{visc} and hard particle interactions $\mathcal{H}_{WCA}$. At the same time, the magnetic moment orientations of the particles change due to the effective magnetic field $\mathbf{H}_{eff}$ that is generated by the magnetic dipole-dipole interactions between the particles which is reflected by equation 1.3. Inherently, these equations of motion must be solved simultaneously. However, it can be shown that due to the large difference between the mechanical and the magnetic relaxation times, the simulation can be divided into consecutive steps.

This thesis is organized as follows. In chapter 2, a broad introduction into the topic area of nanoparticle-based magnetoresistive sensor devices is given. In the following chapter 3, the numerical methods that are used for the hybrid simulation method, i.e. classical spin dynamics and classical molecular dynamics are introduced in general. At the same time, particular features that must be considered in the context of this thesis are demonstrated. In addition to that experimental systems are presented and a route for the determination of model systems is proposed. On the one hand, the particle positions and sizes can be determined by three-dimensional reconstruction techniques while, on the other hand, model systems with inferior complexity can be deduced from these real systems as presented in chapter 4.

At the beginning of the investigations for this thesis, preliminary spin dynamics simulations of real and model structures have been carried out in order to get an impression

of the magnetic structure of disordered ensembles of magnetic nanoparticles. In doing so, it has been shown that the topological disorder causes geometric frustration leading to a trapping of the magnetic configurations in local energy minima. To increase the efficiency of the calculation of low energy configurations, an experimentally inspired demagnetization protocol has been applied *in silico*. This approach is presented in chapter 5 of this thesis.

Subsequently, the key issue of this work is addressed in chapter 6. In this chapter, the novel, hybrid simulation method is explained in detail alongside the theoretical foundations of the separation of the degrees of freedom that has been introduced above. In the following chapter 7 this method is applied to a model structure that has been designed to mimic real, experimental systems according to chapter 4. If one compares the experimental situation to the theoretical setting, the hybrid simulation of the magnetic particles in the viscous matrix corresponds to the preparation stage of the magnetoresistive sensor system. At this stage, the matrix material is liquid and the particles are free to move. Hence, the magnetoresistive properties are defined at this stage but the actual measuring task is performed at a different stage. After the self-assembly of the magnetic nanoparticles in the liquid matrix is completed, the matrix is gelatinized and the particle structure as well as the magnetoresistive properties are preserved and can be used to precisely detect changes in the magnetic structure. At this second stage, the measuring stage, the magnetic particles are no longer free to move and only the magnetic moment orientations can change. If one transfers this situation to the simulation, the measuring stage corresponds to a situation with frozen mechanical degrees of freedom and active magnetic degrees of freedom. Thus, in order to simulate the measuring stage, the mechanical degrees of freedom, and therefore the molecular dynamics part of the method must be switched off. In chapter 7, the GMR estimation by means of pure spin dynamics simulations is shown for the model structure.

This thesis concludes with an overview of numerically investigated systems that show noticeable properties which makes them interesting candidates for future experimental investigations. In addition to the two-dimensional arrays of particles for nanoparticle-based sensor applications, small, three-dimensional particle ensembles with interesting properties are presented.

2 Magnetoresistive systems

Magnetoresistive systems offer an interesting playground for experimental and theoretical investigations as well as promising technical applications. This chapter introduces the giant magnetoresistance (GMR) effect in multilayer systems and granular gel-based systems together with the relevant features of magnetic nanoparticles that are crucial for gel-based GMR systems. In conclusion, basic operating principles of GMR sensor devices are presented in the context of the detection of arbitrary biomolecules.

2.1 Magnetic nanoparticles

Magnetic materials can be classified according to two main aspects. First, they can be categorized by their geometric dimension and form, i.e. from large-scale bulk materials over microscale thin films and particles down to magnetic molecules. Second, magnetic materials can be divided into different substantial classes detached from their shape and scale. An overview of the most important classes of magnetic order in solids is given in figure 2.1. In regular magnetic solid materials, with the exception of a few particular cases, the magnetic behavior is dominated by permanent magnetic moments that can be attributed to all or a subset of the ions in the solid. Differences between the types of magnetism are related to the internal arrangement of these magnetic moments. This holds true for the cases of diamagnetism, paramagnetism, ferromagnetism, antiferromagnetism, and ferrimagnetism in regular solids. If amorphous and disordered solids are also taken into account, new types of magnetism must be considered. Amorphous solids are characterized by the absence of equivalent atomic sites whereas disordered solids can be considered as systems with regular lattices with randomly placed atoms on the crystal lattice sites [7].

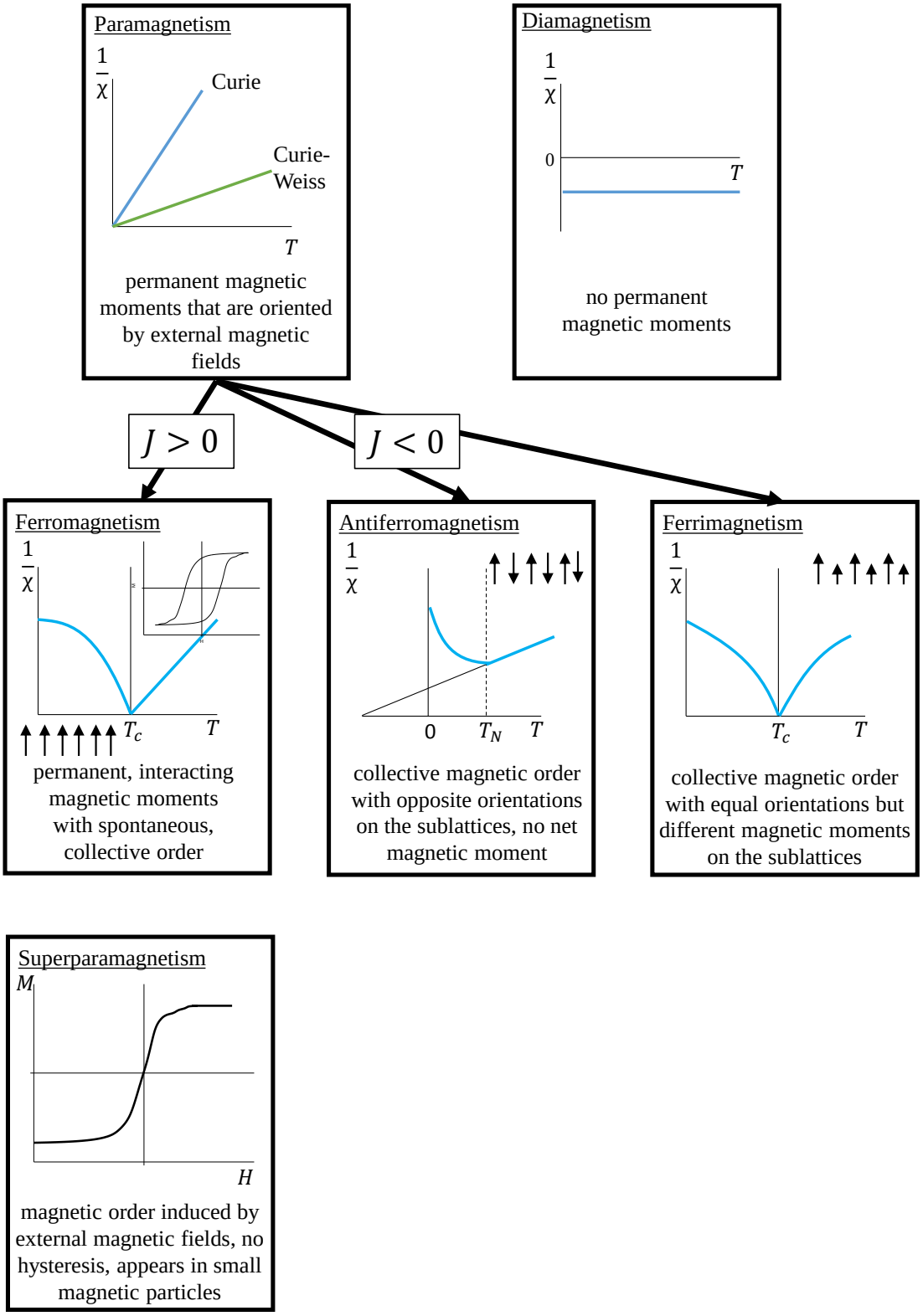

FIGURE 2.1: Magnetic family tree: overview of the different classes of magnetic order. The temperature-dependent inverse susceptibility is shown for paramagnetic, diamagnetic, ferromagnetic, antiferromagnetic and ferrimagnetic materials. Ferromagnetic materials are characterized by a hysteresis loop, i.e. the field-dependent magnetization depends on the history of the system. For superparamagnetic materials, this hysteretic behavior vanishes. This figure is adapted from [7, 8].

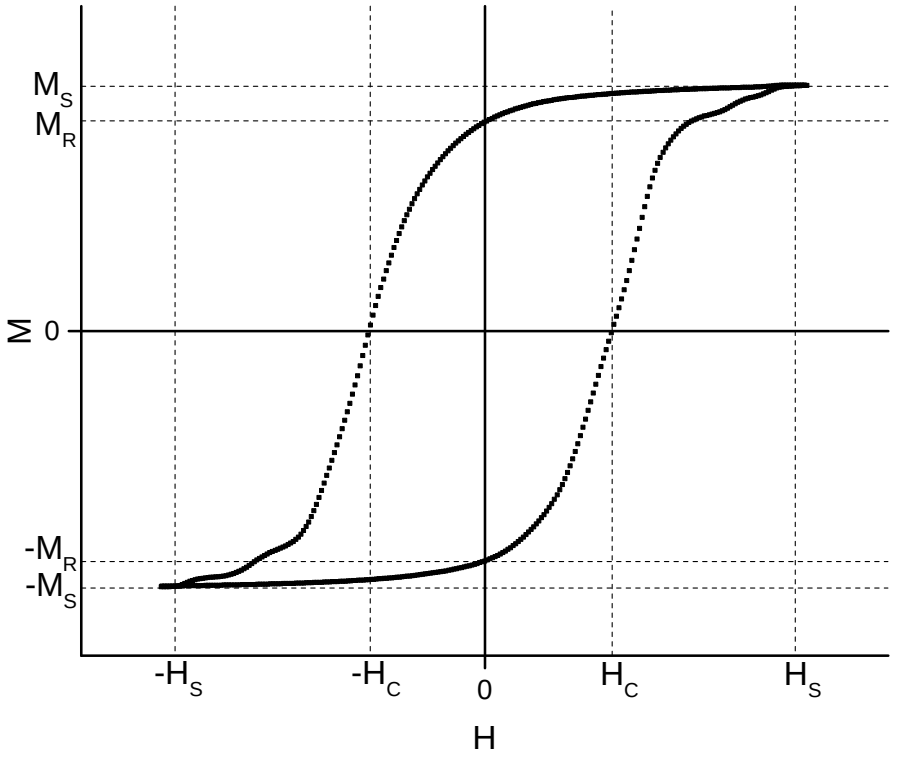

FIGURE 2.2: Exemplary magnetic hysteresis loop with the characteristic quantities saturation magnetization M_S and field H_S, remanent magnetization M_R and coercive field H_C.

Within the classes of magnetic materials, weak (diamagnetic and paramagnetic) and strong (ferromagnetic, antiferromagnetic, ferrimagnetic) materials can be distinguished. In zero external magnetic field, diamagnetic and paramagnetic materials do not have a net magnetic moment and thus no net magnetization, i.e. no magnetic moment per unit volume at any temperature. A spontaneous zero-field magnetization can only be observed in strong magnetic materials below a characteristic temperature, i.e. the Curie temperature T_C for ferromagnetic and the Néel temperature T_N for paramagnetic materials. Due to competing interactions of the magnetic moments, ferromagnetic materials are broken up into magnetic domains. Magnetic domains are homogeneously magnetized regions of the magnetic material that are separated by so-called domain walls. Domain walls are regions of finite thickness in which the magnetization gradually changes from one domain to another. In time-dependent magnetic fields, hysteretic behavior arises. Hysteresis loops are characterized by the quantities saturation magnetization (M_S) and field (H_S), remanent magnetization (M_R) at zero external field, and coercive field (H_C) at zero magnetization as shown in figure 2.2.

Comparing magnetic nanoparticles and magnetic bulk materials, magnetic nanoparticles have special characteristics. For the modeling of single particles and small ensembles where the atomic structure is of great importance, an atomistic treatment is favored.

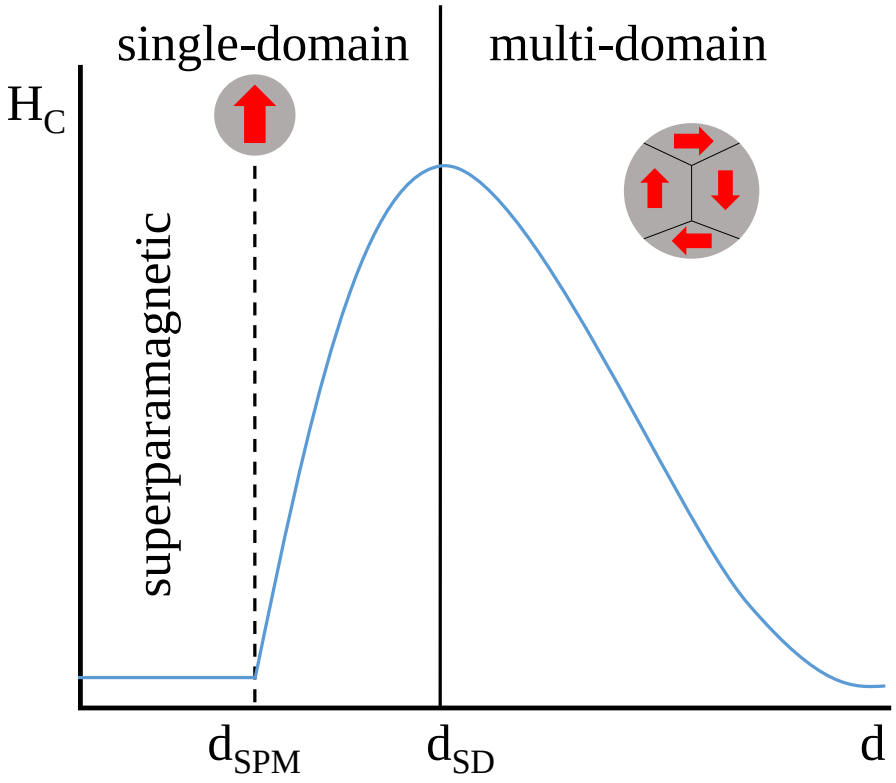

FIGURE 2.3: Size-dependence of the coercive field of magnetic particles. Below a critical particle size d_{SD}, a transition between a multi-domain and a single-domain state occurs. By further increasing of the particle size below a second critical size d_{SPM}, the particle becomes superparamagnetic. This figure is adapted from [12, 13].

Therefore, the magnetic nanoparticles are described as assemblies of strongly interacting magnetic moments of the atoms they are composed of. For larger ensembles, an atomistic treatment becomes elaborate because each nanoparticle can consist of up to approximately 10^5 atoms. Thus, the particles can be treated as a continuous medium with a small size. The differences between the behavior of magnetic nanoparticles and bulk material can be taken into account by means of finite size effects. The most simple approximation which holds true for many reasonable particle sizes is the representation of a single magnetic nanoparticle as a uniformly magnetized, hard, ferromagnetic body. [9–11]

The coercive field H_C is the most sensitive property of a ferromagnetic material. Hence, it is one of the most important criteria for technical applications. The coercive field increases with a decreasing size of the magnetic body as it is shown in figure 2.3. Below a critical size d_{SD} the coercive field decreases with further decreasing particle size. This behavior is due to the fact that the energy that is required for a further domain formation is larger than the energy savings due to the stray field minimization by the domains. Hence, at d_{SD} a transition between a multi-domain and a single-domain state of the particle occurs. The critical size d_{SD} can be estimated according to equation 2.1.

$$d_{SD} = \frac{2 \cdot \sqrt{A_{ex} \cdot K}}{M_S^2} \tag{2.1}$$

In this equation, A_{ex} represents the exchange stiffness constant whereas K represents the anisotropy constant of the material. Below d_{SD}, the particle consists of one single magnetic domain carrying one net magnetic macro moment. The magnetization of a particle below d_{SD} can only change by means of a rotation of the macro moment [14, 15]. By further decreasing the particle size, another critical point is reached, i.e. the superparamagnetic limit d_{SPM}. Below d_{SPM}, the anisotropy energy becomes comparable to the thermal energy $k_B \cdot T$. Hence, the macro moment fluctuates due to thermal agitation. In a superparamagnetic particle, the characteristic relaxation time becomes very small and no hysteretic behavior can be observed as it is shown in figure 2.1. [12]

2.1.1 Magnetic interactions

Magnetic order is established by various types of interactions between the magnetic components of a system. Ferromagnetic samples are characterized by their spontaneous magnetization due to an inherent magnetic order. This inherent magnetic order originates from interactions of magnetic moments on the microscale and can be extended to describe macroscopic, interacting magnetic moments.

Exchange interaction

Ferromagnetic order must be explained in the framework of quantum mechanics. In the classical picture, magnetic moments interact by means of magnetic dipole fields but these fields are too small by orders of magnitude to explain spontaneous ferromagnetic order. Instead of the magnetic dipole-dipole interaction, the so-called exchange interaction which is a purely quantum mechanical effect was identified as the source of ferromagnetic order. Exchange interaction is the result of the Coulomb interaction of adjacent electrons and the Pauli exclusion principle which states that two electrons cannot be in the same quantum state. Exchange interaction can be described by means of the Heisenberg Hamiltonian.

$$\mathcal{H} = -2J\hat{\mathbf{S}}_i \cdot \hat{\mathbf{S}}_j \tag{2.2}$$

In this equation, $\hat{\mathbf{S}}_i$ and $\hat{\mathbf{S}}_j$ are the dimensionless spin operators and J is the exchange constant given in units of energy. For positive values of J, adjacent spins prefer a

parallel (ferromagnetic) orientation whereas for negative values of J an antiparallel (antiferromagnetic) orientation is preferred. The atoms of a solid are arranged in a lattice structure. In this case, the Hamiltonian can be calculated by summing up the contributions from equation 2.2 for all pairs of atoms in the system.

$$\mathcal{H} = -2 \sum_{i>j} J_{ij} \mathbf{S}_i \cdot \mathbf{S}_j \tag{2.3}$$

Besides this direct exchange other types of exchange interactions exist. For small distances between the magnetic moments, an overlap of their wave functions results in a strong and short-ranged coupling, i.e. the direct exchange interaction. If the exchange interaction is mediated by itinerant electrons or non-magnetic ions over larger distances the mechanism is called indirect exchange interaction. Indirect exchange can lead to sophisticated coupling characteristics such as oscillating coupling energies as described in chapter 2.2.2. For systems of magnetic nanoparticles that consist of thousands of atoms that are overlain by one magnetic macro moment, exchange interactions do not have to be taken into account. Even though exchange interactions play a crucial role for ferromagnetic order on the atomic scale, the interactions between magnetic particles are dominated by long-range interactions, first and foremost the magnetic dipole-dipole interaction. [8, 16]

Magnetic dipole-dipole interaction

Two main contributions dominate the energy of ferromagnetic materials. First, electrostatic effects like exchange interactions (see chapter 2.1.1) and second, magnetostatic effects. Magnetostatic effects account for the self-energy of the interaction of a ferromagnet with the magnetic field it creates by itself as well as the interaction of the ferromagnetic body with externally applied magnetic fields. Comparing electrostatic and magnetostatic effects, magnetostatic effects are much weaker. At the same time, they are long-range effects and nevertheless crucial for the formation of magnetic domains, magnetization processes, and the interaction of macroscopic and microscopic magnetic objects.
A single magnetic dipole $\mathbf{m}$ which is placed in a uniform magnetic field with a magnetic flux density $\mathbf{B}$ experiences a torque but no net force. This torque τ can be calculated according to the following equation.

$$\tau = \mathbf{m} \times \mathbf{B} \tag{2.4}$$

The Zeeman energy E_{Zee} represents the energy of the magnetic moment in the external field.

$$E_{\mathrm{Zee}} = -\mathbf{m} \cdot \mathbf{B} \tag{2.5}$$

This potential energy does not depend on the position of the magnetic moment. It reaches its minimum value for a parallel orientation of the magnetic moment and the external magnetic field. For the case of a non-uniform magnetic field $\mathbf{B}(\mathbf{r})$, a net force $\mathbf{F}$ occurs which depends on the position of the magnetic moment $\mathbf{r}$.

$$\mathbf{F} = \nabla (\mathbf{m} \cdot \mathbf{B}(\mathbf{r})) \tag{2.6}$$

Magnetic dipole-dipole interaction occurs when two magnetic particles interact with each other by their magnetic dipole fields. Considering two magnetic dipole moments with parallel orientations $\mathbf{m}_i = \mathbf{m}_j$ at positions $\mathbf{r}_i$ and $\mathbf{r}_j$, the magnetic dipole-dipole energy can be interpreted as the energy of $\mathbf{m}_i$ in the field $\mathbf{B}_{ji}$ that is created by $\mathbf{m}_j$. This applies in reverse as well.

$$E_{\mathrm{DD}} = -\mathbf{m}_i \cdot \mathbf{B}_{ji} = -\mathbf{m}_j \cdot \mathbf{B}_{ij} \tag{2.7}$$

The field that is produced by a magnetic dipole $\mathbf{m}$ can be described as a function of distance by means of the following equation.

$$\mathbf{B}(\mathbf{r}) = \frac{\mu_0}{4\pi r^2} \frac{3\mathbf{r}(\mathbf{m} \cdot \mathbf{r}) - \mathbf{m}r^2}{r^3} \tag{2.8}$$

In equation 2.8, $\mathbf{r}$ represents the position at which the magnetic field is evaluated, r is the absolute value of $\mathbf{r}$ whereas μ_0 is the magnetic field constant and $\mathbf{m}$ represents the magnetic moment that produces the magnetic field $\mathbf{B}$. By replacing the magnetic field in equation 2.7 by equation 2.8, the energy and thus the force between two interacting magnetic moments due to their magnetic dipole fields can be calculated.

$$\mathbf{F}_{ij} = \frac{3\mu_0}{4\pi r^4} \left[\left(\frac{\mathbf{r}}{r} \times \mathbf{m}_i \right) \times \mathbf{m}_j + \left(\frac{\mathbf{r}}{r} \times \mathbf{m}_j \right) \times \mathbf{m}_i - 2\frac{\mathbf{r}}{r} \left(\left(\frac{\mathbf{r}}{r} \times \mathbf{m}_i \right) \cdot \left(\frac{\mathbf{r}}{r} \times \mathbf{m}_j \right) \right) \right] \tag{2.9}$$

2.1.2 Geometric frustration

The term frustration was coined by G. Toulouse in 1977 to describe the inability to satisfy pairwise interactions around a closed loop [17]. This inability occurs due to structural disorder and can be introduced in the context of a system that consists of three magnetic moments that are arranged on a triangular lattice as it is shown in figure 2.4(b). Therefore, the magnetic moments are assumed to follow the Ising model, i.e. the orientations of the magnetic moments are restricted to the up and down directions [18]. In addition to that, an antiferromagnetic coupling is assumed. Thus, a minimum value of the interaction energy of one pair of magnetic moments is achieved for an antiparallel alignment. Placing the first pair of magnetic moments in a way that they reach the minimum interaction energy results in a system in which the third magnetic moment can no longer be placed in a way that its orientation is antiparallel to the other two moment orientations. Hence, the system is called frustrated [19]. The degeneracy of the magnetic ground states leads to the magnetic analogs of liquids and ices namely spin liquids and spin ices. It was shown that the ordering of the protons in water ice is locally equivalent to the physics of a frustrated ensemble of magnetic Ising-type spins that are arranged on a lattice of vertex-sharing tetrahedra [20]. This structure is called pyrochlore lattice. In frustrated systems, even small perturbations can cause instabilities and thus the emergence of novel phenomena. It was reported in [21] that magnetic monopoles exist in the form of quasi-particles that are free to move in condensed matter as a direct result of frustration as already proposed by P. Dirac in 1931 [22]. Due to the emerging phenomena, frustrated magnetic systems have been intensively studied over the last decades. Magnetic frustration is usually studied in atomic systems but it can nevertheless be observed in larger systems. Magnetic nanoparticles with diameters up to a certain value (see figure 2.3) can be considered as homogeneously magnetized spheres that carry one single magnetic macro moment. Hence, systems of magnetic nanoparticles with structural disorder have magnetic properties that are analog to the properties of atomistic systems. Due to the relatively large distances between the particles in these systems, the leading interaction between the particles is the magnetic dipole-dipole interaction. Thus, the term *magnetic dipole glass* was coined. As described in [23], the ground states of systems of magnetic dipoles are strongly degenerated. This degeneracy occurs in systems with particles that are fixed on regular lattices [24], randomly placed particles [25], and in magnetic fluids [23]. [26]

2.1.3 Magnetic properties of nanoparticle ensembles

Ensembles of magnetic nanoparticles can be organized by means of undirected self-assembly, i.e. due to their intrinsic interactions [27] or they can be organized with

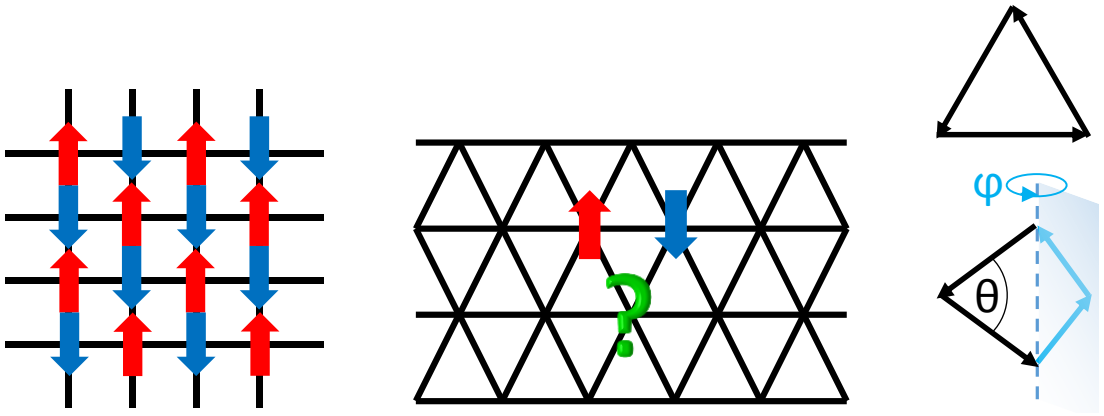

(a) (b) (c)

FIGURE 2.4: For an unfrustrated system such as the square lattice with antiferromagnetically coupled spins (a), all interaction energies can be minimized at the same time. However, the simultaneous minimization of all interaction energies is not possible on the triangular lattice in the Ising picture resulting in a frustrated system (b). In the Heisenberg picture, three spins form a unique ground state whereas four spins represent a system with a multitude of ground states depending on the two degrees of freedom, φ and θ (c). (The figure is adapted from [19])

external forces such as external magnetic fields which corresponds to a directed self-assembly. These organized assemblies show complex, collective properties which open up new perspectives for different fields of research such as information storage and sensor technologies. Phenomena that are restricted to nanostructured materials include magnetoresistance effects, exchange bias, and spin injection. Conventional nanostructured materials are thin film or multilayer systems which have been intensively studied in the past. Besides thin film systems, particle composites on the nanoscale show promising features. The effects that occur in nanoparticle-based systems are driven by particle-particle, particle-field interactions, and the structural order that results from the assembly process. The dominating mechanism in ensembles of magnetic nanoparticles is the magnetic dipole-dipole interaction (see chapter 2.1.1) which decays as $\frac{1}{r^3}$, with r being the average distance between adjacent particles. Hence, the magnetic dipole-dipole interaction is the main cause of new effects in nanostructured materials [28, 29]. For example, in nanoparticle-based systems, the magnetic dipole-dipole interaction causes the formation of ring structures in order to form flux-closed structures as it has been shown in [30] (see figure 2.5). In these ring structures, the magnetization is forced to be circular which leads to a stable flux closure mode and thereby interesting properties for technical applications in the field of magnetic recording [31–33]. In addition to ring-like structures, magnetic particles in liquid matrices form chains, chain networks, densely packed clusters and fractal structures [34–36]. [12]

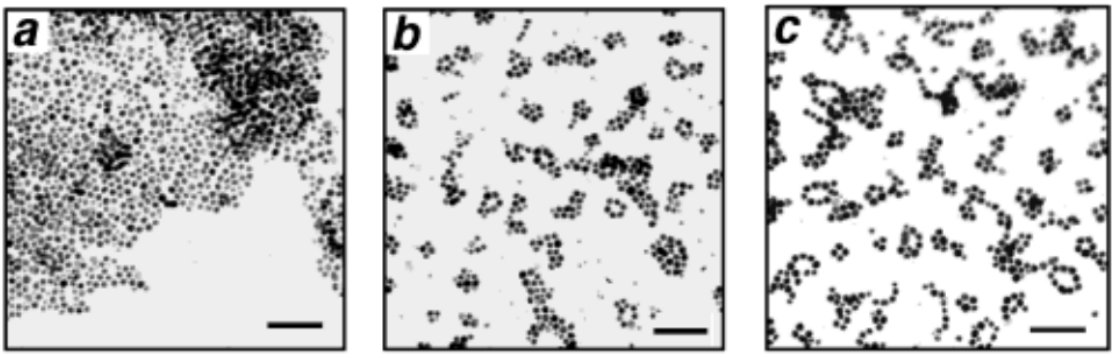

FIGURE 2.5: TEM images (Philips EM-400, 80 kV) of $27 \pm 4nm$ Co particles dispersed in toluene at different concentrations of C-undecylcalix[4]resorcinarene: (a) $< 10^{-6}M$, (b) $10^{-5}M$, (c) $< 10^{-3}M$. Scale bar = $200nm$. Reprinted with permission from [30] ©2002 American Chemical Society.

2.2 Magnetoresistance and related effects

Magnetoresistance is a material's property to change its electrical resistance in the presence of an external magnetic field. Various different magnetoresistance effects can be distinguished due to their different origins, among them the well-known tunneling magnetoresistance (TMR) and the giant magnetoresistance (GMR) effect. Ferromagnetic materials exhibit a long-range order of uncompensated spins and hence a difference in the density of states of spin-up and spin-down electrons leading to different conductivities. Thus, electron transport in ferromagnetic materials is spin-dependent and can be treated in the framework of the two current model by Mott [37, 38]. These observations finally led to the discovery of the GMR, the most prominent phenomenon of spin-dependent transport.

2.2.1 Giant magnetoresistance (GMR) effect

Independently discovered by A. Fert [1] and P. Grünberg [2] in 1988 and 1989, a significant change of the electrical resistance can be observed in ferromagnetic multilayer systems with non-magnetic spacer layers. The change in resistance can be induced by the application of an external magnetic field to change the relative orientation of the ferromagnetic layers. Thus, the electron transport in multilayer systems can be controlled by changing the magnetization directions in the layers. Two characteristic properties lead to GMR in multilayer systems. First, the non-magnetic spacer layer weakens the coupling between the ferromagnetic layers. Hence, the alignment of the layer magnetizations can be adjusted more easily by means of an external magnetic field. Second, the layers are very thin and so the carrier electrons feel a change in the magnetization direction of the layers. The GMR ratio or briefly GMR can be determined by the minimum

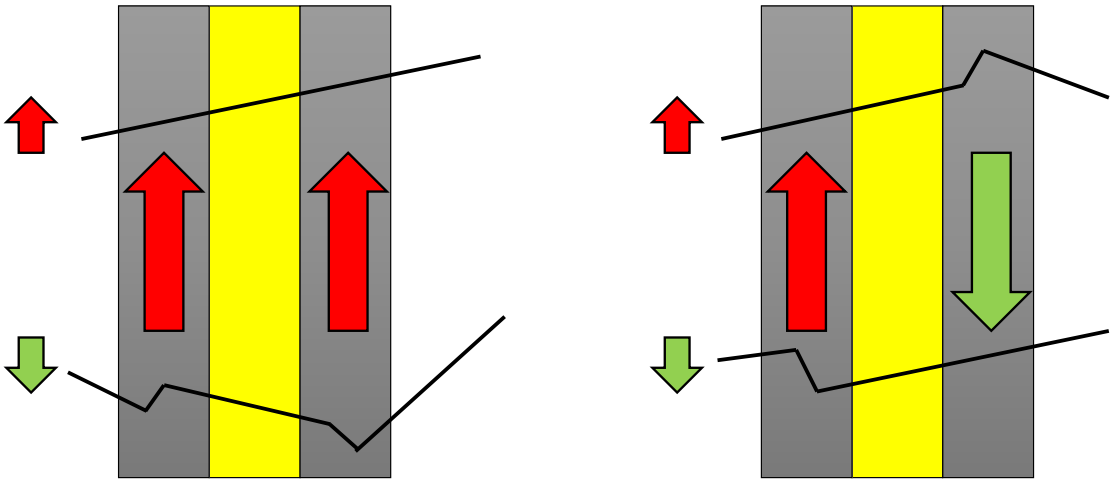

FIGURE 2.6: Schematic representation of the spin-dependent transport of electrons in multilayer GMR systems consisting of two ferromagnetic layers (grey) that are separated by a non-magnetic spacer lacer (yellow). For a parallel alignment of the ferromagnetic layers (left), one of the two currents can pass the layers easily, whereas the other current is inhibited by both layers. For an antiparallel alignment of the layers (right), both currents are scattered at one of the layers, resulting in larger total resistance than for the antiparallel alignment.

and maximum values of the electrical resistance, R_{min} and R_{max} that are obtained at the coercive field and at the magnetic field in saturation. [39, 40]

$$\mathrm{GMR} = \frac{R_{max} - R_{min}}{R_{min}} \tag{2.10}$$

Thus, the GMR effect originates from the spin-dependent scattering of the conduction electrons. A phenomenological explanation can be found within Mott's two-current model [37, 38]. This model states that conduction in metals can be expressed via summation of two conduction channels that correspond to the spin-up and spin-down electrons. These two channels are mostly independent. In addition to that, the scattering of the electrons depends on the relative orientation of the conduction electron spin and the magnetization of the material resulting in different scattering rates for the spin-up and the spin-down electrons. As it is shown in figure 2.6, for the case of a parallel alignment of the magnetic layers of a multilayer system one type of electron can pass without being scattered whereas the other electron type is strongly scattered at both magnetic layers. For the case of an antiparallel alignment of the layer magnetizations, both electron types can pass one layer unscattered and are strongly scattered at the other layer. As a result, the total electrical resistance is low for the parallel alignment and high for the antiparallel alignment of the ferromagnetic layers.

According to the direction of the current, current-in-plane (CIP) and current-perpendicular-to-plane (CPP) GMR systems can be distinguished. The effect amplitudes in CPP system are typically larger than in CIP systems (170% measured in Co/Cu CPP system compared to 108% measured in Fe/Cr CIP system). [40]

2.2.2 Interlayer exchange coupling

For technical applications it is important to adjust the sign of the coupling between the magnetic layers. The mechanism that underlies the coupling between the ferromagnetic layers is called interlayer exchange coupling (IEC) and was discovered by Grünberg et al. in 1986 [41] and continued by Parkin et al. [42]. This type of coupling is mediated by means of the electrons of the non-magnetic spacer layer. The sign of the coupling oscillates with the thickness of the spacer layer as shown in figure 2.7. The IEC is closely related to the Rudermann-Kittel-Kasuya-Yosida (RKKY) interaction [43–45] which is an effect between magnetic impurities in a non-magnetic host [46, 47]. However, a theoretical explanation within the RKKY picture fails because of the intrinsic limitations of the model. Newer models which are based on quantum well energy were applied successfully [48, 49].

2.2.3 Granular GMR effect

The occurence of GMR is not restricted to multilayer systems. It can also be observed in granular systems of magnetic grains that are immersed in a non-magnetic metallic matrix. This effect is called granular GMR effect and was discovered independently by Xiao et al. [3] and Berkowitz et al. [4] in 1992. Again, the granular GMR effect can be explained in the framework of Mott's two current model. In zero external field, the magnetic moments of the grains are statistically distributed resulting in the maximum value of the electrical resistance R_{max} due to the strong spin-dependent scattering. In contrast to that, an external magnetic field forces the magnetic moments in its direction which leads to a significantly reduced resistance R_{min}. Hence, the characteristic GMR curves can be obtained by measuring the electrical resistance of a system in the presence of a time-dependent magnetic field. This is exemplarily shown in figure 2.8 together with the corresponding magnetization curve. Besides the possibility of obtaining information about the GMR experimentally, it is possible to calculate qualitative GMR curves. The underlying phenomenological theory implies that the GMR ratio is determined by the square of the average angle between the direction of the magnetic moments of the grains and the external magnetic field direction [50].

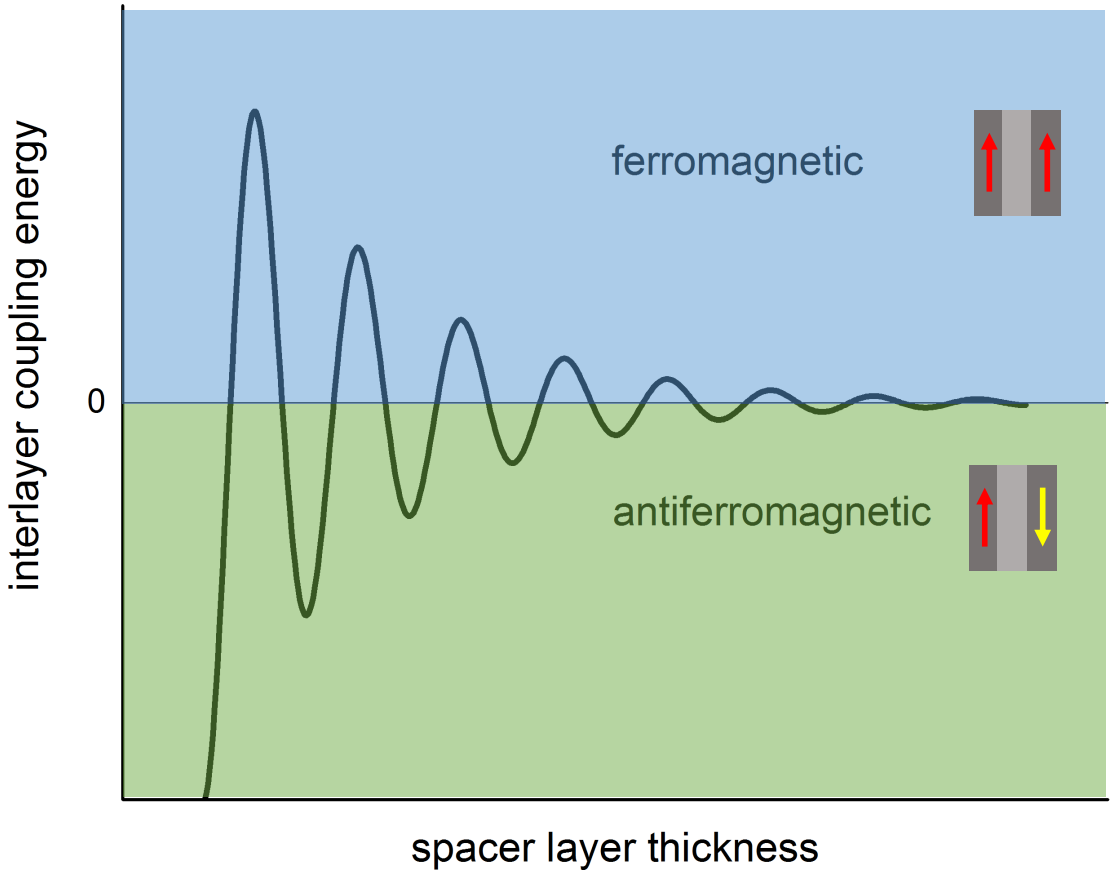

FIGURE 2.7: Schematic representation of the oscillating interlayer exchange coupling energy. The sign of this interaction of ferromagnetic layers that are separated by a non-magnetic spacer layer varies with the thickness of the spacer layer [47].

$$\mathrm{GMR} \propto 1 - \langle \cos\theta \rangle^2 \tag{2.11}$$

In granular systems, $\langle \cos\theta \rangle^2$ can be expressed in terms of the magnetization M and the saturation magnetization M_S [3].

$$\mathrm{GMR} \propto 1 - \left(\frac{M}{M_S}\right)^2 \tag{2.12}$$

Finally, the GMR effect amplitude A_{GMR} is introduced as a proportionality constant.

$$\mathrm{GMR} = A_{\mathrm{GMR}} \left[1 - \left(\frac{M}{M_S}\right)^2\right] \tag{2.13}$$

The GMR effect amplitude A_{GMR} can be determined by means of quantum mechanical techniques, such as the so-called tight binding Korringa-Kohn-Rostoker method [51, 52] or it can be measured experimentally [53]. The occurence of the granular GMR effect is

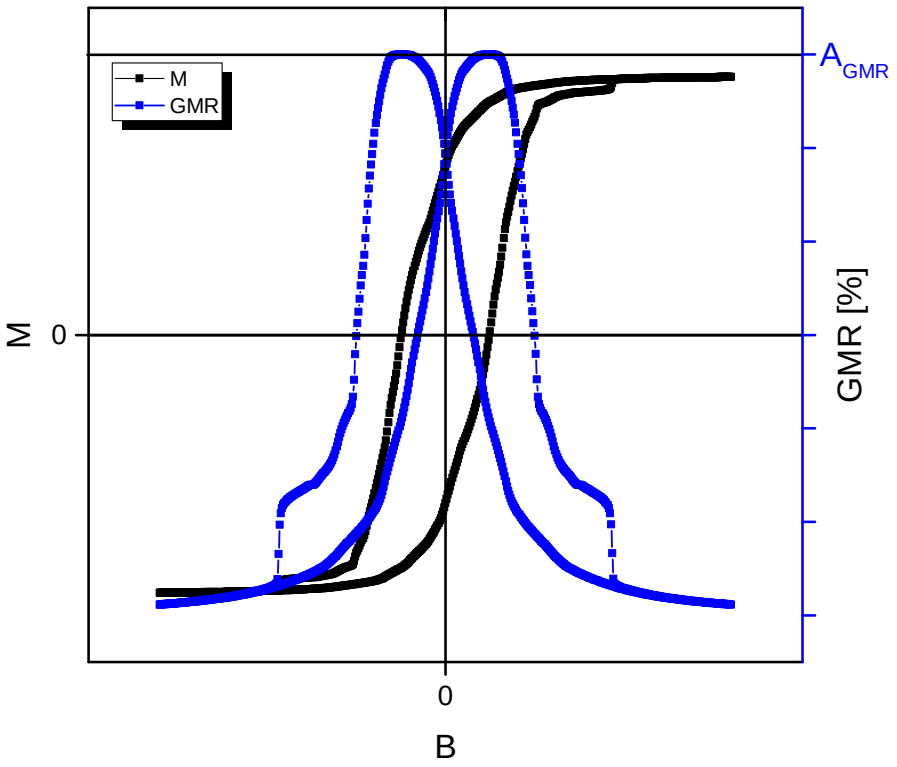

FIGURE 2.8: Qualitative GMR curve (blue) with associated magnetization curve (black). The GMR curve is calculated from a simulated magnetization curve of a nanoparticle ensemble by means of equation 2.13.

not only restricted to systems of magnetic grains in non-magnetic metallic matrices. It can also be observed for magnetic nanoparticles that are immersed in conductive gel-like matrices [5].

Measurement of GMR curves of particle-gel systems

A method to measure GMR curves of systems that consist of magnetic nanoparticles that are embedded in conductive gel matrices is presented in [6]. For this method, the particle-gel sample is prepared in a sample vessel on a silicon dioxide wafer. The sample is then contacted from above with four needles that are made of gold. The needles form a line as it is shown in figure 2.9. To determine the magnetoresistance of the system a magneto-transport measurement is performed. Therefore, a current is introduced into the system by means of the outer two needles. At the same time, the resulting voltage is measured with the two inner needles which allows to determine the resistance. Because the electrical resistance varies with the degree of the magnetic order, the measurement is performed in a time-dependent external magnetic field that is applied in the plane of the particle-gel system, parallel to the current. Realized by a computer-controlled electromagnet, starting from a maximum negative absolute value of the magnetic field,

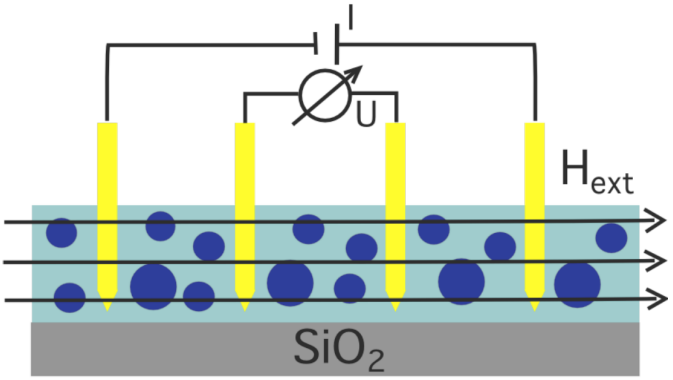

FIGURE 2.9: Schematic representation of the four point probe setup that is used in [6] to measure the GMR curves of samples that consist of magnetic nanoparticles in conductive gel matrices. The sample is prepared on a silicon dioxide wafer and contacted by four gold needles from above. A current is introduced via the two outer needles and the resulting voltage is measured by the two inner needles. The magnetoresistance is then determined by measuring the resistance of the system in a time-dependent external magnetic field. This figure is reproduced from [6].

the field is ramped up to a maximum positive value and back down to the maximum negative value.

2.3 Magnetoresistive sensor systems

Conventional GMR sensors consist of thin ferromagnetic layers that are separated by non-magnetic, conductive spacer layers. The ferromagnetic layer consists either of a magnetic transition metal (*Fe*, *Co*, *Ni*) or of one of their alloys. The non-magnetic spacer usually is a non-ferromagnetic transition metal or a noble metal such as *Cr*, *Mo*, *Ru*, *Cu*, *Ag* or *Au*. The thickness of each layer can be found in the range of several nanometers. Due to the interlayer exchange coupling (see chapter 2.2.2), the sign of the coupling between two ferromagnetic layers can be adjusted by the thickness of the non-magnetic spacer. Usually, the spacer thickness is chosen in a way that the ferromagnetic layers have a spontaneous antiferromagnetic alignment. By this means, the zero-field resistance of the system is high resulting in a significant decrease for large external magnetic fields. The most prominent ones of these systems are *Fe*/*Cr* [54] and *Co*/*Cu* [55, 56] multilayer systems. The major drawback of these systems is that they are usually sensitive to very high field values on the order of *kOe* because high fields are required in order to overcome the spontaneous antiferromagnetic coupling of the ferromagnetic layers. This gave rise to a new type of conventional layered GMR system which is called spin valve [57]. Spin valves, again, consist of two ferromagnetic layers that are separated by a non-magnetic spacer. In contrast to the systems that are introduced above, one of the magnetic layers of a spin valve is pinned by means of an additional antiferromagnetic layer. The other

magnetic layer can rotate freely in an external magnetic field. Thereby, a weak coupling between the two magnetic layers is realized leading to high sensor sensitivities for small values of the external field. This opened up the perspective of further miniaturization of GMR sensor devices. For all GMR sensors, the electrical resistance is a function of the external magnetic field while the design of the sensor devices strongly depends on its application. But basically, a GMR sensor is a magnetic field sensor and thereby can detect magnetic fields or perturbations of magnetic fields. GMR sensors are applied in electrical current sensing [58], vibration sensors for industrial machines [59], contact-less linear and angular position sensors for e.g. automotive applications [60–62], biomolecule detection [63] and many more.

2.3.1 Multilayer GMR sensors for biomolecule detection

In conjunction with magnetic particles that serve as markers, GMR biosensors can be used for the highly sensitive and rapid detection of different kinds of biomolecules. These sensors can be used in lab-on-a-chip type diagnostics devices that gained interest over the last years [64–66]. The benefits of GMR sensors for these applications include cost-reduction, portability and the possibility of a real-time electronic readout. The working principle of GMR sensors for the biomolecule detection is based on the detection of the magnetic stray field of bound magnetic marker particles on the sensor surface. The magnetic marker particles are functionalized micro or nanoparticles that are also used for the separation of proteins and cells [67], hyperthermia [68] and drug delivery [69]. The application of magnetic markers is connected to several advantages compared to other types of markers such as radioisotopes, enzymes, fluorescent molecules or charged molecules. First, the properties of magnetic particles are very stable over time. Second, the detection can be performed very precisely because usually there is no significant magnetic background in biomolecular samples. Furthermore, the magnetic particles can be manipulated without direct contact by means of external magnetic fields.

A basic GMR sensor for the detection of biomolecules consists of a multilayer system with two magnetic layers and a non-magnetic spacer as previously introduced. The size of the sensor can be microscopic for the detection of magnetic particles in close proximity. For many systems, the labeling of the analyte is done by ligand-receptor interactions in a sandwich configuration as shown in figure 2.10. Therefore, the magnetic multilayer GMR sensor is covered by receptor molecules that are chosen to match the target molecules that are to be detected. When exposed to a sample solution such as blood that contains the target biomolecules, the target biomolecules bind to the receptor molecules on the sensor surface by molecular recognition. In a second step, excess sample solution is removed from the sensor surface. Afterwards, magnetic particles such as

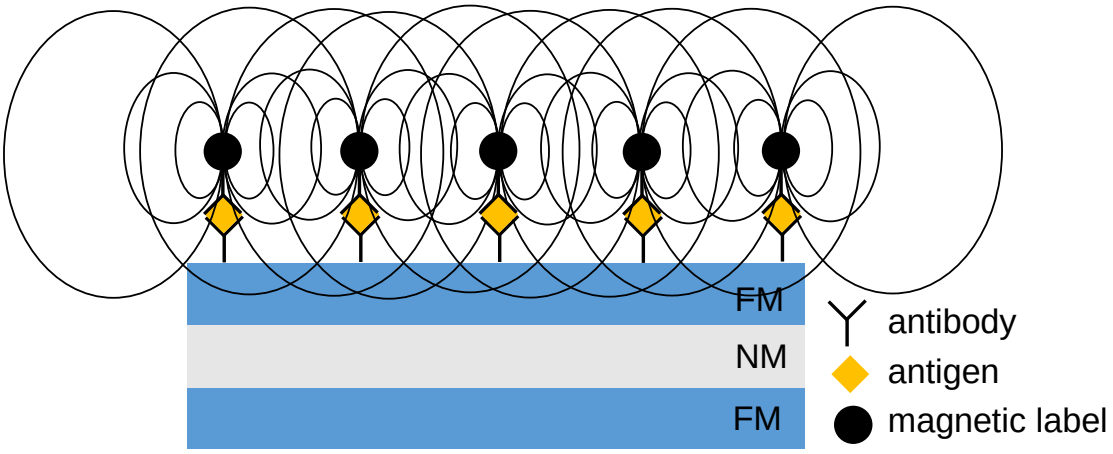

FIGURE 2.10: Basis multilayered GMR sensor system consisting of two ferromagnetic (FM) layers and a non-magnetic (NM) spacer layer for the detection of biomolecules. The GMR sensor is covered by receptor molecules or antibodies that are chosen specifically for the measuring task. This structure is exposed to the target biomolecules or antigens that are immersed in the sample solution. Thus, the target biomolecules bind to the receptor molecules on the sensor surface. As a next step, magnetic particles that are coated with receptor molecules are introduced into the system. The stray field of the particles can finally be measured by the GMR sensor. [64]

superparamagnetic beads that are coated with the same receptor molecules as the sensor surface are introduced into the system. Hence, the magnetic particles bind to the target biomolecules that are already bound to the sensor surface. Unbound magnetic particles are removed by means of a magnetic gradient field. Finally, the number of bound magnetic particles and at the same time the number of target molecules is measured by the resistance of the GMR sensor due to the magnetic stray fields of the magnetic marker particles. [64]

The main disadvantage of multilayered GMR sensors is that further miniaturization leads to a conflict between the length scale of the sensor and the superparamagnetic limit (compare chapter 2.1). Thus, the magnetization of the sensor can be destabilized by thermal fluctuations. As a consequence, high anisotropies are required to obtain a stable magnetization but at the same time the sensor sensitivity is reduced. One possible solution can be found in granular GMR systems. [6]

2.3.2 Granular GMR biosensors on the basis of magnetic nanoparticles in conductive gel matrices

Recent research has revealed the advantages of granular systems that consist of magnetic nanoparticles that are embedded in conductive gel matrices as introduced in chapter 2.2.3 [5, 6, 70, 71]. The magnetic particles in these systems interact solely by means of the magnetic dipole-dipole interaction. Thus, there are no significant interparticular

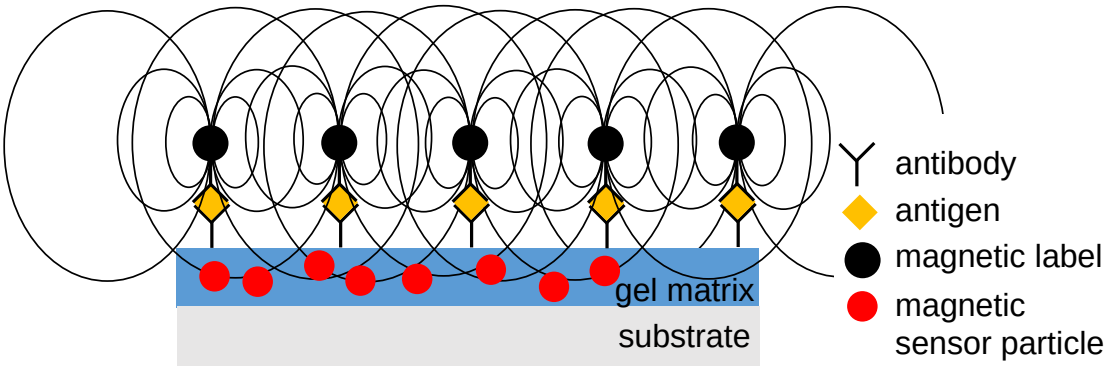

FIGURE 2.11: Nanoparticle-based GMR sensor system consisting of magnetic nanoparticles in a conductive gel matrix. Similar to figure 2.10, the GMR sensor is covered by receptor molecules or antibodies that are chosen specifically for the measuring task. This structure is exposed to the target biomolecules or antigens that are immersed in the sample solution. Thus, the target biomolecules bind to the receptor molecules on the sensor surface. As a next step, magnetic particles that are coated with receptor molecules are introduced into the system. The stray field of the particles can finally be measured by the particle-based GMR sensor. [6]

exchange interactions present. As a result, the magnetic particles obtain configurations with locally and globally vanishing magnetizations as it has been shown in [71] in contrast to the magnetization of thin continuous layers. This additional magnetic substructure leads to promising properties of particle-based GMR systems. Moreover, it can be shown that the magnetic moment orientations are strongly bound to the sensor plane [71, 72]. This situation corresponds to a multilayer system with insignificant perpendicular anisotropy [6] enabling further miniaturization without decreasing the sensor sensitivity.

While the working principle of the sensor is changed from multilayer to granular GMR, the principle of marking the target biomolecules with magnetic labels stays the same (compare chapter 2.3.1) as shown in figure 2.11. One of the main advantages of particle-based GMR sensors can be identified regarding the fabrication techniques involved. As reported in [73], conventional multilayer systems are prepared by vacuum techniques such as evaporation, sputtering or molecular beam epitaxy. It has been shown in [5, 6] that these elaborate techniques can be avoided by using gel-based nanoparticular sensor materials. Instead of using vacuum-based techniques, the particle-gel mixtures can be printed and thereby provide a very efficient way to produce low-cost sensor devices. After printing the particle-gel mixture on a substrate, e.g. a simple paper strip, the magnetic particles can be structured by external magnetic fields in order to enhance the sensor sensitivity or the particles arrange themselves by means of self-assembly in the liquid state of the gel. After drying out the gel matrix, the sensor strip is coated with receptor molecules that are chosen specifically for the measuring task. This is done by

dipping the strip in a receptor molecule solution. Afterwards, the sensor is immersed in a sample solution such as blood that contains the target biomolecules. Hence, the target molecules bind to the receptor molecules that are already attached to the sensor surface. In order to determine the number of target molecules on the sensor surface the GMR effect is used. In order to influence the magnetic structure of the nanoparticles that are immersed in the gel matrix, other magnetic particles, e.g. superparamagnetic beads, are attached to the target molecules. This is done by means of more receptor molecules that are attached to the magnetic marker beads. Thus, the nanoparticular GMR biosensor is covered by magnetically labeled target molecules to a certain extent. The magnetic answer of the sensor can be measured by means of the change of the electrical resistance that can be determined precisely due to the high GMR effect amplitude. [5, 6, 70, 74]

3

Basic simulation methods

In order to simulate interacting magnetic nanoparticles that are immersed in viscous matrices, two different tasks have to be addressed. First, the forces on the particles due to particle-particle and particle-matrix interactions have to be calculated and the resulting motion has to be applied. Second, the magnetic low energy configuration, i.e. the configuration of the magnetic moments that results in a minimum total energy must be calculated. Within the work that is presented here, two different simulation methods, each of them highly specialized, are used to account for these two tasks. The calculation of the magnetic moment low energy contributions is done by means of classical spin dynamics simulations whereas molecular dynamics is used to calculate the resulting forces and determine the particle trajectories according to these forces. Here, the basic simulation methods are presented.

3.1 Classical spin dynamics

Classical spin dynamics (SD) is a numerical technique for the computation of the static and dynamic magnetic properties of microscopic and mesoscopic ensembles of magnetic moments with respect to the temperature. In contrast to quantum mechanical techniques that solve the quantum mechanical equations of motion for the expectation value, within classical SD the classical equations of motion are solved in order to calculate the time evolution of the magnetic moments. In this work, a spin dynamics algorithm that solves the Landau-Lifshitz equation is used. In order to consider the temperature, a Langevin approach is used to model the contact to an external heat bath. The basic working principle of the algorithm is presented in the following sections. A more detailed description can be found in [75] and [76].

3.1.1 Magnetic macro moment approximation

In the framework of this thesis spin dynamics is applied to ensembles of magnetic nanoparticles. Each magnetic nanoparticle consists of a large number of atoms and therefore a large number of magnetic moments. Thus, the simulation of a system that contains many magnetic particles results in a considerable computational effort. As it has been shown in chapter 2.1, magnetic particles can be considered as single-domain particles below a critical diameter d_{SD} [9–11]. Here, all particles are assumed to be small enough to be single-domain particles and can therefore be considered as particles that carry one single effective magnetic moment. This so called macro moment approximation is common practice for the simulation of ensembles of single-domain particles. Within this work, each particle is assumed to carry one single magnetic moment that is calculated according to the following equation.

$$\mu_{eff} = \frac{M_{sat} \cdot \pi \cdot d^3}{6 \cdot \mu_B} \tag{3.1}$$

In this equation, M_{sat} represents the saturation magnetization of the particle material, d is the particle diameter, and μ_B denotes the Bohr magneton.

3.1.2 Classical equations of motion for the spin Hamiltonian

A magnetic moment $\mathbf{S}$ that is exposed to an external magnetic field precesses around the magnetic field direction. The precessional motion is described by the classical equations of motion for the spin Hamiltonian. Whereas the quantum mechanical equations of motion can be derived from the spin commutator relations as shown in equation 3.2, the classical analog is given by the Lie-Poisson bracket, see equation 3.3 [77].

$$\left[\hat{S}_i^{\alpha}, \hat{S}_j^{\beta}\right] = i\hbar\delta_{ij}\epsilon_{\alpha\beta\gamma}\hat{S}_i^{\gamma} \tag{3.2}$$

$$\left\{F\left(\{\mathbf{S}\}\right), G\left(\{\mathbf{S}\}\right)\right\} = \sum_{i=1}^{N} \epsilon_{\alpha\beta\gamma} \frac{\partial F}{\partial S_i^{\alpha}} \frac{\partial G}{\partial S_i^{\beta}} S_i^{\gamma} \tag{3.3}$$

Therein, $F\left(\{\mathbf{S}\}\right)$ and $G\left(\{\mathbf{S}\}\right)$ represent arbitrary functions of the vector set $\{\mathbf{S}\}$ and $\epsilon_{\alpha\beta\gamma}$ is the Levi-Civita tensor. Moreover, the spin operators of the quantum mechanical description are interpreted as classical variables S_i^{α}. The classical counterpart of the quantum mechanical commutator relations can be constructed by replacing $F\left(\{\mathbf{S}\}\right) = S_i^{\alpha}$ and $G\left(\{\mathbf{S}\}\right) = S_j^{\beta}$ in equation 3.3.

$$\left\{S_i^\alpha, S_j^\beta\right\} = \epsilon_{\alpha\beta\gamma}\delta_{ij}S_i^\gamma \tag{3.4}$$

Thus, the time evolution of the α-component of a magnetic moment $\mathbf{S}$ at a position i can be derived by equation 3.5.

$$\begin{aligned}\hbar\frac{\partial S_i^\alpha}{\partial t} &= \{S_i^\alpha, \mathcal{H}(\{\mathbf{S}\})\} \\ &= \sum_{j=1}^{N}\epsilon_{\alpha\beta\gamma}\delta_{ij}\frac{\partial\mathcal{H}}{\partial S_j^\beta}S_j^\gamma \\ &= \left(\frac{\partial\mathcal{H}}{\partial\mathbf{S}_i}\times\mathbf{S}_i\right)^\alpha\end{aligned} \tag{3.5}$$

This can be generalized in order to obtain the classical equations of motion for the spin Hamiltonian.

$$\begin{aligned}\hbar\frac{\partial\mathbf{S}_i}{\partial t} &= \frac{\partial\mathcal{H}}{\partial\mathbf{S}_i}\times\mathbf{S}_i \\ &= \mathbf{H}_{eff}\times\mathbf{S}_i\end{aligned} \tag{3.6}$$

The local field splitting or effective field $\mathbf{H}_{eff}$ sums up all contributions to the local effective magnetic field due to interactions with the magnetic moment under consideration. The precessional motion of the magnetic moment is a result of the cross product in equation 3.6. [75]

3.1.3 Landau-Lifshitz equation

The time evolution of a single magnetic moment that is calculated according to 3.6 is always an infinite precession around the effective field direction with a constant energy as it is shown in figure 3.1(a). In real magnetic materials, the magnetic moments would gradually lose energy because of lattice interactions, interactions with itinerant electrons and impurities or by means of spin waves [78]. As it was first proposed by Landau and Lifshitz in 1935, a damping term that is proportional to a positive damping constant λ can be included in equation 3.6 [79].

$$\frac{\partial\mathbf{S}_i}{\partial t} = \frac{1}{\hbar}\mathbf{H}_{eff}\times\mathbf{S}_i - \lambda\frac{1}{\hbar}\left(\mathbf{H}_{eff}\times\mathbf{S}_i\right)\times\mathbf{S}_i \tag{3.7}$$

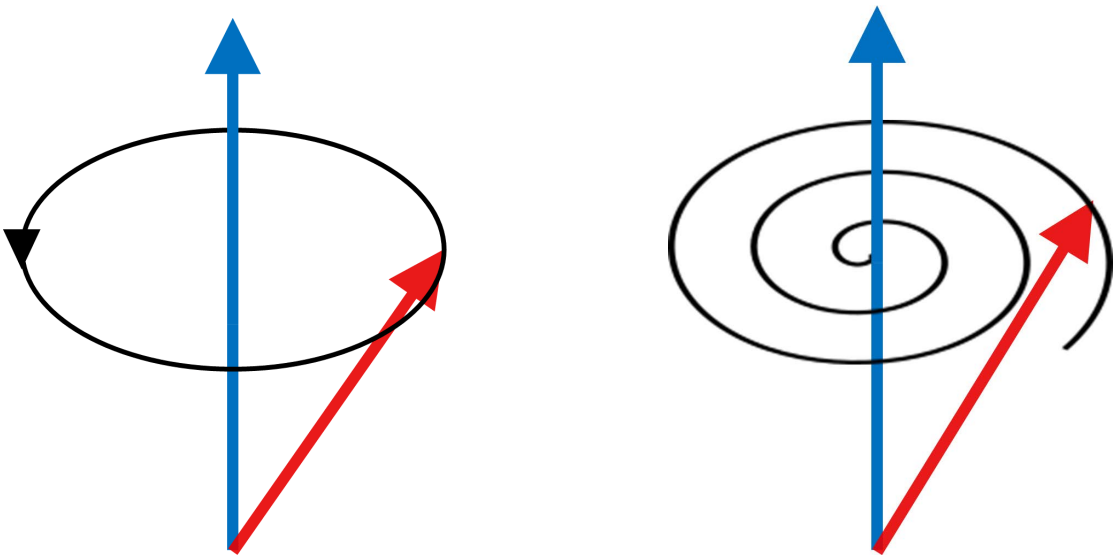

(a) (b)

FIGURE 3.1: Precessional motion of a spin (red) around the direction of the effective field (blue) that consists of all interaction contributions. As a result of the classical equations of motion without the inclusion of a damping term, the spin precesses around the field direction for all the times (a). By adding a damping term to the equations of motion, the spin loses energy and therefore spirals towards the local energy minimum (b).

The resulting damping force is perpendicular to the precession and points towards the local energy minimum which is equal to the local effective field direction (see figure 3.1(b)). A reformulation of the damping term of the Landau-Lifshitz equation was proposed by Gilbert in 1955 [80]. In Gilbert's approach which is also known as the Landau-Lifshitz-Gilbert (LLG) equation, the damping is reflected by a damping term that is proportional to the frequency of the precessional motion as shown in equation 3.8.

$$\frac{\partial \mathbf{S}_i}{\partial t} = \frac{1}{\hbar}\mathbf{H}_{eff} \times \mathbf{S}_i + \alpha \mathbf{S}_i \times \frac{\partial \mathbf{S}_i}{\partial t} \tag{3.8}$$

It can be shown that the LLG equation is mathematically equivalent to the original formulation by Landau and Lifshitz in equation 3.7. [75, 81]

3.1.4 Heat bath coupling

Systems of magnetic moments that are considered in the Landau-Lifshitz picture as it is defined in equation 3.7 interact with each other and with external fields by means of magnetic interactions that are introduced by the effective magnetic field $\mathbf{H}_{eff}$ whereas the thermodynamic properties are neglected.

Statistical mechanics provides a link between the macroscopic thermodynamic properties of a system and the microscopic origin of these properties. For large numbers of particles it is impossible to consider the microscopic details. However, the vast majority of microscopic information is not required in order to describe the macroscopic observables because there is a multitude of microscopic configurations that leads to the same macroscopic properties. As it is stated in [82], if the temperature of a system is connected to the average kinetic energy of the particles that the system contains, the same temperature can be measured for many different configurations of the velocities of the individual particles. However, each configuration corresponds to a different point in phase space. Hence, every configuration represents a unique microscopic state but the macroscopic observables are not sensitive to the microscopic details. This is reflected by the concept of *ensembles* in statistical mechanics. [75, 82]

Ensembles

An ensemble is defined as an accumulation of systems with the same microscopic interactions and therefore shared macroscopic properties. Each of the systems that the ensemble contains evolves from different initial conditions. The macroscopic properties are then calculated by averaging over the microscopic states. There are different ways to define an ensemble. The most simple ensemble definition considers an ensemble with N particles with a total energy E in a volume V that is isolated from its environment. Thus, N, V and E are conserved quantities. This type of ensemble is known as the microcanonical ensemble. The microcanonical ensemble provides a very simple way to treat statistical systems of particles but it does not reflect the experimental situation in many cases. Experimentally, systems of particles can rarely be considered as isolated from their environment. Usually, the system exchanges energy with its enviroment by means of thermal energy. This is considered in the framework of the canonical ensemble. Therein, the number of particles N and the volume V are constant. In contrast to the microcanonical ensemble the total energy E is no conserved quantity. In addition to that, a constant temperature T is defined to represent the thermal contact to an infinite heat reservoir [75, 82].

Langevin approach

In the context of a canonical ensemble, the exchange of energy has to be regulated in order to keep the system's temperature constant. This can be done by means of a Langevin-like approach. Within this approach, the contact of the system and the heat bath is realized by stochastic forces. This approach is based on the works of Einstein

[83] and Langevin [84] on the Brownian motion of particles [85]. According to Langevin, Brownian particles experience two different kinds of forces. On the one hand the particles are exposed to dynamic friction which is represented by a viscous drag force $\zeta\dot{r}(t)$ with r being the replacement and ζ being the friction coefficient. On the other hand the particles experience a rapidly fluctuating force $F(t)$ due to the impacts of the molecules of the surrounding medium. With these forces, the equation of motion of the particles due to Newton's second law reads as follows.

$$m\ddot{r}(t) = -\zeta\dot{r}(t) + F(t) \tag{3.9}$$

It is assumed [84] that the fluctuating force F(t) is independent of the displacement $r(t)$. Moreover, it is assumed that $F(t)$ varies very rapidly when compared to the variation of the displacement. In addition to that, the statistical average value of $F(t)$ for an ensemble of particles, $\bar{F}(t)$ is assumed to be zero due to its irregularity. [86]
Similar to the prototypical Langevin equation 3.9, systems of magnetic moments can be treated in a stochastic way in order to mimic the interaction with an external heat bath. The heat bath interaction is therefore introduced into the damped Landau-Lifshitz equation as it is shown in equation 3.7 in terms of a fluctuating term $\mathbf{f}_i \times \mathbf{S}_i$.

$$\frac{\partial \mathbf{S}_i}{\partial t} = \frac{1}{\hbar}\mathbf{H}_{eff} \times \mathbf{S}_i - \lambda\frac{1}{\hbar}\left(\mathbf{H}_{eff} \times \mathbf{S}_i\right) \times \mathbf{S}_i + \mathbf{f}_i \times \mathbf{S}_i \tag{3.10}$$

In equation 3.10, $\mathbf{f}_i$ denotes the fluctuations due to thermal agitation represented by a stochastic distribution. In accordance with the Langevin equation, the statistical average of the fluctuating force must vanish in order to avoid any thermally induced drift of the system. It can be shown that the length of the spin is conserved by the stochastic Landau-Lifshitz equation. [75]

3.1.5 Integration of the spin equations of motion

In order to treat the stochastic Landau-Lifshitz equation for arbitrary spin systems numerically, a fourth order Runge-Kutta method as proposed by Milstein and Tretyakov [87] is used for the integration within this work. An extensive description of the numerical realization is given in [75] and will not be discussed here.

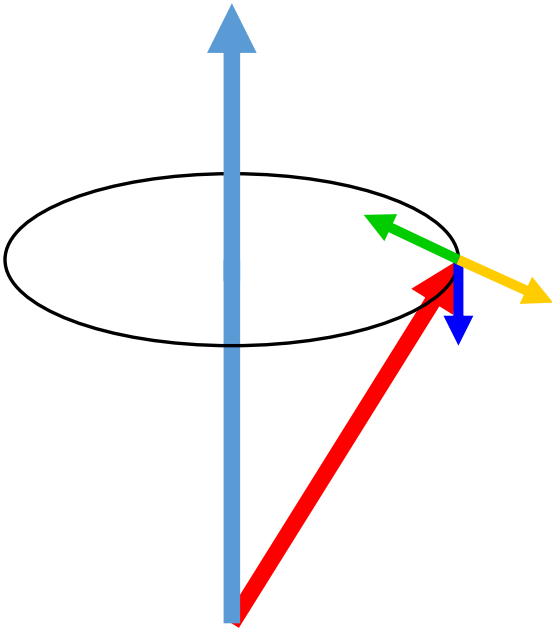

FIGURE 3.2: Visualization of the forces that act on a single spin (red) in the framework of the stochastic Landau-Lifshitz equation. The spin precesses around the effective field direction (light blue) due to the precessional force (dark blue). In addition to that, a damping force (green) acts on the spin in a way that the precessional motion relaxes towards the effective field direction. In order to account for thermal agitation of the spin, a fluctuating force (yellow) is introduced.

3.1.6 Classical spin dynamics summary

In summary, systems of classical magnetic moments or spins can be treated by means of classical spin dynamics. The method that is used within this work utilizes the stochastic Landau-Lifshitz equation in order to describe the time evolution of the magnetic moments under consideration of damping and temperature effects. The coupling to a heat bath is realized by a Langevin-like approach. The resulting equations of motion are integrated numerically by a fourth order Runge-Kutta method. This method can be applied to arbitrary systems of classical magnetic moments. Whereas the positions of the magnetic moments are fixed in space, the magnetic moment orientations due to interactions between the magnetic moments and interactions with the magnetic moments and external magnetic fields are calculated. In this work, a program package that is presented in [76] is used for all spin dynamics simulations. The program package provides a comprehensive tool box with algorithms for Monte Carlo and spin dynamics simulations together with a multitude of application modes. For a detailed description of the program, the reader is referred to [75, 76]. Within the spin dynamics picture, the magnetic moments are fixed in space which holds true for solid structures or, in comparison to the time scale of the magnetic relaxation, very slowly changing magnetic moments, e.g. magnetic particles in viscous matrices. This is presented in detail in chapter 6.

3.2 Classical molecular dynamics

Classical molecular dynamics provides a method to compute the trajectories of atoms, molecules or general particles. In contrast to quantum mechanical approaches, the forces that induce the motion of the particles are derived from classical potential functions. Molecular dynamics simulations involve three fundamental problems:

1. the physical model that describes the interactions between the particles and between the particles and external fields,
2. the calculation of potential energies and the resulting forces from the physical model, and
3. the algorithm that is used to integrate the underlying equations of motion with respect to the calculated forces.

Within this chapter, common solutions to these three crucial problems are introduced in general and in the context of the simulation of the magneto-dynamics of ensembles of magnetic nanoparticles in viscous matrices.

3.2.1 Potential energy functions

For molecular dynamics simulations atoms, molecules, or general particles are modeled by point masses that interact with other particles and with external fields. In contrast to *ab initio* methods that are based on quantum mechanical fundamentals, classical molecular dynamics addresses systems of classical particles that are connected by means of different kinds of virtual springs. In order to calculate the trajectories of particles in a classical framework, the particle-particle and particle-field interactions have to be defined in a suitable manner. In the context of molecular dynamics, the definition of interactions as potential energy functions or force field is widely used. The forces on the particles can directly be derived from these potential energy functions by equation 3.11.

$$\mathbf{F}_i\left(\mathbf{r}_1, ..., \mathbf{r}_N\right) = -\nabla_i U\left(\mathbf{r}_1, ..., \mathbf{r}_N\right) \tag{3.11}$$

Here, $\mathbf{F}_i$ represents the force that the ith particle experiences due to the N other particles at the positions $\mathbf{r}_1, ..., \mathbf{r}_N$ in the system. The force is calculated by the scalar potential function $U\left(\mathbf{r}_1, ..., \mathbf{r}_N\right)$ with $\nabla_i U = \frac{\partial}{\partial \mathbf{r}_i}$. In the framework of isotropic pair potential functions the resulting forces depend exclusively on the distances between the particles whereas the absolute orientation is irrelevant. In contrast to that, anisotropic pair

potentials depend on the particles' spatial orientations as well. The formulation of suitable potential energy functions is usually complicated. Typically, they are not strictly derived from first principles but determined by combinations of quantum mechanical energy calculations, spectroscopy data, transport measurements, and other techniques. In iterative processes the potential formulations are refined by means of experimental data.

A potential energy function has to provide two key features. First, atoms, molecules, or particles are bound together in the liquid and solid states of matter. Therefore, the potential function must enable the attraction of particle pairs over long distances. At the same time, the potential has to provide a repulsive contribution for short interparticle distances in order to mimic the material's resistance to compression. There is a multitude of standard potentials that satisfy these conditions. In other cases in which the potential function does not provide the required short-range repulsion it has to be used in combination with a purely repulsive potential in order to establish physically correct behavior. One famous example of an attractive-repulsive potential energy function is the Lennard-Jones potential.

Lennard-Jones potential

The Lennard-Jones potential, also known as 12-6 potential, is a well-known potential energy function for molecular dynamics simulations. It was originally proposed by John Lennard-Jones to describe the intermolecular forces of liquid argon [88]. The most common form of the Lennard-Jones potential is given in the following equation.

$$U_{LJ} = \begin{cases} 4\epsilon \left[\left(\frac{\sigma}{r_{ij}} \right)^{12} - \left(\frac{\sigma}{r_{ij}} \right)^{6} \right], & \text{if } r_{ij} < r_{cut} \\ 0, & \text{if } r_{ij} \geq r_{cut} \end{cases} \tag{3.12}$$

Therein, ϵ represents the depth of the attractive potential well in units of energy, σ is the distance at which the potential becomes zero, and r_{ij} is the distance between the particles i and j. To reduce the computational complexity a cut-off radius r_{cut} can be defined at which the interaction between the particles becomes insignificant. Figure 3.3 shows the Lennard-Jones potential for $\sigma = \epsilon = 1$. [88–90]

3.2.2 Particle-particle and particle-matrix interactions in systems of interacting magnetic particles in viscous surrounding media

In order to model interacting magnetic particles in a viscous surrounding medium, three different contributions have to be included in order to mimic the magnetic interactions as

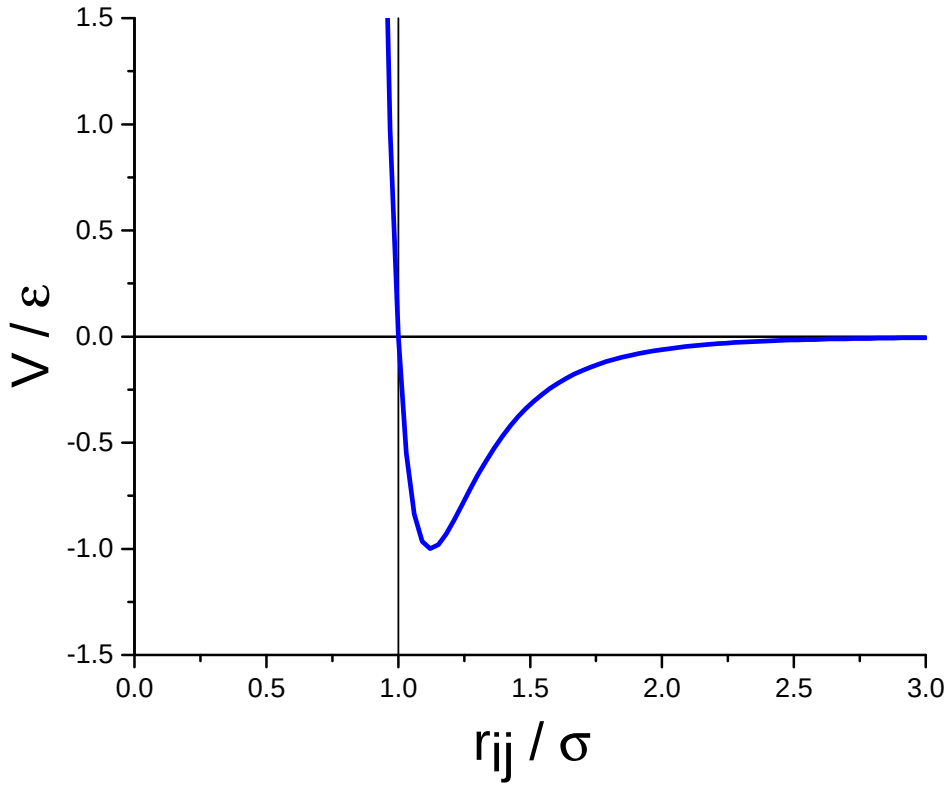

FIGURE 3.3: The Lennard-Jones potential in the 12-6 form for the case of $\epsilon = 1$ in units of energy and $\sigma = 1$ in units of distance. The potential consists of a short-range repulsive and a long-range attractive contribution in order to mimic interparticular forces for many applications.

well as the hard sphere interactions and the effect of the matrix viscosity. The particle-particle interactions are included in terms of potential energy functions whereas the particle-matrix interaction is taken into account as a force contribution.

Magnetic dipole-dipole interaction

The leading interaction between magnetic particles on the nanoscale that are immersed in viscous matrices is the magnetic dipole-dipole interaction that is introduced in the chapters 2.1.1 and 2.1.3 [28, 29]. Every particle in the system produces a magnetic dipole field that affects every other particle. As the distances between the particles can be considered large other magnetic interactions, i.e. exchange-type interactions, can be neglected [12]. The pairwise potential energy contributions due to the magnetic dipole-dipole interaction of two magnetic particles with magnetic moments $\mathbf{m}_1$ and $\mathbf{m}_2$ can be calculated according to the following equation.

$$U_{\mathrm{DD}} = -\frac{\mu_0}{4\pi r_{12}^3}\left[3\left(\mathbf{m}_1 \cdot \frac{\mathbf{r}_{12}}{r_{12}}\right)\left(\mathbf{m}_2 \cdot \frac{\mathbf{r}_{12}}{r_{12}}\right) - \mathbf{m}_1 \cdot \mathbf{m}_2\right] \tag{3.13}$$

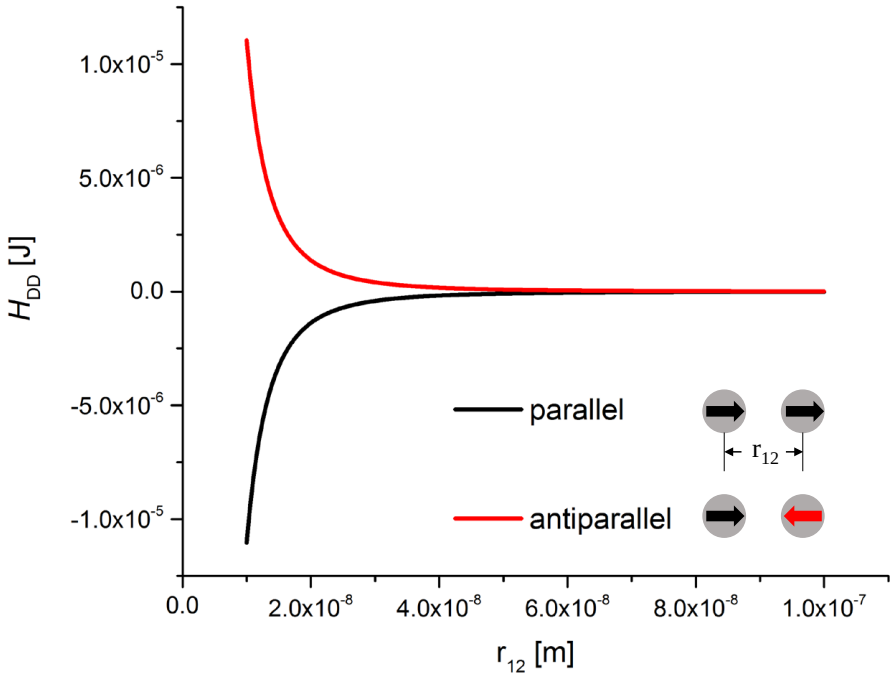

FIGURE 3.4: Exemplary magnetic dipole-dipole interaction energies of two interacting cobalt nanoparticles with diameters of 10 nm. The magnetic dipole-dipole interaction energy is plotted against the center-to-center distance r_{12} of the particles which is varied from 10 nm to 100 nm. For a parallel alignment of the magnetic moments of the particles negative energy values are obtained (black line) resulting in attractive forces between the particles. On the other side, an antiparallel alignment of the magnetic moments results in positive energy values (red line) and particle repulsion. Even for this small sample that consists of only two particles the dipole-dipole energy acts over a long distance of about 8 particle diameters.

In equation 3.13, $\mathbf{m}_1$ and $\mathbf{m}_2$ again represent the magnetic moments of the two particles of one particle pair while $\mathbf{r}_{12}$ represents the vector that connects the centers of these two particles. The absolute value of the center-to-center distance is given by r_{12}. The magnetic dipole-dipole interaction results in a force (see equation 2.9) that acts along the line that connects the centers of the particles. With the magnetic dipole-dipole interaction, attraction and repulsion of the particles can occur depending on the relative orientations of $\mathbf{m}_1$ and $\mathbf{m}_2$. Due to its slow decay, the magnetic dipole-dipole interaction is computationally elaborate. The absolute value of the energy as calculated by equation 3.13 is usually small but at the same time it acts on a very long distance. An exemplary case of two dipolarly interacting cobalt particles each with a diameter of 10 nm is shown in figure 3.4 for the cases of parallel and antiparallel alignment of the magnetic moments of the particles. From this it becomes apparent that no clear cut-off radius for the magnetic dipole-dipole interaction can be defined. Hence, the calculation of all pairwise dipole-dipole interactions is necessary in every step in time.

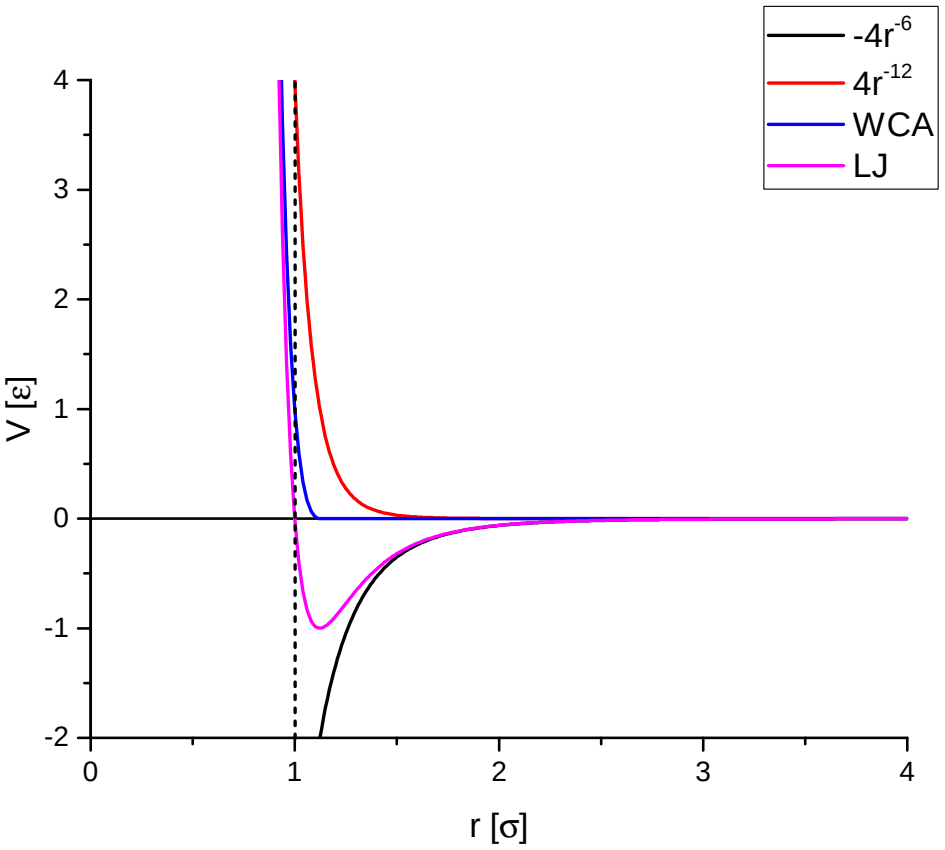

FIGURE 3.5: Comparison of the attractive and repulsive Lennard-Jones potential (magenta, see chapter 3.2.1) and the purely short-range repulsive Weeks-Chandler-Andersen potential (blue) for $\sigma = \epsilon = 1$. The dominating contributions of both potential energy functions $4 \cdot r^{-12}$ and $-4 \cdot r^{-6}$ are shown in red and black respectively.

Weeks-Chandler-Andersen (WCA) potential

As already stated in chapter 3.2.1, each potential energy formulation has to provide long-range attraction and short-range repulsion in order to result in physical behavior. As the sign of the magnetic dipole-dipole interaction depends on the relative orientation of the magnetic moments that are involved, a purely repulsive short-range potential contribution must be included as well. Thus, the magnetic particles can be modeled as hard spheres without inclusion of an elaborate collision detection. The well-known Weeks-Chandler-Andersen (WCA) potential [91] provides a force-shifted variant of the Lennard-Jones potential that is introduced above.

$$U_{\mathrm{WCA}} = \begin{cases} 4\epsilon \left[\left(\frac{\sigma}{r_{ij}} \right)^{12} - \left(\frac{\sigma}{r_{ij}} \right)^{6} \right] + \epsilon, & \text{if } r_{ij} < 2^{\frac{1}{6}}\sigma \\ 0, & \text{if } r_{ij} \geq 2^{\frac{1}{6}}\sigma \end{cases} \tag{3.14}$$

By the WCA potential, the required short-range repulsion of the interacting magnetic particles can precisely be realized. Above a distance of two interacting particles $r_{ij} \geq$

$2^{\frac{1}{6}}\sigma$, the WCA potential is cut off. Below this distance, a Lennard-Jones type repulsion is used. The parameters σ and ϵ are equivalent to the same parameters of the Lennard-Jones potential as introduced in 3.2.1. A comparison of the Lennard-Jones and the WCA potential is given in figure 3.5.

Stokes drag

The motion of the magnetic particles is affected by the viscosity of the surrounding medium, e.g. water or different kinds of gel matrices in their liquid state. The force that acts on a small spherical particle with a diameter d_p at a velocity v_p that is surrounded by a viscous material with a dynamic viscosity η_m can be calculated by means of Stokes' law.

$$F_{\text{visc}} = 3\pi d_p \eta_m v_p \tag{3.15}$$

In contrast to the previously introduced particle-particle interactions, the drag force is a particle-matrix type interaction that is calculated once for every particle in every step in time of the molecular dynamics simulation. Moreover, this contribution is typically given in terms of a force instead of a potential energy but can be transformed by means of equation 3.11.

3.2.3 Force calculation

The forces that act on the particles have to be calculated in every step in time of the molecular dynamics simulation. As introduced in chapter 3.2.2, particle-particle and particle-matrix contributions can be distinguished. Whereas the particle-particle interactions have to be calculated for every pair of particles in the system under consideration, one contribution per single particle has to be considered for particle-matrix interactions. The same holds true for general particle-field interactions which are not subject of this work. Particle-field or particle-matrix interactions are generally easy to compute because the computational problem is of the order of the number of particles in the system N. In contrast to this, the computation of pairwise interactions is much more demanding because of the higher order of the problem. There are different approaches of how to consider pairwise interactions in the calculation of forces that are presented in the following. Which of these approaches can be applied depends on the physical type of the potential energy function. [89]

Neighbor list

For short-range potentials such as the Lennard-Jones potential (see chapter 3.2.1), a cut-off radius can be defined at which the potential energy becomes zero. As a consequence, particle pairs at distances larger than the cut-off radius do not interact with each other. For the neighbor list method, a list is maintained that contains information about the neighborhood of every particle in the system. In this list all pairs of particles with distances within the cut-off radius are labeled as neighbors. For the calculation of forces this means that only particle pairs that are neighbors according to the neighbor list have to be considered. Thus, the order of the problem is reduced compared to the full problem. In order to reduce the complexity of the problem further, it can be assumed that the neighbor list is valid for more than one step in time of the simulation [90, 92]. On modern computers, even large systems can be treated in terms of a neighbor list. For extremely large systems, methods exist that reduce the required memory capacity as it is presented in [90]. On the downside, the neighbor list method is not efficiently applicable to potential energy functions with long-range characteristics, e.g. the magnetic dipole-dipole interaction (see chapter 3.2.2).

Cell computation

Another method to reduce the computational effort of the force calculation has been proposed in [93]. Within this approach, the system is divided into two or three-dimensional cells. The edges of these cells have to be longer than the cut-off radius of the potential energy function under consideration. Thus, interactions of the particles are only relevant for particles in the same cell or in adjacent cells. The cell information can efficiently be organized in a linked list as proposed in [94]. Hence, the linked list is used to identify the particles that belong to a cell. It provides a rational way to organize the memory because the particle structure inside the rigid cells changes in every time step of the simulation. Again, the application of this approach is only efficiently possible in the case of a well-defined cut-off radius. [90]

All-pairs method

The all-pairs-method is a method to consider the full problem of the computation of pairwise interactions. This method is applicable to all kinds of potential energy functions with short and long-range characteristics. Moreover, it is easy to implement because there is no selection between active and inactive pairwise interactions due to a cut-off radius as it is the case for the neighbor list and cell computation approaches. On the

downside, the all-pairs method is very inefficient for short-range potentials because all contributions are considered, even zero contributions. On the other hand, for long-range potential functions the computational effort is the same but the all-pairs method provides correct potential energies whereas cutting off the potential leads to unphysical behavior. More sophisticated methods for the calculation of forces are presented in the literature. However, even these methods utilize an effective potential cut off [82, 89]. Within this work, the all-pairs method is applied for molecular dynamics simulations in order to preserve the long-range characteristics of the magnetic dipole-dipole interaction. [90]

3.2.4 Integration of the translational equations of motion

The particles in systems that are investigated by means of classical molecular dynamics simulations obey the laws of Newtonian mechanics. Therefore, the forces that are calculated in the previous step result in an acceleration of the particles in consideration of the particle mass due to Newton's second law [95]. There is a multitude of algorithms to integrate the Newtonian equations of motion, e.g. the Euler method which is presented in the following and different types of Runge-Kutta algorithms [96] or Verlet type integration schemes [92]. In order to identify a suitable algorithm for the integration of the equations of motion several general features have to be considered. First of all, the force calculation is computationally much more demanding than the subsequent integration. For this reason, the actual speed of the integration algorithm plays a secondary role. Moreover, the accuracy for large time steps has to be considered. The longer the time step size can be chosen, the fewer force calculations are necessary and the more problems can be treated by the method. The usually strong short-range repulsive potential functions in molecular dynamics simulations impose an effective upper limit on the time step size. As a consequence, adaptive methods cannot be applied. In addition to that, one has to consider the energy conservation properties of the candidate algorithms.
Simple integration methods usually have a fair accuracy for short time ranges and a small drift in energy on longer time scales. Besides the energy conservation being a feature of Newton's equations of motion, the equations are also invariant under time-reversal and area-preserving which should be considered for the choice of the integrator algorithm as well. Time-reversibility is featured by some well-known algorithms such as the Leapfrog algorithm [97]. On the other hand, there are algorithms that do not provide time-reversibility, e.g. predictor-corrector integration schemes [96]. Moreover, the preservation of areas which is called symplecticity should be considered. If the equations of motion act on a system of particles that span an area or a volume Ω, Ω evolves in time. Symplectic algorithms, as well as the Newtonian equations of motion, conserve Ω

even for long simulation times according to Liouville's theorem whereas non-symplectic algorithms map Ω on Ω' which is usually much larger than Ω. It can be shown that non-symplecticity is connected to a drift in energy. To sum up, time-reversibility and symplecticity are not necessary for the integration of the equations of motion but they support the energy conservation which has to be provided in order to produce accurate trajectories. [89, 90]

For molecular dynamics simulations usually one of two Verlet type algorithms is utilized, namely the Leapfrog algorithm or the Velocity Verlet algorithm. Both of them are time-reversible and symplectic which leads to a good energy conservation on short time scales and a considerably small long-time drift. At the same time, both algorithms are easy to implement and stand out due to their performance and low memory consumption. [89, 90]. The Leapfrog algorithm and the Velocity Verlet algorithm are presented in the following after introducing the Euler method as the most simple integration method and the basic Verlet scheme at the beginning.

Euler method

The Euler method, named after swiss physicist and mathematician Leonhard Euler, is the most simple type of a Runge-Kutta scheme [96]. It provides a method to solve ordinary differential equations to given initial values. It can be used to integrate the equations of motion in the context of molecular dynamics simulations. This method is based on the truncated Taylor expansion of the position r around the time t.

$$r\left(t+\Delta t\right)=r\left(t\right)+\dot{r}\left(t\right)\Delta t+\frac{\ddot{r}\left(t\right)}{2}\Delta t^{2}+\mathcal{O}\left(\Delta t^{3}\right) \tag{3.16}$$

The actual Euler integration scheme is derived by inserting the expressions for $\dot{r}\left(t\right)$ and $\ddot{r}\left(t\right)$ from the Newtonian equations.

$$r\left(t+\Delta t\right)=r\left(t\right)+v\left(t\right)\Delta t+\frac{F\left(t\right)}{2m}\Delta t^{2}+\mathcal{O}\left(\Delta t^{3}\right) \tag{3.17}$$

It can be shown that the step's error is only one power of Δt smaller than the correction $= \left(\Delta t^{3}\right)$, i.e. $\left(\Delta t^{2}\right)$. Furthermore, this algorithm is neither time-reversible nor symplectic and as a consequence of that exhibits a strong energy drift. It has only conceptional use and is not recommended for any practical application. There are other methods that are based on the Euler method with much better properties such as the Backward Euler and

Midpoint methods which in turn lead to the Runge-Kutta and Linear Multistep methods. Nevertheless, the Euler method forms the basis of the Verlet integration scheme. [98]

Verlet algorithm

The Verlet algorithm is named after the french physicist Loup Verlet [92]. It is also known as Explicit Central Difference method and provides an improved but still simple form of the Euler method. Likewise, it is based on a truncated Taylor expansion of the position r around the time t similar to the one shown in equation 3.16. In contrast to the Euler method, third order terms are considered for the Verlet algorithm.

$$\begin{aligned} r\left(t+\Delta t\right) &= r\left(t\right) + v\left(t\right)\Delta t + \frac{F\left(t\right)}{2m}\Delta t^2 + \frac{\Delta t^3}{3!}\dddot{r}\left(t\right) + \mathcal{O}\left(\Delta t^4\right) \\ r\left(t-\Delta t\right) &= r\left(t\right) - v\left(t\right)\Delta t + \frac{F\left(t\right)}{2m}\Delta t^2 - \frac{\Delta t^3}{3!}\dddot{r}\left(t\right) + \mathcal{O}\left(\Delta t^4\right) \end{aligned} \tag{3.18}$$

By summation of these two equations for the forward and backward time evolution (equation 3.18), equation 3.19 is derived.

$$r\left(t+\Delta t\right) + r\left(t-\Delta t\right) = 2r\left(t\right) + \frac{F\left(t\right)}{m}\Delta t^2 + \mathcal{O}\left(\Delta t^4\right) \tag{3.19}$$

The reformulation of equation 3.19 leads to a formula which estimates the position at time $t+\Delta t$ via the preceding position $r\left(t-\Delta t\right)$ and the current values of the position and the force, $r\left(t\right)$ and $F\left(t\right)$.

$$r\left(t+\Delta t\right) \approx 2r\left(t\right) - r\left(t-\Delta t\right) + \frac{F\left(t\right)}{m}\Delta t^2 \tag{3.20}$$

Thus, the new position is computed without consideration of the velocity. However, the velocity can be estimated from the trajectory by evaluation of equation 3.21.

$$\begin{aligned} & r\left(t+\Delta t\right) - r\left(t-\Delta t\right) = 2v\left(t\right)\Delta t + \mathcal{O}\left(\Delta t^3\right) \\ \Rightarrow \quad & v\left(t\right) = \frac{r\left(t+\Delta t\right) - r\left(t-\Delta t\right)}{2\Delta t} + \mathcal{O}\left(\Delta t^3\right) \end{aligned} \tag{3.21}$$

After the new position is computed the position at time $t-\Delta t$ can be discarded whereas the current position becomes the proceding position for the next integration step. This results in the least possible memory consumption. In contrast to the Euler method the Verlet algorithm is both time-reversible and symplectic which results in good short and long-time energy conservation. [89, 90].

Leapfrog algorithm

The Leapfrog algorithm is a simple equivalent variation of the Verlet algorithm. In contrast to the Verlet integration scheme, the velocities are computed at half-integer time steps whereas the positions are still computed at integer time steps similar to the Verlet algorithm. The definition of the velocity is the same as it is for the Verlet algorithm, see equation 3.21.

$$\begin{aligned} v\left(t-\frac{\Delta t}{2}\right) &\equiv \frac{r\left(t\right)-r\left(t-\Delta t\right)}{\Delta t} \\ v\left(t+\frac{\Delta t}{2}\right) &\equiv \frac{r\left(t+\Delta t\right)-r\left(t\right)}{\Delta t} \end{aligned} \tag{3.22}$$

According to equation 3.23, the new position can be computed from the preceding position, the current position and the velocity in between. Thus, the positions and velocites are *leapfrogging* each other. The use of the midpoint velocities results in more accurate trajectories.

$$r\left(t+\Delta t\right) = r\left(t\right) + \Delta t v\left(t+\frac{\Delta t}{2}\right) \tag{3.23}$$

For the estimation of $v\left(t+\Delta t\right)$ equation 3.24 can be utilized which is derived from the basic Verlet scheme.

$$v\left(t+\frac{\Delta t}{2}\right) = v\left(t-\frac{\Delta t}{2}\right) + \frac{F\left(t\right)}{m}\Delta t \tag{3.24}$$

To sum up, the Leapfrog algorithm produces more accurate positions than the basic Verlet algorithm. However, the total energy cannot be computed directly because the positions and velocities are not available for the same steps in time. [89, 97]

Velocity Verlet algorithm

The Velocity Verlet algorithm is a method that uses the previously presented Leapfrog algorithm as a basis. A slight modification of the velocity updating as it is presented in [99] results in an integration scheme with simultaneously available positions and velocities. Thus, the total energy can be computed directly.

$$v\left(t+\Delta t\right) = v\left(t\right) + \frac{F\left(t+\Delta t\right)+F\left(t\right)}{2m}\Delta t. \tag{3.25}$$

According to [89] the Velocity Verlet algorithm is equivalent to the basic Verlet scheme. To conclude, Verlet type algorithms and especially the modified Velocity Verlet algorithm are suitable for most application in molecular dynamics simulations. They combine fair performance, low memory requirements and good accuracies and are easy to implement. [100]

3.2.5 Molecular dynamics at constant temperature

As already introduced in the context of spin dynamics simulations in chapter 3.1.4, the experimental situation for particle systems is usually explainable in terms of the canonical ensemble with constant number of particles N, volume V and temperature T. In order to keep the temperature of a real system constant, the system exchanges energy with a very large energy reservoir in equilibrium at a definite temperature. As the heat bath is much larger than the actual system it can be assumed that the system adopts the heat bath temperature without influencing it. Thus, in simulations, heat flow from and to the system must be enabled to control the system temperature. There are several canonical molecular dynamics methods such as the Andersen method [101], the Berendsen method [102], and the Nosé method in the formulation of Hoover [103] which is mostly used in molecular dynamics simulations. [104]
The Andersen method closely resembles the experimental situation. Experimentally, the particles of the system under consideration collide with the wall that separates the system from the heat bath. Thus, energy is exchanged between the system and the heat bath. The exchanged energy is then spread over the system by particle-particle collisions. This generally results in a distribution of configurations according to the canonical ensemble. Within the Andersen method, a constant system temperature is realized by replacement of the velocity of randomly chosen particles by a velocity that is drawn from a Maxwell distribution for the heat bath temperature. The equilibration time and the energy fluctuations are controlled by the collision rate of the particles. This procedure leads to a canonical distribution. [101]
In order to evaluate the expectation values of quantities that are independent of time and momentum, a canonical distribution in the positins $\mathbf{r}$ can be used.

$$\rho\left(\mathbf{r}\right) = e^{\frac{-U(\mathbf{r})}{k_B \cdot T}} \tag{3.26}$$

As the total kinetic energy of the system evolves towards the equilibrium value $\frac{3Nk_BT}{2}$ with only small fluctuations around it, the kinetic energy can be forced to a value that is exactly equal to the energy that corresponds to the temperature T. Hence, the narrow energy distribution can be replaced by a delta function.

$$\rho\left(E_{kin}\right) \rightarrow \delta\left[E_{kin} - \frac{3\left(N-1\right)k_B T}{2}\right] \tag{3.27}$$

This can be realized by rescaling the velocities after every integration step.

$$\mathbf{v}_i\left(t\right) \rightarrow \lambda \cdot \mathbf{v}_i \quad \text{with } \lambda = \sqrt{\frac{3\left(N-1\right)k_B T}{\sum_{i=1}^{N} m v_i^2}} \tag{3.28}$$

Besides this velocity rescaling approach, other methods have been developed that realize the coupling of the system and the heat bath by an additional force as it was already shown by the Langevin-like approach in chapter 3.1.4. In this approach, friction is assumed to be proportional to the particle velocity resulting in a canonical distribution. A particular formulation of the friction coefficient ζ has been proposed by Berendsen et al. [102].

$$\zeta = \gamma\left(1 - \frac{T_D}{T}\right) \tag{3.29}$$

In this equation, γ represents a constant factor, T denotes the actual temperature that is evaluated by the kinetic energy, whereas T_D denotes the desired temperature that is provided by the heat bath. With the Berendsen method of temperature control the temperature decays exponentially towards the heat bath temperature resulting in usually fast relaxation processes. On the downside, this method is neither time-reversible nor does it provide a full canonical description.

A purely canonical and time-reversible method is given by the reformulation of Hoover of the so-called Nosé method. Here, an artificial variable is introduced that realizes the heat bath as an integral part of the system. The friction parameter ζ, expressed in terms of a differential equation, is associated with a virtual mass Q that determines the coupling between the system and the heat bath.

$$\frac{d\zeta}{dt} = \frac{1}{Q}\left(\sum_i v_i^2 - 3Nk_B T_D\right) \tag{3.30}$$

For large values of Q, a weak coupling is realized whereas a tight coupling is achieved for small values of Q. The value of Q must be chosen with care in order to keep the simulation time small, to avoid artificial high-frequency temperature fluctuations, and at the same time realize a good temperature control.

To summarize, constant temperature molecular dynamics simulations can be realized by different methods such as Andersen velocity scaling and Berendsen or Nosé-Hoover friction. The Andersen method provides a very simple way to control the temperature but it does not allow temperature fluctuations as they are present in the canonical ensemble. The Berendsen method follows a different approach, realizes temperature fluctuations, and results in a fast relaxation of the system in simulation but it is not time-reversible and does not provide a full canonical description. The Nosé-Hoover method is associated with a time-scaling that is rather unintuitive but it provides a time-reversible and fully canonical description. Hence, for the most molecular dynamics simulations, the Nosé-Hoover method or a combination of Berendsen and Nosé-Hoover methods is used. [104–106]

3.2.6 Classical molecular dynamics summary

To sum up, classical molecular dynamics provides a method to compute the trajectories of particles that interact by classical potential functions. Here, the motion of magnetic nanoparticles that is induced by magnetic dipole-dipole interactions is considered together with a viscous drag due to a liquid or gel-like matrix material. Moreover, a classical potential formulation is used to realize hard sphere dynamics. By definition, the orientations of the magnetic moments of the particles are not considered here and, thus, are assumed to be fixed for a small time interval which is subject of chapter 6.
All molecular dynamics simulations in this work are performed with the open-source software package HOOMD-blue [107–109]. HOOMD-blue provides a general-purpose program package for particle simulations with integrators for different ensembles, input/output options and standard potential formulations. It is highly customizable because of its modular structure. As a customization, major changes have been implemented in HOOMD-blue in order to realize a simulation environment for magnetically interacting particles. Standard molecular dynamics applications involve isotropic potential functions, i.e. the potential only depends on the scalar particle-particle distance. Because the magnetic dipole-dipole interaction is highly anisotropic, the scalar handling of the distances has been changed to a full vectorial treatment. Furthermore, the magnetic dipole-dipole interaction potential has been included in the HOOMD-blue code.
The most important change to the original HOOMD-blue is the inclusion of the spin dynamics algorithm that is presented above for simultaneous spin dynamics simulations for hybrid molecular and spin dynamics simulations which will be presented in detail in chapter 6. In addition to that, a new output format has been included. In order to

display the moving magnetic nanoparticles together with their changing magnetic moment orientations, a x3d output format for the *instantreality* framework [110] has been implemented.

3.2.7 Reduced Lennard-Jones Units

In contrast to the spin dynamics algorithm that is used in this work, the molecular dynamics tool HOOMD-blue does not utilize SI units. Instead of this, reduced Lennard-Jones units are used for input, processing, and output. The reduced Lennard-Jones units provide a full set of generic units. In order to improve the numerical performance, the precision of floating point calculations can be maximized by scaling important quantities to the order of 1. Therefore, the fundamental units m_u (mass), d_u (distance), and E_u (energy) are defined to match the problem and all other units are derived from these fundamental units. Throughout this work, the following set of fundamental units is used in order to ensure good performance and intuitive data input.

$$\begin{aligned} m_u &= kg \\ d_u &= 10^{-9}\ m \\ E_u &= J \end{aligned} \tag{3.31}$$

Examples of derived units are shown in the following equations. The time unit τ is expressed by all three fundamental units. The unit v_u corresponds to the velocity by dividing the unit of distance by the unit of time and F_u represents the reduced unit of force by dividing the unit of energy by the unit of distance.

$$\begin{aligned} \tau &= \sqrt{\frac{m_u d_u^3}{E_u^2}} \\ v_u &= \frac{d_u}{\tau} \\ F_u &= \frac{E_u}{d_u} \end{aligned} \tag{3.32}$$

The magnetic units M_u of the magnetization and μ_u of the magnetic moment can be derived from the fundamental units in the same manner.

$$\begin{aligned} M_u &= \sqrt{4\pi\epsilon_0 \frac{E_u^2}{M_u D_u^3}} \\ \mu_0 &= \sqrt{4\pi\epsilon_0 \frac{E_u^2 D_u^3}{M_u}} \end{aligned} \tag{3.33}$$

The actual conversion factors can be identified by inserting the chosen fundamental units in equation 3.31 into the derived units in equations 3.32 and 3.33. This system is compatible to the SI system of the spin dynamics algorithm. However, the conversion factors must be considered for the data exchange and the input files.

4 Design of model systems

The simulations that are shown in this work are performed on model structures which consist of clearly defined ensembles of magnetic nanoparticles. In order to design model structures that serve as input for simulations, one has to compromise between the computational effort of the simulation and the realism of the structure under consideration. On the one hand, one wants to investigate systems that are as close to the experimental situation as possible in order to obtain realistic results, i.e. realistic nanoparticle structures and realistic magnetic and magnetoresistive properties. On the other hand, the simulation has to be performed with limited computing resources. Therefore, a simplification of real, experimental structures to model structures is required.

4.1 Experimental systems

For the experimental investigation of the magnetoresistive properties of systems that are based on magnetic nanoparticles that are immersed in a conductive gel matrix, obviously, samples have to be prepared. Therefore, different matrix materials can be used. As shown in [5, 6, 111], a commonly used matrix material is agarose. Agarose is an extract of seaweeds which can be used for the formation of hydrogel matrices. The long agarose molecules therefore interweave when boiled up and subsequently cooled down in a buffer. As the reticle of the gel is formed by hydrogen bonds, the gelatinization process is reversible. For common agarose concentrations, gelling temperatures can be found in the range between 32 °C and 45 °C while melting temperatures can be found in the range between 80 °C and 95 °C. Figure 4.1 shows two sample systems that use 2% agarose as gel matrix together with cobalt particles with a concentration of 0.03, i.e. the ratio of the particle mass over the gel mass equals 0.03. After the gel is heated and thus liquefied, the particles are mixed in by stirring. Afterwards, the particles undergo a self-assembly process. In addition to that, the nanoparticles can be structured by means

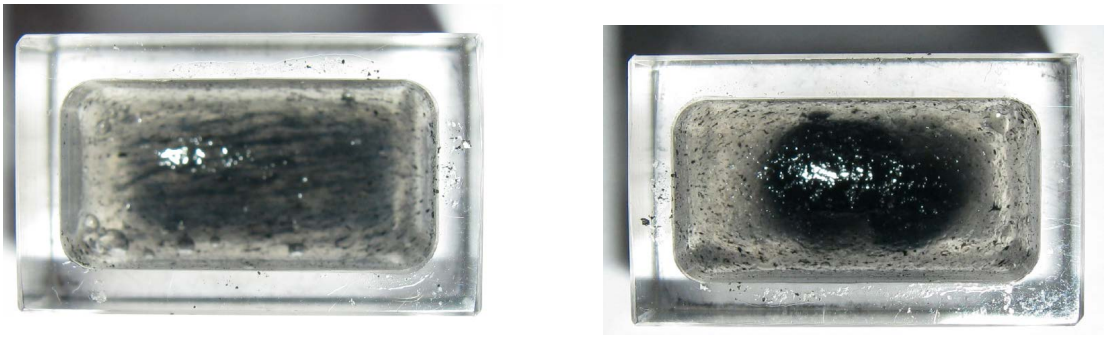

(a) (b)

FIGURE 4.1: Sample systems consisting of a 2% agarose gel matrix and cobalt nanoparticles with a particle concentration of 0.03. In addition to the particle self-assembly due to the magnetic dipole-dipole interaction between the particles and viscous interaction with the gel matrix, homogeneous (a) and rotating (b) external magnetic fields can be utilized to structure the system. The particle-gel mixture is stored in a samples vessel that is made of acrylic glass and measures 2 $cm \times 1.2$ cm [6, 111].

of an external magnetic field. A system that is prepared in a homogeneous external magnetic field is shown in figure 4.1(a) whereas figure 4.1(b) shows a sample that has been prepared in an in-plane, rotating magnetic field. The samples are stored in vessels that are made of acrylic glass and measure 2 $cm \times 1.2$ cm [6, 111].

There are two possible ways to simplify these experimental systems in order to obtain model structures that can be simulated numerically. Experimentally, three-dimensional reconstruction techniques can be used to determine the real particle constellation that is achieved under particular experimental conditions. On the other hand, one can abstract from experimental findings, i.e. particle concentrations and gel viscosities, and create model structures theoretically. Whereas the first method provides a very precise way to convert real systems to *in silico* systems, the second method is a very basic and hence a less time-consuming way.

4.2 3D reconstruction of nanoparticle ensembles

As introduced in [111, 112], a 3D reconstruction of systems of magnetic nanoparticles that are immersend in a gel matrix can be performed in order to obtain detailed topological information. All 3D reconstructions that are shown here have been performed by Thomas Rempel at Bielefeld University. First results have been published in [112] and a detailed discussion will be published in [111].
For the 3D reconstruction, a dual method is used. This method involves a scanning electron microscope (SEM) and a focused ion beam (FIB). It has been shown in [111, 112] that the SEM can be used to take images of the surface of the nanoparticle system by

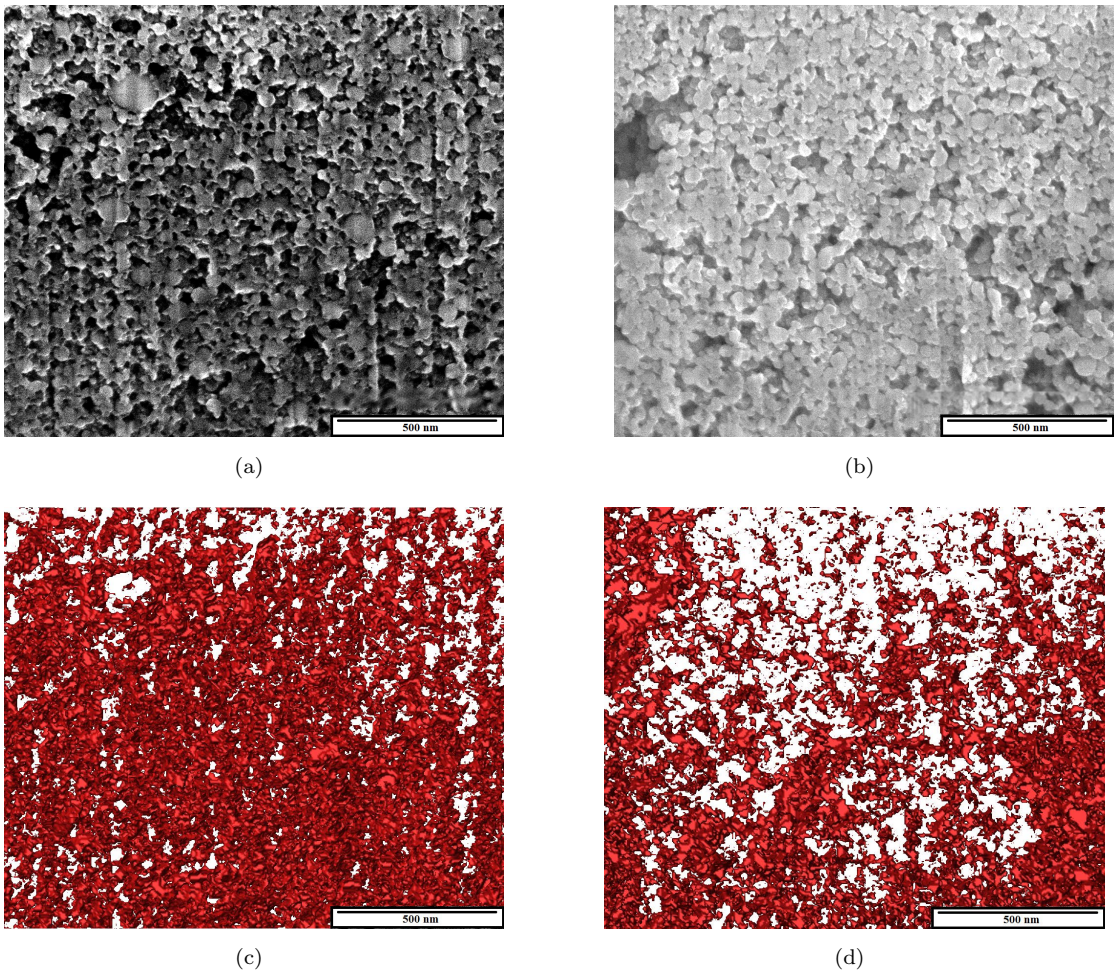

(a) (b)

(c) (d)

FIGURE 4.2: SEM images of the surface of a sample A that is prepared in a homogeneous external magnetic field (a) and the surface of a sample B that is prepared in a rotating magnetic field (b). The corresponding 3D reconstructions from SEM slice images are shown in (c) for sample A and (d) for sample B. [111, 112]

scanning with a focused beam of electrons. At the same time, the FIB is used at a high beam current to successively cut away thin slices. Afterwards, the SEM images can be used for a 3D reconstruction of the particle microstructure. For this dual method, the samples as shown in figure 4.1 have to be freeze-dried. As a consequence of the freeze-drying process the samples lose their conductivity. Because conductivity is required for the further process, the samples are then coated by a thin gold layer.

After the dual FIB-SEM method is performed, one has access to a full set of 2D images of the system's slices that can be used for a complete 3D reconstruction with a particular software package. Sample SEM images and 3D reconstructions for the two kinds of systems from figure 4.1 are shown in figure 4.2. In the 3D reconstructions, the gel matrix is displayed in red whereas the particles are left out for the sake of clearness. From the 3D models, it is possible to measure the particle positions and diameters in layers that can be used as input for simulations. Figure 4.3 shows an exemplary particle

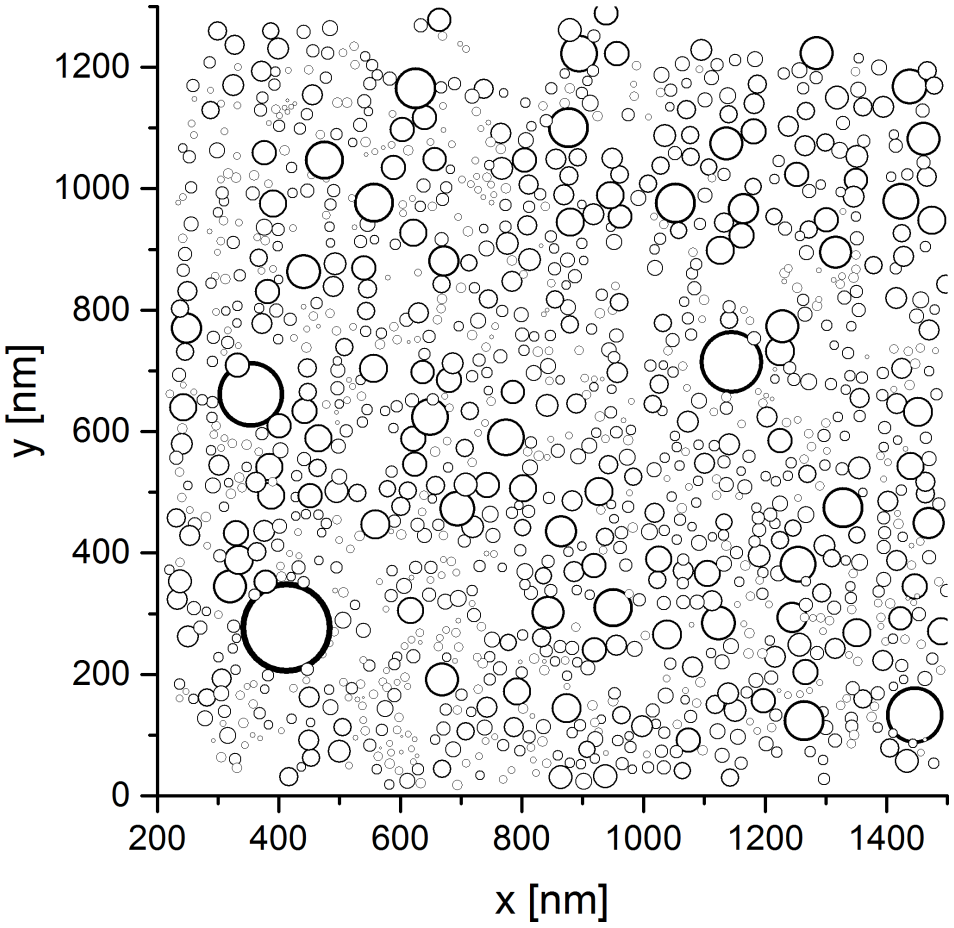

FIGURE 4.3: Two-dimensional magnetic nanoparticle structure. The particle positions and diameters are measured from one layer of a real, 3D reconstructed system that has been imported by means of a dual FIB-SEM method. The positions and diameters can be used as input for spin dynamics or hybrid molecular and spin dynamics simulations.

configuration that has been generated by means of the 3D reconstruction of a real system similar to the one in figure 4.1(a). Therefore, one section of one layer of the 3D reconstruction has been measured particle by particle. The resulting particle positions and diameters can be used as input data for spin dynamics or hybrid molecular and spin dynamics simulations. It should be noted that this technique is usually performed on one section of the experimental system instead of the whole system because of the technical efforts. In this example, an area of about $1500 \times 1500\ nm$ is considered. In conclusion, this method provides a very precise way to determine particle positions and diameters in systems that are prepared by different methods. On the downside, the effort is huge. In the next section, a less elaborate approach is introduced.

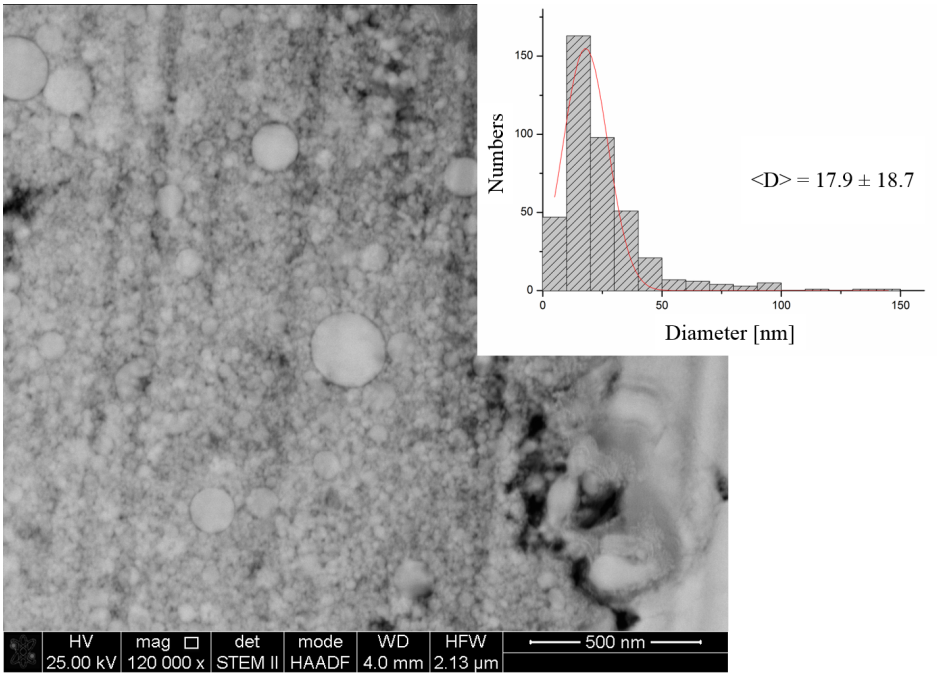

FIGURE 4.4: Experimental system consisting of cobalt particles that are embedded in an agarose matrix. STEM image of the Co core / conductive C-shell nanoparticle configuration that is used for AC GMR measurements and the particle size distribution (inset). This figure is reproduced from [112].

4.3 Structure determination by abstraction and downsizing

As stated in section 4.1, an alternative method to create particle ensembles for the simulation is provided by the abstraction and simultaneous downsizing of experimentally observed properties such as particle size distributions and matrix viscosities. The particle size distribution can be determined from images similar to the one shown in figure 4.4 [112]. From the size distribution and the concentration, it can roughly be concluded on the arrangement of the particles in the gel. With this information, model structures can be constructed. In order to generate systems, that are easy to compute, only a small number of particles should be included. In a second abstraction step, one particle size can be chosen instead of a size distribution. It has been shown in [112] that in this way one is able to build very simple model structures that are easy to compute and at the same time resemble the properties of real, complex structures. For the system that is shown in figure 4.4, a very simple model structure was designed which is named AH41 in the following. AH41 consists of 200 monodisperse cobalt particles with equal diameters of 20 nm as shown in figure 4.5. The particles are spatially distributed over an area of 350×350 nm.

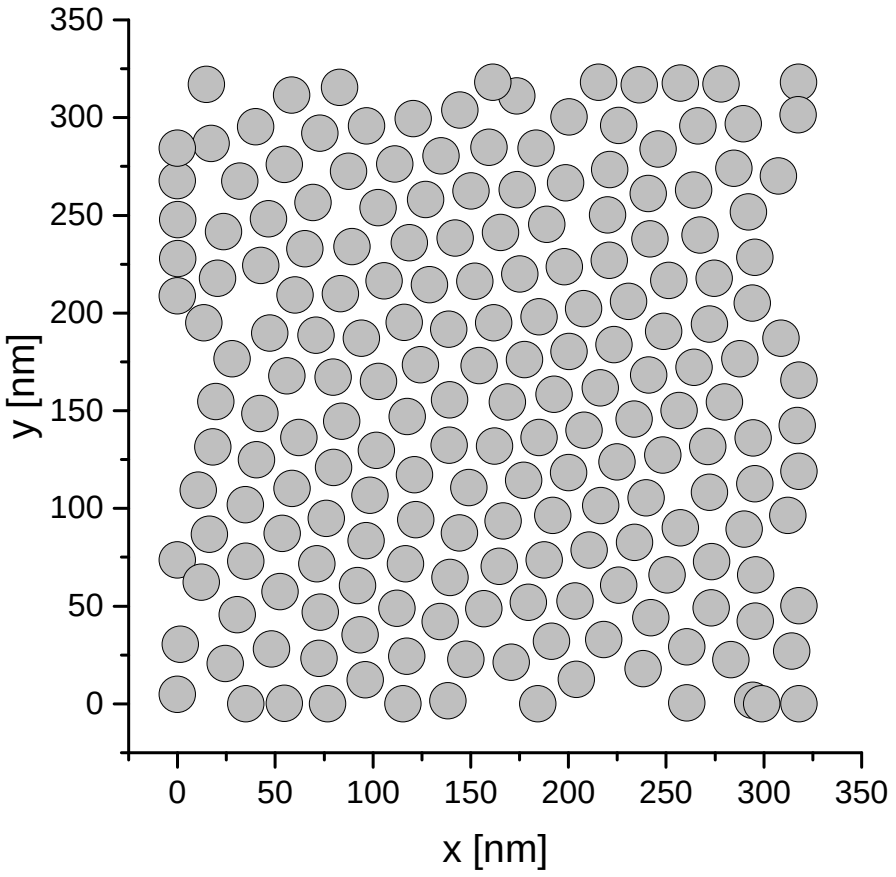

FIGURE 4.5: Sample structure AH41 containing 200 monodisperse cobalt particles with $d = 20\ nm$ distributed over an area of $350\ nm \times 350\ nm$. The structure resembles experimentally produced systems. [72]

4.4 Design of model systems summary

In general, simulations can be performed on arbitrary particle configurations. The particle positions and sizes can precisely be determined by means of 3D reconstruction techniques. As real systems consist of a huge number of particles, simulations require considerable computational efforts. Therefore, simplified model structures with a small number of particles can be constructed by abstraction of experimentally obtained crucial quantities such as the particle size distribution and concentration.

5

Efficient calculation of magnetic low energy configurations of nanoparticle ensembles

Preliminary numerical investigations of model structures of magnetic nanoparticles have shown that their topological disorder leads to geometric frustration. Hence, not all interaction contributions can be minimized at the same time. As introduced in chapter 2.1.2, the nanoparticle ensembles behave like magnetic dipole glasses. The numerical investigation of frustrated systems is associated with special characteristics. Here, an experimentally inspired demagnetization routine is used to drive the system efficiently towards its low energy configurations. The total energies that are achieved by this method are even lower than the total energies that are derived by conventional relaxation simulations. The results that are presented here have been published in [72] and [112].

5.1 Basic relaxation simulations

Classical spin dynamics simulations as introduced in chapter 3.1 reveal one single magnetic ground state, i.e. one particular configuration of the magnetic moment orientations with the minimum total energy possible, for unfrustrated systems at $T = 0\ K$. As expected, the topological disorder causes geometrical frustration. Hence, spin dynamics simulations for random initial configurations result in a multitude of low energy configurations with similar total energies but structural differences. For the model structure AH41, four exemplary configurations are shown in figure 5.1. From these configurations, it becomes apparent that the energy landscape of the magnetic dipole-dipole energy features a large quantity of local energy minima that are separated by energy barriers. These barriers cannot be overcome by the simple relaxation procedure. Hence, the configuration effectively "gets stuck" in one of these local energy minima without any possibility of leaving it in favor of a lower energy minimum. The total energies that are

calculated for the structure under consideration differ by approximately 2%. However, the orientations of the magnetic moments are obviously different. So far, it remains unclear wether other energy minima with even lower total energies exist.
A first approach for this problem is to cool the system from a high initial temperature to $T = 0\ K$ during the simulation. As introduced in chapter 3.1.4, a Langevin approach is used to couple the magnetic system to an external heat bath. Due to this heat bath coupling, the magnetic moments fluctuate undirectedly with a white noise characteristics. These fluctuations are capable of lifting the magnetic system out of a local energy minimum which opens up the possibility of finding another, lower energy configuration.
A more sophisticated approach is to use a time-dependent magnetic field instead of a varying temperature which is presented in the following.

5.2 Demagnetization protocol

The complex behavior of systems of magnetic moments with geometrical frustration can be observed experimentally as well. As reported in [113] in the context of artificial spin ice, demagnetization protocols can be used to drive magnetic ensembles into low energy states very efficiently. In common demagnetization measurements [114, 115] the magnetic sample is rotated in an alternating, damped, in-plane external magnetic field. In doing so, the magnetic moments are rapidly agitated. Hence, the strong magnetic dipole-dipole bonds can be broken down to open up the possibility of reaching another low energy configuration.
In this work, a rotating, damped, sinusoidal magnetic field is used numerically to drive frustrated systems in low energy states more efficiently, in analogy to the experimental investigations of [113–115]. For the sake of simplicity, instead of rotating the magnetic sample in the external field, the field is rotated around the sample. The external magnetic field is calculated according to the following equations in every step in time of the spin dynamics simulation. The damping of the magnetic field is considered in equation 5.1 by means of the damping parameter τ.

$$B_{0,damped} = B_0 \cdot exp\left(-\tau \frac{t_{current}}{t_{total}}\right), \tag{5.1}$$

with $t_{current}$, the current time step, t_{total}, the total number of time steps and B_0, the amplitude of the external field. The frequency of the magnetic field per simulation run is specified by the parameter f which is used to calculate β.

$$\beta = 2 \cdot \pi \cdot f \cdot \frac{t_{current}}{t_{total}} \tag{5.2}$$

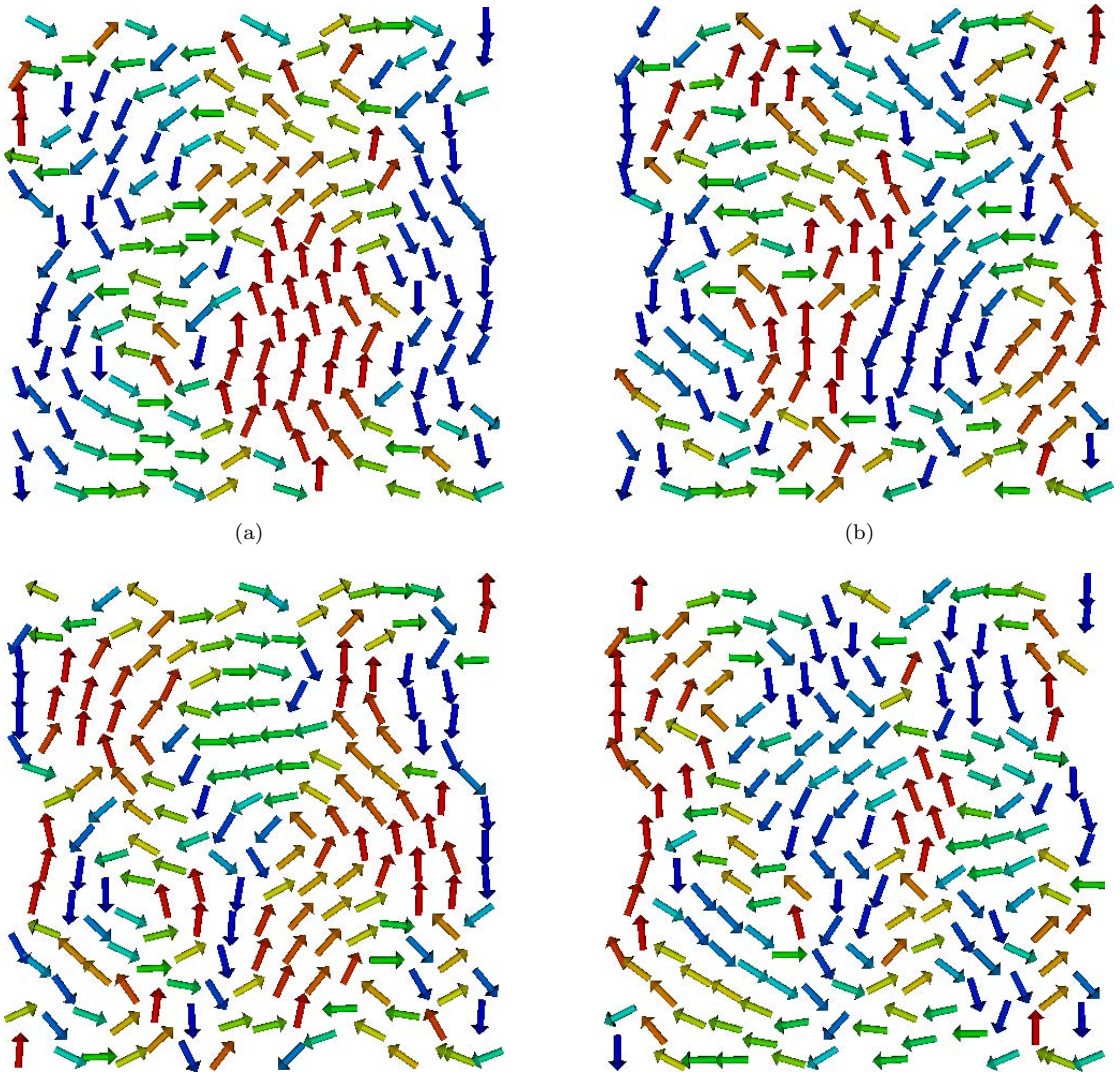

FIGURE 5.1: Examples of low energy configurations of structure AH41 obtained by classical spin dynamics simulations at $T = 0\ K$. The arrows represent the magnetic moments of the particles. The resulting total energies that are calculated after the magnetic moment configuration does not change with time any longer are (a) $-3.78467 \cdot 10^{-16}\ J$, (b) $-3.75635 \cdot 10^{-16}\ J$, (c) $-3.79583 \cdot 10^{-16}\ J$, and (d) $-3.3.72457 \cdot 10^{-16}\ J$. In all subfigures, the coloring of the magnetic moment vectors indicates the in-plane component. (This figure is reproduced from [72].)

The azimuthal and polar angles α and γ are calculated as follows with N_α, the number of azimuthal turn per simulation rund and N_γ, the number of polar turns per simulations run.

$$\alpha = N_\alpha \cdot 2 \cdot \pi \cdot \frac{t_{current}}{t_{total}} \tag{5.3}$$

$$\gamma = N_\gamma \cdot 2 \cdot \pi \cdot \frac{t_{current}}{t_{total}} \tag{5.4}$$

The three-dimensional orientation of the external magnetic field can finally be calculated by the following equations.

$$\begin{aligned} B_x &= B_{0,damped} \cdot \sin\alpha \cdot \cos\gamma \cdot \cos\beta \\ B_y &= B_{0,damped} \cdot \sin\alpha \cdot \sin\gamma \cdot \cos\beta \\ B_z &= B_{0,damped} \cdot \cos\alpha \cdot \cos\beta \end{aligned} \tag{5.5}$$

The progression of the absolute external field and its x-component for exemplary parameters is shown in figure 5.2. This demagnetization protocol has been included in the spin dynamics algorithm that is presented in section 3.1 in order to investigate the model structure AH41. Therefore, in analogy to section 5.1, each magnetic moment is assumed to carry one effective magnetic moment of $\mu_{eff} = 641371.18\ \mu_B$. The magnetic moments are then exposed to an external magnetic field that follows the demagnetization protocol. Exemplary results are shown in figure 5.3. Therefore, the parameters in table 5.1 have been used for the demagnetization protocol.

TABLE 5.1: Parameters of the demagnetization protocol for AH41

N_α	7
N_γ	3
f	30
B_0	0.05 T
τ	6

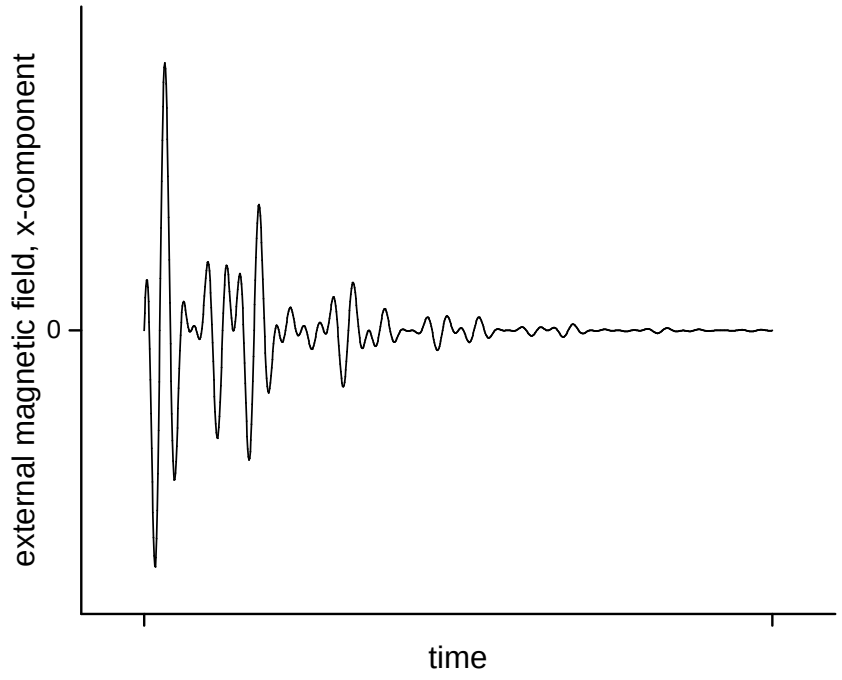

(a)

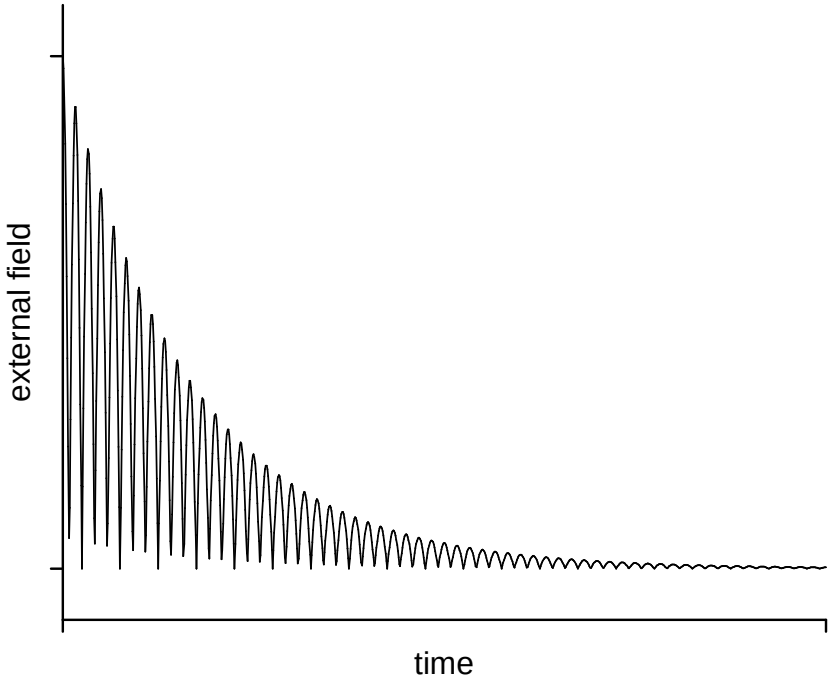

(b)

FIGURE 5.2: Qualitative characteristics of the demagnetization protocol. The frustrated magnetic system is exposed to a damped, sinusoidal, and rotating external magnetic field. Here, the x-component of the external field (a) and the absolute value (b) are shown for exemplary parameters.

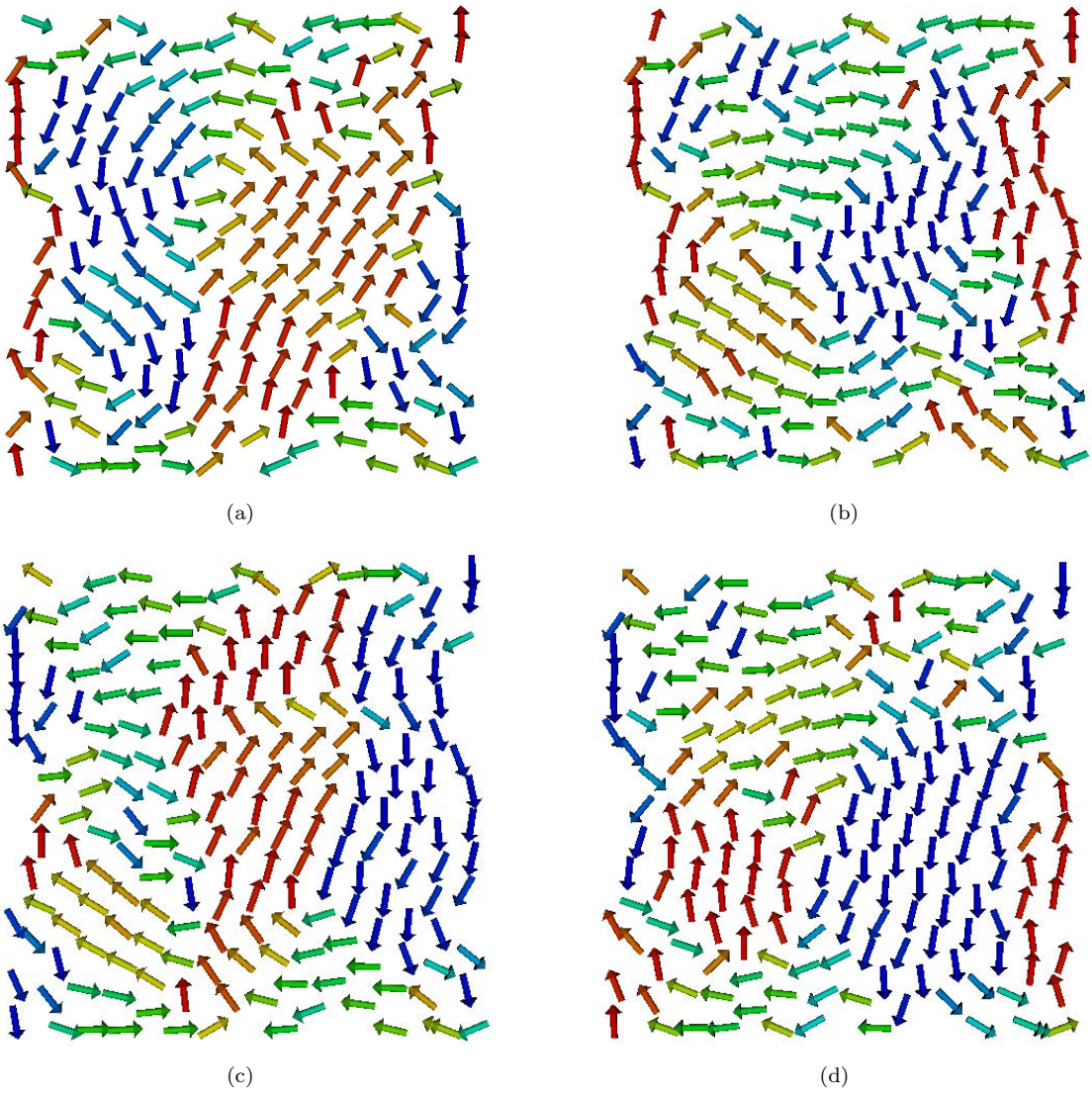

(a) (b) (c) (d)

FIGURE 5.3: Exemplary results of simulations of the model structure AH41. Here the external magnetic field follows the demagnetization protocol which is shown in figure 5.2. The parameters are specified as follows: $N_\alpha = 7$, $N_\gamma = 3$, $f = 30$, $B_0 = 0.05T$, and $\tau = 6$. The resulting energies are (a) $-3.82643 \cdot 10^{-16}J$, (b) $-3.83821 \cdot 10^{-16}J$, (c) $-3.81961 \cdot 10^{-16}J$, and (d) $-3.83900 \cdot 10^{-16}J$. In all figures, the coloring of the magnetic moment vectors indicates the in-plane component of the magnetic moment. (This figure is reproduced from [72].)

5.3 Comparison of simple relaxation and demagnetization protocol

The resulting low energy configurations of both approaches, the simple relaxation and the demagnetization protocol, can be compared qualitatively in terms of the final magnetic moment orientations and quantitatively in terms of the resulting total energies. Qualitatively, it becomes apparent that the simple relaxation procedure leads to magnetic moment orientations that consist of several small vortices. In contrast to that, simulations with a small external magnetic field that follows the demagnetization protocol lead to final configurations of the magnetic moments that consist in principle of one large magnetic moment vortex with some smaller vortices at the boundaries. Two exemplary configurations of the model structure AH41 for the two simulation methods are shown in figure 5.4. Quantitatively, the total energies of the final low energy configurations are compared in figure 5.5. In this figure, there is a marked difference between the total energies that result from the two simulation approaches. Figure 5.5 shows a statistical evaluation of 1000 simple relaxation simulations that are compared to 1000 simulation runs that use the demagnetization protocol. The energy values that are displayed here are the total energies that are calculated for the final configurations of the magnetic moments that do not change with time any longer. Whereas the resulting total energies of the simple relaxation procedure show a broad distribution, the demagnetization protocol leads to a much narrower distribution of the total energies. Moreover, the total energies that are calculated by the demagnetization protocol are overall significantly lower than the results of the simple relaxation procedure.

5.4 Demagnetization simulations summary

Ensembles of magnetic nanoparticles with spatial disorder have sophisticated properties because the magnetic dipole-dipole energy landscape consists of a great number of local energy minima that are separated by energy barriers. Simple relaxation simulations by means of stochastic spin dynamics simulations show that during the relaxation procedure, the configuration of the magnetic moments of the particles enters one of the local energy minima. Because the energy minima are separated by energy barriers, the configuration gets stuck figuratively. Therefore, lower, “better” configurations cannot be reached. This happens in simulations as well as in experimental investigations. Thus, nature and theory encounter the same issues.
In order to increase the efficiency of the procedure, the magnetic sample can be exposed to an alternating external magnetic field. Hence, the magnetic moments are agitated

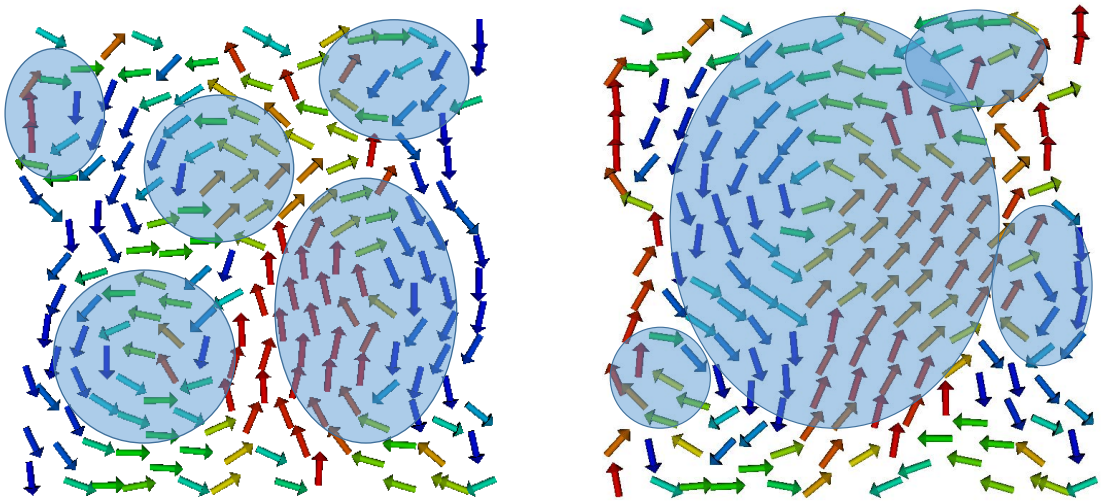

(a) (b)

FIGURE 5.4: Qualitatively, differences in the magnetic moment orientations can be identified between the results of simple relaxation simulations and simulations with a demagnetization protocol. Simple relaxation simulations mostly result in low energy configurations that consist of several small vortices of the magnetic moments (a). In contrast to that, simulations that utilize a demagnetization protocol produce low energy configurations that contain in principle one large magnetic moment vortex (b). In both figures, the vortices are highlighted in blue.

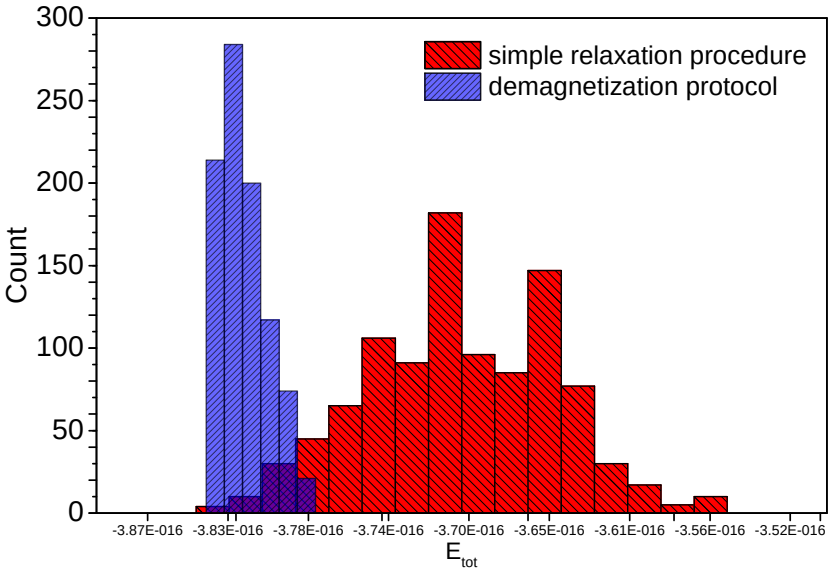

FIGURE 5.5: Statistical evaluation of 1000 simulation runs that follow the simple relaxation procedure and 1000 simulation runs that utilize the demagnetization protocol. Comparing the final low energy configurations, the total energies that are achieved by the demagnetization protocol are overall lower than the total energies from the simple relaxation procedure. In addition to that, the distribution of the total energies is much narrower for the simulation results of the demagnetization protocol.

and the energy barriers can be overcome in order to reach lower energy configurations. Here, it is shown that besides reducing the overall total dipole-dipole energy, the distribution of the total energies is much narrower and clearer. The experimental technique can be expanded to the simulation method with good results.

6 Hybrid molecular and spin dynamics simulations

In order to estimate the GMR properties of ensembles of magnetic nanoparticles in viscous matrices, the complete structuring process of the particles in their environment must be considered. In analogy to experimental investigations, the particle data, i.e. the number of particles, the size distribution, and the material data is given. The particles can be initialized with random or specific coordinates. Theoretically and experimentally, the particles then undergo a self-assembly process due to their magnetic dipole-dipole interactions until a stable final configuration is reached. Afterwards, the GMR curves can be measured experimentally or they can be calculated from simulated magnetization curves. In order to define general features such as particle densities, size distributions or matrix viscosities that lead to favorable GMR properties, information about the magnetic microstructure is required. As information about the single magnetic moment orientations of the particles cannot be provided experimentally, numerical simulation is a crucial tool to identify these features. Here, a hybrid molecular and spin dynamics method is presented that considers the magnetic and the mechanical degrees of freedom of ensembles of magnetic particles in viscous matrices quasi-simultaneously. In contrast to other hybrid molecular and spin dynamics methods [116–119], a purely classical approach is used in this work.

6.1 Motivation

The self-assembly of magnetic particles and the structuring with external magnetic fields attracts a lot of interest because of the versatile applications. Magnetic nanoparticles can be used as building blocks for complex nanostructured materials such as data storage

materials with high densities, nanoscaled electronic devices, sensor systems, and medical applications such as targeted drug delivery. There are two main classes of methods to fabricate nanostructured magnetic materials. The first class of methods follows a top-down approach and therefore the nanostructured material is created by using successively finer tools on bulk materials. Important methods for the top-down construction of nanostructured materials are focused ion beam and lithographic techniques such as electron beam lithography or photolithography. In the second class of methods, the opposite approach is taken and the nanostructured material is created bottom-up by assembling atoms, molecules or particles to create complex, functional structures. Here, the assembly of the building blocks can be directed or undirected. Within the directed assembly, external forces are applied to the particles. On the other hand, the undirected assembly is driven by the intrinsic properties of the particles. Self-assembly processes can be found in atomic, ionic, and molecular crystals, liquid crystals and lipid bilayers. The self-assembly is usually caused by van der Waals interactions, hydrogen bonding or electromagnetic dipole interactions [120]. As shown in figure 6.1, new functional materials for applications in electronics, optoelectronics, thermoelectrics and many more can be generated by self-assembly processes [121]. For systems of magnetic particles, the particles self-assemble by means of magnetic dipole-dipole interactions or can be directed by means of external magnetic fields. [122–125]

In order to investigate the self-assembly process of magnetic nanoparticles in viscous media in detail, a combination of experimental and numerical techniques must be applied because the detailed magnetic structure remains hidden in experiments [112]. As stated in the introduction, in order to simulate moving magnetic moments, the spin and mechanical equations of motion must be solved simultaneously which can be done by molecular and spin dynamics techniques. There are different hybrid molecular and spin dynamics approaches presented in the literature. In [116, 126], a coupling of the spin and electronic degrees of freedom is realized in an *ab initio*, atomistic method. A magneto-mechanical coupling is realized in [117, 127, 128]. Therein, the spin degrees of freedom are included as additional degrees of freedom in an *ab initio* molecular dynamics framework. Another hybrid molecular and spin dynamics method is presented in [118] where a reformulation of molecular dynamics that includes spin and lattice dynamics degrees of freedom is provided. Moreover, another atomistic approach is presented in [119]. In summary, there are hybrid molecular and spin dynamics methods reported in the literature. However, these methods are *ab initio* methods following an atomistic approach which is not reasonably applicable to systems of magnetic particles on the nanoscale. For the purpose that is pursued in this work, a classical approach must be followed. Moreover, a coarse-grained approach is to be preferred over an atomistic approach in order to use the resources at best. On the other hand, there are methods to simulate

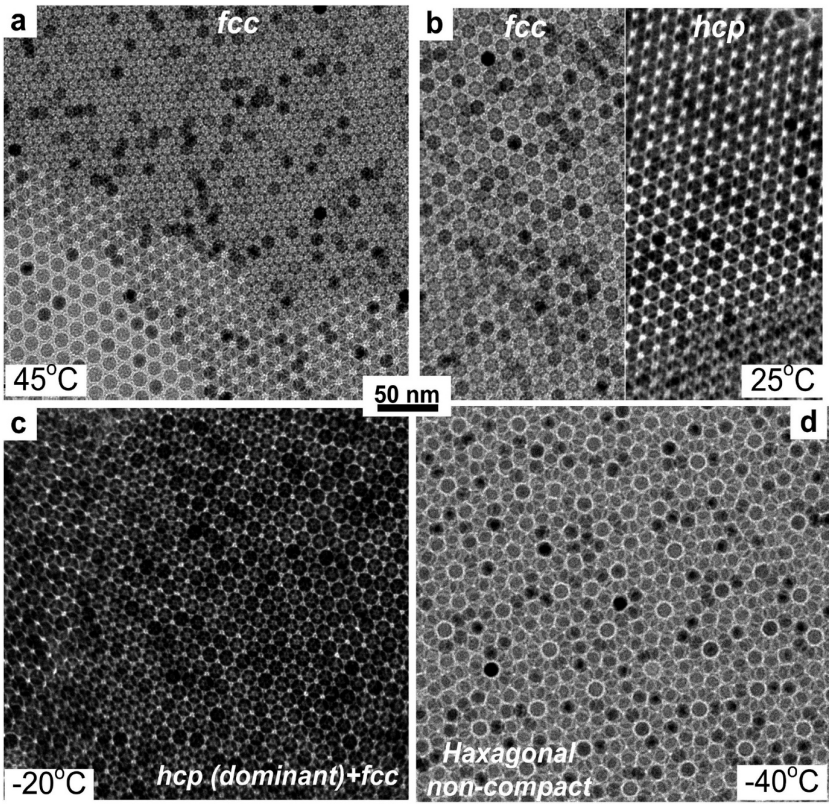

FIGURE 6.1: TEM images of superlattices self-assembled from chloroform solutions of 11 nm $Fe_xO/CoFe_2O_4$ nanocrystals at different temperatures: (a) face-centered cubic structure was formed at 45 °C; (b) face-centered cubic and hexagonal close-packed structures were formed at 25 °C; (c) hexagonal close-packed structures were dominant at −20 °C; and (d) non-close-packed structures were formed at −40 °C. Published in [121]. Copyright © 2010 American Chemical Society.

magnetic nanoparticles in solution that are not hybrid molecular and spin dynamics methods. Most of these methods follow the same approach. The most important examples for this approach are presented in [129–132]. Basically, all of these methods utilize Brownian dynamics simulations of magnetic particles under the assumption of frozen magnetic moments inside the particles. Hence, the orientation of the magnetic moment relative to the orientation of the magnetic particle does not change. Another approach is introduced in [133] where the magnetic moments are not frozen inside the particles but the spin degrees of freedom are included in the molecular dynamics code. In this approach, a Barnes-Hut algorithm is used to compute the particle trajectories. All these methods have in common that they make use of very strongly simplified approaches for the magnetic degrees of freedom whereas the molecular dynamics approaches for the mechanical part are very complex and sophisticated. As introduced in chapter 3.1, spin dynamics is the tool of choice for the simulation of the magnetic configuration. Thus, a hybrid molecular and spin dynamics method benefits from the advantages of both worlds. According to current knowledge, there is no other hybrid method of this kind reported in the literature. The content of this chapter is partly published in [112, 134].

6.2 Separation of the magnetic and mechanical degrees of freedom

The combination of spin dynamics and molecular dynamics in a new hybrid algorithm as it is presented in this work is based on the assumption that the mechanical and the magnetic relaxation processes occur on time scales that are clearly separated. Therefore, spin dynamics and molecular dynamics can be used consecutively instead of a thoroughly simultaneous coupling. It was proposed in [135] that for colloidal dispersions the time scale of the colloidal particles and the time scale of their internal degrees of freedom can be clearly separated, similar to the well-known Born-Oppenheimer approximation [136]. In analogy to [135], here, the magnetic and mechanical degrees of freedom can be treated separately. In order to validate this assumption for the problem that is considered here, the relaxation times of these two classes of degrees of freedom are specified in the following.

6.2.1 Mechanical relaxation of magnetic particles in a viscous matrix

The mechanical relaxation can be determined by the so-called configurational relaxation time τ_{cr}. The configurational relaxation time is defined as the time that a spherical particle in a liquid medium needs to diffuse across its own radius and can be calculated according to equation 6.1. This time τ_{cr} can be considered as the least time required for a change in the configuration of colloidal particles.

$$\tau_{cr} = \frac{\eta_m d_p^3}{k_B T} \tag{6.1}$$

In equation 6.1, η_m denotes the dynamic viscosity of the liquid medium and d_p denotes the particle diameter. [137–139]

6.2.2 Magnetic relaxation

The relaxation of the magnetization of colloidal magnetic particles occurs by two different mechanisms. On the one hand, the particle itself can rotate in the liquid medium as shown in figure 6.2(a). The characteristic time that is associated with this relaxation mechanism is called Brownian rotational diffusion time τ_B and can be estimated according to equation 6.2.

$$\tau_B = \frac{3 V_p \eta_m}{k_B T} \tag{6.2}$$

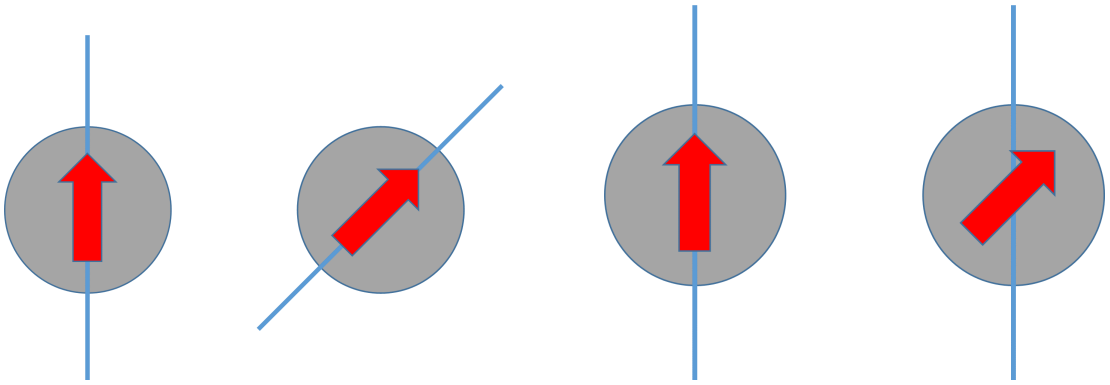

FIGURE 6.2: The relaxation of homogeneously magnetized particles in liquid matrices is caused by two different mechanisms. (a) On the one hand, the particle itself can rotate in liquid. This is referred to as Brown relaxation. (b) On the other hand, the magnetic moment orientation rotates inside the particle without a change of the orientation of the particle itself. In both figures, the particle orientation is marked by a blue line, and the magnetic moment orientation vector is represented by a red arrow.

The second relaxation mechanism, the Néel rotation, describes the rotation of the magnetic moment vector inside the particle without a rotation of the particle itself which is shown in figure 6.2(b). In the case of a single-domain particle with uniaxial anisotropy in zero external magnetic field, for a change in the magnetic moment orientation, an energy barrier KV_p has to be overcome. Here, K denotes the particle material's anisotropy constant and V_p denotes the particle volume. For $k_BT \gg KV_p$, the thermal energy is large enough to induce fluctuations of the magnetic moment orientation. The characteristic time associated with this mechanism, τ_N, reads as follows.

$$\tau_N = \frac{1}{f_0} exp\left(\frac{KV_p}{k_BT}\right) \tag{6.3}$$

In this equation, f_0 denotes a characteristic frequency that can be determined experimentally [140, 141]. For small particle diameters, the Néel relaxation dominates whereas for larger particle diameters the Brown relaxation dominates. According to [142], both mechanisms can be combined to the so-called effective relaxation time τ_{eff} which provides information about the actual relaxation behavior to a given particle diameter.

$$\tau_{eff} = \frac{\tau_B \cdot \tau_N}{\tau_B + \tau_N} \tag{6.4}$$

The effective relaxation time τ_{eff} must be compared to the mechanical relaxation time in order to determine the degree of separation of the two classes of degrees of freedom in order to establish a quasi-simultaneous hybrid approach.

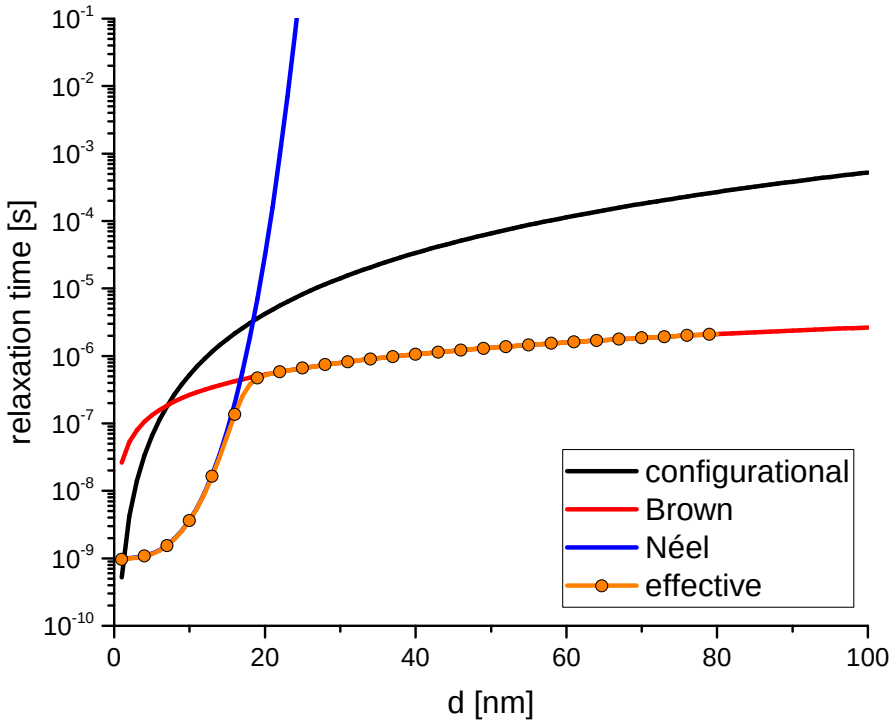

FIGURE 6.3: Comparison of the relaxation times of the mechanical and the magnetic degrees of freedom of cobalt nanoparticles with diameters up to 100 nm immersed in 2% agarose with $\eta_m = 0.017\ Pa \cdot s$. The mechanical relaxation is dominated by the configurational relaxation time (see equation 6.1) whereas the magnetic relaxation occurs on the time scales that are given by the Brown and the Néel relaxation times as shown in equations 6.2 and 6.3. For small particle diameters the Néel relaxation time dominates whereas for larger diameters of the particles the Brown relaxation time dominates. This is represented by the effective relaxation time which combines the Néel and the Brown relaxation times according to equation 6.4. This figure is reproduced from [134].

6.2.3 Comparison of mechanical and magnetic relaxation times

In order to validate the assumption that the time scales of the mechanical and the magnetic relaxation are clearly separated for systems of magnetic nanoparticles that are immersed in gel matrices, the specific time scales for realistic parameters are estimated. In close coordination with previous experimental investigations [5, 6, 111] cobalt nanoparticles with diameters of up to 100 nm are considered. Therefore, the anisotropy constant is set to $K = 10^5 \frac{J}{m^3}$. In addition to that the characteristic frequency of the Néel rotation is assumed to be $f_0 = 10^9 Hz$. In order to consider a realistic matrix material, the kinematic viscosity of the liquid medium is set to $\eta_m = 0.017\ Pa \cdot s$ to mimic a 2% Agarose matrix as proposed in [5, 6, 111].

The result of the evaluation of the relevant time scales is shown in figure 6.3. It becomes apparent that both the configurational (mechanical) relaxation time and Brown (magnetic) relaxation time slowly increase with an increasing particle diameter. At the

same time, these relaxation times are clearly separated. In contrast to that, the Néel relaxation time increases very rapidly with an increasing particle diameter. As already stated above, the Néel relaxation dominates for small particle diameters whereas for larger diameters of the particles the Brown relaxation dominates. Here, a transition between these two mechanisms can be identified for values of the particle diameter of about 20 nm. The actual relaxation time is described by the effective relaxation time that considers both of the magnetic relaxation algorithms. In figure 6.3, it becomes clear that for particle diameters below the transition at about 20 nm, the Néel relaxation is crucial. For the separation of the magnetic and mechanical degrees of freedom this means that the configurational relaxation time has to be compared to the Néel relaxation time. Here, it can be noted that except for very small particle diameters of up to about 3 nm the magnetic and mechanical relaxation times are separated by at least one order of magnitude. At the transition point at $d = 20$ nm, the separation is slightly reduced but still clearly present at about one order of magnitude. Above the transition point, the magnetic relaxation is dominated by the Brown relaxation time. Here, in contrast to the regime below the transition point, the difference between the magnetic and the mechanical relaxation time increases continuously with increasing the particle diameter. Hence, a clear separation of the different types of degrees of freedom is ensured for all diameters except for very small diameters.
This comparison can be repeated for different values of the parameters viscosity and anisotropy constant. Even for large viscosities and significantly increased values of the anisotropy constant, a clear separation between the mechanical and magnetic degrees of freedom can be observed for reasonable particle diameters. Obviously, the critical points shift along the particle size axis but, nevertheless, qualitatively the same features can be observed.
In summary, a clear separation of the configurational (mechanical) relaxation and the effective (magnetic) relaxation time which represents the Brown and the Néel relaxation can be observed for realistic values of the crucial parameters. Thus, a hybrid approach can be followed for the quasi-simultaneous simulation of the magnetic and the mechanical degrees of freedom of magnetic particles in viscous matrices which takes advantage of this very separation.

6.3 The role of temperature

As introduced in chapter 3, spin dynamics and molecular dynamics simulations are usually performed in the canonical ensemble which represents most of the experimental situations. Hence, the average temperature is kept constant during the simulation. This

is realized by means of an infinitely large heat bath that is coupled to the simulated system. Here, a Langevin approach is used to couple the system to a heat bath by means of stochastic forces in the framework of spin dynamics. For the molecular dynamics part of the hybrid algorithm, a Nosé-Hoover thermostat is used. In order to avoid conflicts between these two different heat baths in the hybrid framework, the temperature of the spin dynamics heat bath is set to $T = 0\ K$. At the same time, the molecular dynamics simulations are carried out at room temperature. It is explained in [143] that it is common practice to couple separate thermostats to the subsystems of a simulated system. This applies to systems with sets of degrees of freedom that differ significantly concerning their characteristic frequencies. If one would couple such a system to one heat bath the exchange of energy between the subsystems would be too slow. Thus, the sets of degrees of freedom would obtain different effective temperatures. This is referred to as "Hot-Solvent/Cold-Solute Problem" in the literature [143]. A typical example for a system with strongly deviating characteristic frequencies is a system that contains macromolecules in solution where a single thermostat would cause the average solute temperature to be significantly lower than the average solvent temperature. This problem is usually solved by applying two seperate thermostats to the two subsets of degrees of freedom. This separation is based on *ab initio* molecular dynamics methods such as the Car-Parrinello approach [144] where the nuclear and electronic subsystems are separated dynamically. According to Car and Parrinello, the slow nuclei are connected to a "physical" temperature whereas the fast electronic degrees of freedom are linked to a "fictitious" temperature. It is stated in [145] that the electronic subsystem which is assumed to be cold is close to its minimum energy constellation. For the hybrid algorithm, in analogy to [145], here, it is assumed that the cold and fast magnetic degrees of freedom are close to their minimum energy configuration. This can be verified by pure spin dynamics simulations. As a consequence of that the heat bath temperature of the spin dynamics algorithm is set to $T = 0\ K$. At the same time, the actual environment temperature is considered in the molecular dynamics algorithm. In this work, simulations are performed at room temperature.
However, as introduced in chapter 5, a finite temperature bath can be applied for the spin dynamics steps of the hybrid algorithm in order to efficiently find low energy configurations. Therefore, the system can be cooled from a high initial temperature to $0\ K$ during the simulation in order to avoid freezing in local energy minima.

6.4 Hybrid simulation coupling procedure

For the hybrid simulation method, the molecular and spin dynamics algorithms that are introduced in chapter 3 are combined into one new algorithm for the quasi-simultaneous

simulation of the magnetic and mechanical evolution of magnetic nanoparticles in viscous matrices. As it is shown in figure 6.4 for a number of i magnetic particles, the simulation starts from a random configuration $\{\mathbf{S}_i\}_0$ of the magnetic moments to given positions $\{\mathbf{r}_i\}_0$. The effective magnetic moment of each homogeneously magnetized particle (see chapter 2.1) is calculated from the particle's diameter d_p and the material's saturation magnetization M_{sat} as introduced in chapter 3.1.1, equation 3.1 [72]. First, the initial configuration $\{\mathbf{S}_i\}_0$ $\{\mathbf{r}_i\}_0$ is used as input for the classical spin dynamics algorithm (see chapter 3.1). Here, the first magnetic low energy configuration $\{\mathbf{S}_i\}_1$ is calculated, i.e. the magnetic moment configuration is relaxed towards the first low energy state. The term low energy configuration is chosen because the particle configurations are spatially disordered which leads to geometric frustration. As a consequence of that, the particles behave like a magnetic dipole spin glass as it is introduced in chapter 2.1.2. For the duration of the spin dynamics program run, the positions of the particles are fixed whereas the magnetic moment orientations change to a configuration with a local minimum in the total magnetic dipole energy. This is realized by the Runge-Kutta integration of the damped Landau-Lifshitz equation with a Langevin-like coupling to a heat bath. In order to avoid conflicts with the heat bath of the molecular dynamics algorithm, the temperature of the spin dynamics heat bath is set to 0 K as introduced in chapter 6.3. After the full initial spin dynamics run, the updated magnetic moment orientations $\{\mathbf{S}_i\}_1$ are forwarded to the molecular dynamics algorithm together with the initial particle positions $\{\mathbf{r}_i\}_0$. Within the molecular dynamics algorithm, the forces on all particles are calculated first. These forces include the magnetic dipole-dipole forces, the Weeks-Chandler-Anderson force contributions to enable hard particle dynamics, and the viscous forces due to Stokes drag, see chapter 3.2.2. The force contributions are then summed up for every particle in the system. With these forces, the equations of motion are integrated in the picture of the canonical ensemble with a given temperature by means of the Velocity Verlet algorithm and the Nosé-Hoover thermostat which are introduced in chapters 3.2.4 and 3.2.5. The integration is performed for a very small step in time. Subsequently, the forces on all particles are calculated again for the new positions and the integration of the equations of motion is performed again. This force calculation and integration is repeated for a predefined number of steps in time. Meanwhile, the orientations of the magnetic moments are not updated again. This procedure is based on the assumption that the mechanical and the magnetic degrees of freedom can be treated separately as introduced in chapter 6.2.3. After the predefined number of molecular dynamics time steps is reached the resulting configuration involves the updated positions $\{\mathbf{r}_i\}_1$ together with the previous orientations $\{\mathbf{S}_i\}_1$. Then, the next full spin dynamics run is intercalated which uses the positions that result from the preceding molecular dynamics steps $\{\mathbf{r}_i\}_1$. As a consequence, the magnetic moments obtain new orientations $\{\mathbf{S}_i\}_2$ that are again passed over to the molecular dynamics algorithm.

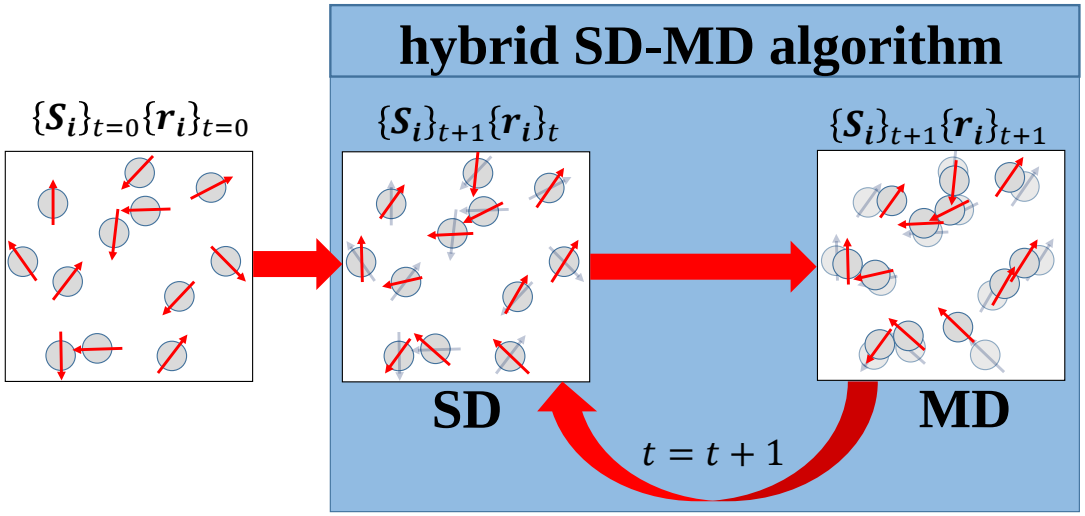

FIGURE 6.4: Schematic representation of the hybrid algorithm that couples classical spin dynamics and classical molecular dynamics simulations in order to compute the trajectories of magnetic nanoparticles in viscous matrices. The particles interact with each other magnetically and mechanically with the viscous matrix material. Starting from a random initial configuration, the first magnetic low energy state is calculated by the spin dynamics algorithm. The orientations of the magnetic moments are updated whereas the particle positions are fixed for this step. The new orientations and the old positions are passed over to the molecular dynamics algorithm. Here, the forces on all particles and the resulting motion for a small step in time are calculated. Subsequently, the new positions and the old moment orientations are again communicated to the spin dynamics algorithm to calculate the next magnetic low energy state. These steps are repeated until a predefined number of time steps is reached.

These steps (orientation update by spin dynamics and position update by molecular dynamics) are repeated until a predefined number of total steps in time is reached.

6.5 Validation: Hybrid simulation of a particle ring

In order to validate the hybrid molecular and spin dynamics coupling algorithm that is presented in the previous sections, a simple example is treated analytically and by means of pure spin dynamics calculations because the magnetic microstructure cannot be investigated experimentally in detail for a comparison. Here, an ideal ring-shaped ensemble of cobalt particles with equal diameters of 100 nm is investigated. The virtual ring the particles are placed on measures 500 nm in diameter. The magnetic ground state of a ring-shaped ensemble of magnetic moments is well-known and documented [146, 147]. As it is shown in figure 6.5, the magnetic moments form a so-called flux closure state where the magnetic moments form a circle with a clockwise or counterclockwise orientation. These experimental observations can be reproduced by pure spin dynamics

TABLE 6.1: Initial positions (x-coordinate and y-coordinate) and the resulting magnetic moment orientations m_x, m_y of the 12 magnetic particles in a ring-shaped configuration. The magnetic moment orientations have been calculated by means of spin dynamics simulations. The simulated magnetic moment orientations are in agreement with experimental findings according to [146, 147]

particle	x-coordinate in nm	y-coordinate in nm	m_x in Am^2	m_y in Am^2
P1	0	250.000	$-7.435 \cdot 10^{-16}$	0
P2	125.000	216.506	$-6.439 \cdot 10^{-16}$	$3.717 \cdot 10^{-16}$
P3	216.506	125.000	$-3.717 \cdot 10^{-16}$	$6.439 \cdot 10^{-16}$
P4	250.000	0	0	$7.435 \cdot 10^{-16}$
P5	216.506	−125.000	$3.717 \cdot 10^{-16}$	$6.439 \cdot 10^{-16}$
P6	125.000	−216.506	$6.439 \cdot 10^{-16}$	$3.717 \cdot 10^{-16}$
P7	0	−250.000	$7.435 \cdot 10^{-16}$	0
P8	−125.000	−216.506	$6.439 \cdot 10^{-16}$	$-3.717 \cdot 10^{-16}$
P9	−216.506	−125.000	$3.717 \cdot 10^{-16}$	$-6.439 \cdot 10^{-16}$
P10	−250.000	0	0	$-7.435 \cdot 10^{-16}$
P11	−216.506	125.000	$-3.717 \cdot 10^{-16}$	$-6.439 \cdot 10^{-16}$
P12	−125.000	216.506	$-6.439 \cdot 10^{-16}$	$-3.717 \cdot 10^{-16}$

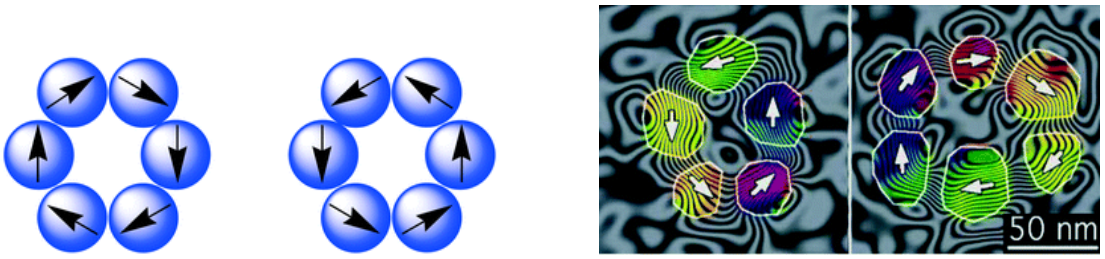

(a) (b)

FIGURE 6.5: Flux closure state of magnetic nanoparticle rings. (a) Illustration of flux closure domains in cyclic ensembles of magnetic dipoles in clockwise (left) and counterclockwise (right) configurations. (b) Off-axis electron holography images of self-assembled Co nanoparticle rings, taken at 298 K using a Philips CM-300 equipped with a Lorentz lens (300 keV). The polarization of the FC states are depicted using arrows and colors (red = right, yellow = down, green = left, blue = up). The magnetic flux enclosed between adjacent contours is $h/128e$, and correlates with the contour linewidths. The figures are reproduced with permission from [147].

simulations. Starting from a random configuration of the magnetic moments at the given positions, the magnetic ground state is calculated by the spin dynamics method that is presented in chapter 3.1 at $T = 0\ K$. The initial configuration and the resulting flux closure configuration that is obtained after 97 time steps with a step length of $dt = 1 \cdot 10^{-14}\ s$ are shown in figure 6.6 whereas the actual positions and magnetic moment orientations are collected in table 6.1.

In order to validate the hybrid molecular and spin dynamics simulation method, the orientations of the magnetic moments that result from the pure spin dynamics simulation are then used to calculate the forces on the particles by hand. Because the ring-shaped

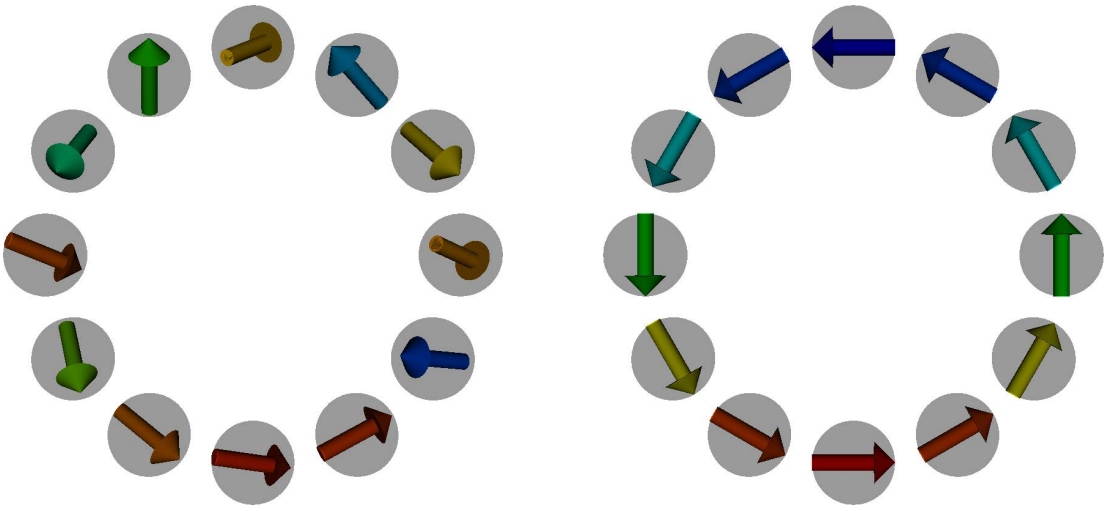

(a) (b)

FIGURE 6.6: Spin dynamics simulations of a ring-shaped configuration of 12 cobalt particles with diameters of 100 nm. The magnetic macro moments of the particles are initialized with random orientations (a). After 97 steps in time with a step size of $1 \cdot 10^{-14}$ s, the ring-shaped flux closure state of the magnetic moments is reached.

TABLE 6.2: Force contributions on the topmost particle (particle 1) due to the magnetic dipole-dipole interaction. These forces are calculated according to equation 2.9 for the positions and magnetic moment orientations that are given in table 6.1.

force contribution	F_x in N	F_y in N
$F_{1,1}$	0	0
$F_{1,2}$	$1.181 \cdot 10^{-16}$	$-3.165 \cdot 10^{-17}$
$F_{1,3}$	$4.596 \cdot 10^{-18}$	$-2.654 \cdot 10^{-18}$
$F_{1,4}$	$-2.654 \cdot 10^{-18}$	$2.654 \cdot 10^{-18}$
$F_{1,5}$	$-2.553 \cdot 10^{-18}$	$4.423 \cdot 10^{-18}$
$F_{1,6}$	$-1.371 \cdot 10^{-18}$	$5.117 \cdot 10^{-18}$
$F_{1,7}$	0	$5.307 \cdot 10^{-18}$
$F_{1,8}$	$1.371 \cdot 10^{-18}$	$5.117 \cdot 10^{-18}$
$F_{1,9}$	$2.553 \cdot 10^{-18}$	$4.423 \cdot 10^{-18}$
$F_{1,10}$	$2.654 \cdot 10^{-18}$	$2.654 \cdot 10^{-18}$
$F_{1,11}$	$-4.596 \cdot 10^{-18}$	$-2.654\dot{1}0^{-18}$
$F_{1,12}$	$-1.181 \cdot 10^{-16}$	$-3.165 \cdot 10^{-17}$

particle ensemble is highly symmetrical, the complete system can be described with the forces on one of the particles. Here, the magnetic dipole-dipole force contributions on the topmost particle (P1 in figure 6.7) are calculated according to equation 2.9 in chapter 2.1.1. The resulting forces are shown in table 6.2.

Due to the characteristics of the magnetic dipole-dipole interaction, the force contributions that are caused by the nearest neighboring particles P2 and P12 dominate whereas the other contributions are small. The force contributions are depicted in figure 6.7. While the x-components of the force contributions cancel out, the dominating

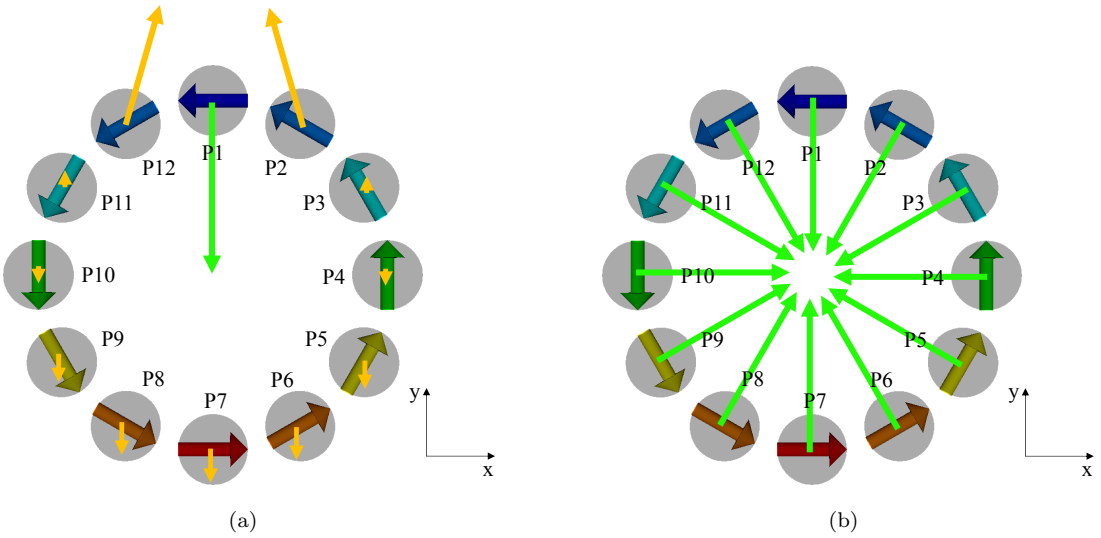

FIGURE 6.7: Magnetic dipole-dipole force contributions on particle 1 (P1). (a) The forces are calculated from the magnetic moment orientations that result from a spin dynamics simulation. For the sake of clarity, the counterforces, i.e. the force contributions that P1 imposes on all the other particles, are depicted here (yellow). The resulting force on P1 is shown in green. The length of the force contribution arrow qualitatively represents the value of the force. It becomes apparent that the contributions due to particles 2 and 12 dominate. Moreover, the x-components of the force contributions cancel out. Hence, P1 is pulled towards the center of the ring structure. (b) Due to the symmetry of the structure, the resulting forces on the other particles have the same absolute value as the force on P1. The forces are rotated around the center of the ring so that each force points from the center of the particle to the center of the ring.

y-components due to P2 and P12 result in a force on P1 that acts towards the center of the particle ring. Therefore, P1 is pulled towards the center of the ring structure. Due to the symmetry of the ring configuration, the resulting forces on the other particles can be determined by a simple rotation around the center of the ring. Hence, similar to P1, the resulting forces on all the other particles in the configuration due to the magnetic interactions between the particles act along the lines that connect the centers of the particles and the center of the ring as shown in figure 6.7(b).

In summary, the particles in the ring-shaped configuration are pulled towards the center of the ring due to the magnetic dipole-dipole interactions between the particles. While the particles move towards the center, the magnetic moment orientations do not change because the symmetry of the configuration is preserved. It is obvious that the final configuration is again ring-shaped but the diameter is smaller than for the initial configuration so that the particles are in contact. For 12 particles with diameters of 100 nm, the ring would measure 381.97 nm in diameter. Hard particle dynamics is realized by the WCA potential that is introduced in chapter 3.2.2. When the particles get in contact and overlap, a large force in opposition to the actual particle movement is exerted on the particles. This force immediately drops to zero when the particles are in contact

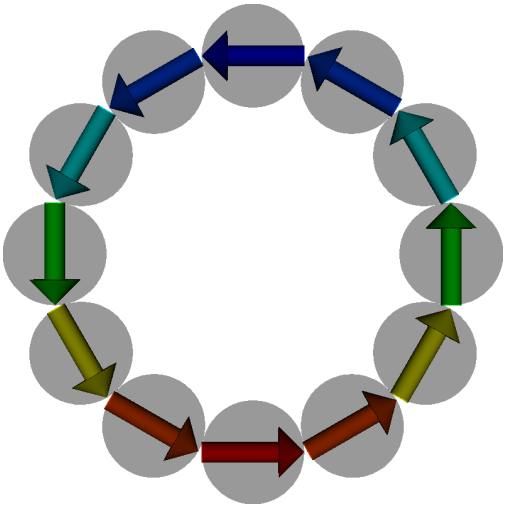

FIGURE 6.8: Final configuration of 12 cobalt particles in a ring-shaped configuration. In agreement with preliminary theoretical considerations, the particles form a stable ring with the particles in contact to each other.

without any overlap. Here, for the final, ring-shaped configuration of the particles, the WCA force contributions ensures that the particles do not overlap. Thus, the particles should form a stable ring with a diameter of about 382 nm.

For the validation of the hybrid molecular and spin dynamics algorithm, the ring-shaped configuration of 12 particles is investigated numerically in order to compare the numerical results to the theoretical expectations. The result of the hybrid simulation of the ring-shaped particle configuration is shown in figure 6.8. It becomes apparent that the numerical result meets the theoretical expectations. The result can be reproduced with other random initial configurations of the magnetic moments of the particles.

6.6 Hybrid molecular and spin dynamics summary

In conclusion, a novel, hybrid simulation method is presented that couples spin dynamics methods for the magnetic degrees of freedom and molecular dynamics methods for the mechanical degrees of freedom of ensembles of magnetic particles in viscous matrices. The coupling of these methods is realized in a consecutive approach which is based on the clear separation of the time scales of the different types of degrees of freedom. The hybrid method is validated with a ring-shaped configuration of 12 particles.

7

Hybrid simulation of the model structure AH41 and estimation of its GMR properties

In order to demonstrate the capabilities of the hybrid molecular and spin dynamics coupling procedure that is presented in chapter 6, a simulation run of the model structure AH41 which is introduced in chapter 4.3 is presented here. As it is shown in chapter 6, the main objective of this work is to predict qualitative GMR properties of nanoparticle ensembles in viscous matrices. According to chapter 2.2.3, the GMR curve of a nanoparticle configuration can be calculated from magnetization curves which can easily be generated by spin dynamics simulations. In the following sections, first, the hybrid molecular and spin dynamics simulation of the model structure AH41 is presented. After that, the subsequent calculation of a qualitative GMR curve is demonstrated. The results that are shown here have been published in [112].

7.1 Hybrid simulation of AH41

In order to perform hybrid molecular and spin dynamics simulations of the model structure AH41, 8 significantly overlapping particles had to be removed from the system in order to enable numerical stability for a reasonable time step size. The initial configuration of the 192 monodisperse cobalt nanoparticles with diameters of 20 nm that are distributed over 350 $nm \times 350$ nm is shown in figure 7.1. The particles are shown true to scale in translucent gray. Each magnetic particle carries an effective magnetic moment that is represented by an arrow. The color of each arrow pictures the x-component of the particle's effective magnetic moment vector to ensure a good overview. For this exemplary simulation, the viscosity of the matrix material is set to 0 $Pa \cdot s$. As introduced in chapter 6.3, the spin dynamics temperature is set to 0 K for the hybrid simulation

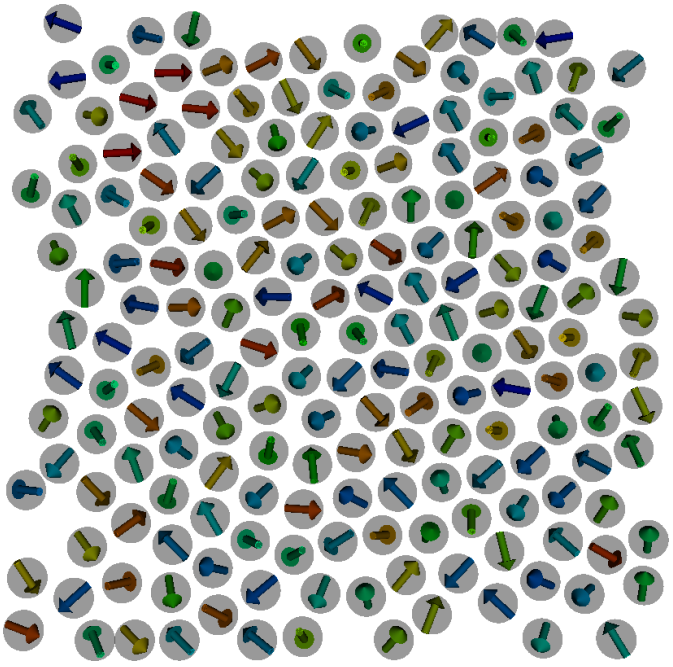

FIGURE 7.1: Initial particle positions and random magnetic moment orientations for the hybrid simulation of the model structure AH41 with 192 cobalt particles with equal diameters of 20 nm. This figure is taken from [112].

whereas the actual temperature is considered in the heat bath coupling of the molecular dynamics algorithm. Here, the model structure AH41 is simulated at room temperature.

At first, the magnetic low energy configuration of this system is calculated by means of a complete spin dynamics run. Here, for AH41, 10^4 steps with a time step length of $10^{-14}s$ are performed to reach a magnetic moment configuration that does not change with time any longer. This magnetic moment configuration $\{\mathbf{S}_i\}_1$ is then used together with the initial positions $\{\mathbf{r}_i\}_0$ to compute the forces on all the particles. In general, these forces are due to magnetic dipole-dipole interactions and hard sphere interactions between the particles and interactions with the particles and the viscosity of the liquid matrix as introduced in chapter 3.2.2. For this example, the viscous forces all equal zero because the viscosity is set to zero as introduced above. The force contributions are then summed up for every particle. With these total forces per particle, the Newtonian equations of motion are solved for one step in time according to the Velocity Verlet algorithm, see equation 3.25. Here, the time step length is $10^{-14}\tau$. In contrast to the time step length of the spin dynamics algorithm that is given in seconds, the time step length of the molecular dynamics part of the algorithm is given in the reduced Lennard-Jones unit τ as it is presented in chapter 3.2.7. In addition to that, it has to be noted that the actual time step length of the molecular dynamics algorithm must be regarded as relative due to the characteristics of the Nosé-Hoover thermostat, see chapter 3.2.5. Here, the effective relaxation time τ_{NH} is set to 1. The effective relaxation time is related

to the *virtual mass* Q of the Nosé-Hoover thermostat via the following equation.

$$\tau_{NH} = \sqrt{\frac{Q}{gk_BT}} \tag{7.1}$$

In equation 7.1, g represents the number of degrees of freedom. Hence, the molecular dynamics time is effectively scaled by the virtual mass Q and cannot be compared to the "real" time steps of the spin dynamics algorithm. As introduced in chapter 6.2, the mechanical degrees of freedom can be considered to be much slower than the magnetic degrees of freedom. Thus, a large number of molecular dynamics time steps has to be performed, before any magnetic rearrangement should reasonably be expected. In the case of AH41, 10^4 molecular dynamics steps (force calculation and integration of the Newtonian equations of motion) are performed without recalculation of the magnetic moment orientations. After these 10^4 steps in time, the current configuration consists of the particle positions $\{\mathbf{r}_i\}_1$ and the previously calculated magnetic moment orientations $\{\mathbf{S}_i\}_1$. As a next step, another full spin dynamics run consisting of 10^4 steps is performed which leads to the new magnetic moment orientations $\{\mathbf{S}_i\}_2$. Again, these orientations are used for 10^4 molecular dynamics time steps. These steps are repeated until the total number of $2 \cdot 10^7$ molecular dynamics time steps is reached. Hence, 2000 spin dynamics runs are performed over the course of $2 \cdot 10^7$ molecular dynamics time steps. Due to the diminishing disorder of the structure over the simulation run, the variations of the magnetic and topological structures are significant in the beginning of the simulation and become smaller over time. Snapshots of the time evolution of the model structure AH41 are shown in figure 7.2.

As reported in [112], the total magnetic dipole-dipole energy and the magnetization are gradually reduced over the simulation run until a minimum value of both is reached. For the initial configuration, a total magnetic energy of $E_{init} = -3.34852 \cdot 10^{-15}$ J arises. For the final configuration, the total magnetic energy is reduced to $E_{final} = -1.65116 \cdot 10^{-13}$ J. The minimum energy configuration consists of chain fragments that are ferro- or antiferromagnetically coupled and particle rings or islands that contain magnetic vortices. This is in agreement with the experimental observations that are published in [112]. In [112], the detailed microstructure of exemplary particle systems is revealed by a three-dimensional reconstruction technique as presented in chapter 4. Pure spin dynamics simulations of the reconstructed systems reveal chains and vortices in broad agreement with the hybrid simulations that are presented here. A detailed discussion of the experimental part of the investigations will be published in [111].

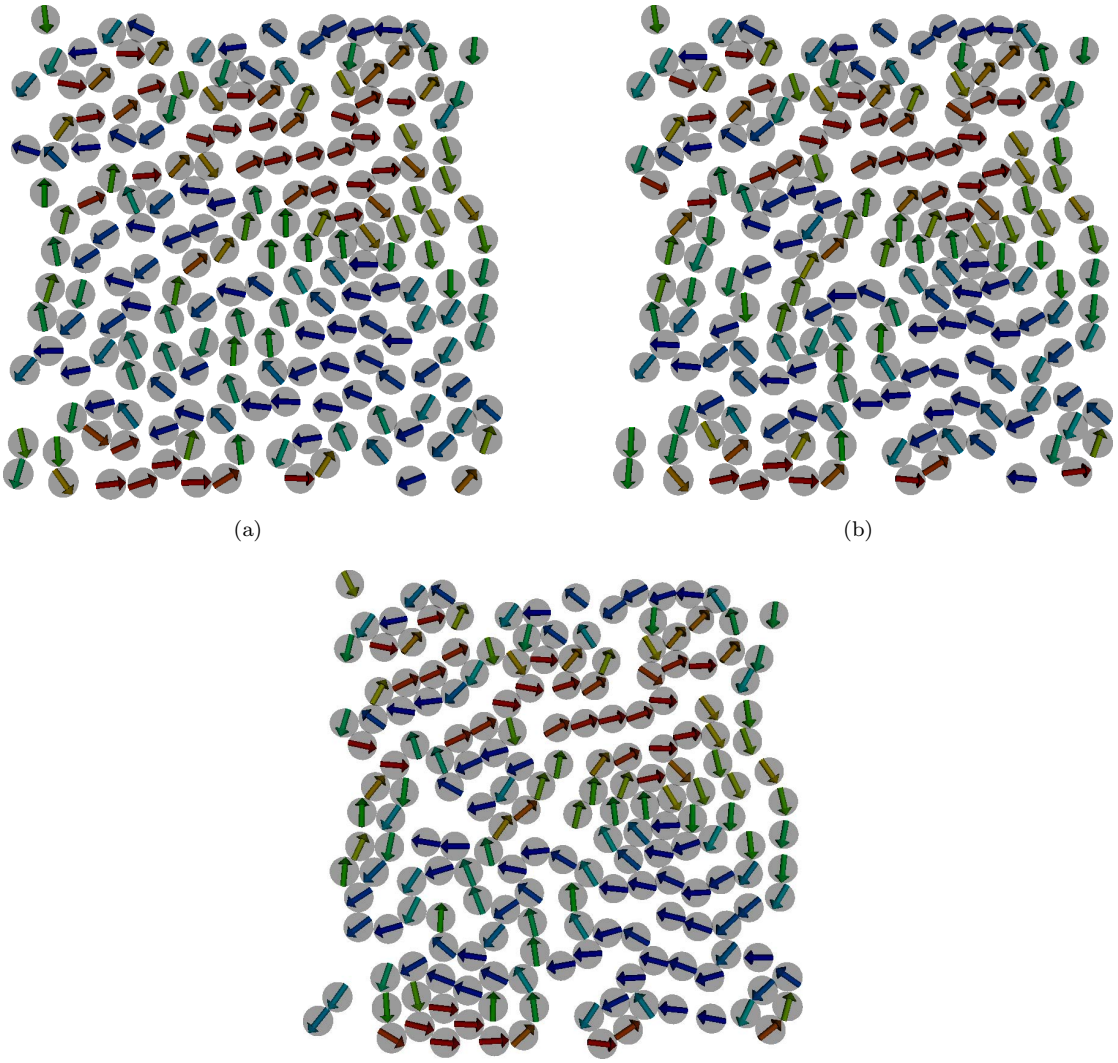

(a) (b) (c)

FIGURE 7.2: Snapshots of the topological and magnetic configurations of the model structure AH41 that is calculated by the hybrid molecular and spin dynamics simulation method. Here, $2 \cdot 10^7$ steps in time with a step length of $1 \cdot 10^{-14}$ in reduced Lennard-Jones units are performed with one full spin dynamics run after every 10000 steps in time. (a) Snapshot after $1 \cdot 10^6$ time steps, (b) snapshot after $2 \cdot 10^6$ time steps and (c) final configuration after $2 \cdot 10^7$ time steps. Figure (c) is taken from [112].

7.2 Prediction of qualitative GMR properties

For granular systems, the experimental GMR curves are measured by tracking the system's electrical resistance in a time-dependent external magnetic field as introduced in chapter 2.2.3. In zero external field, the magnetic configuration is disordered, i.e. the magnetic moment orientations are statistically distributed. Thus, the electrical resistance obtains the maximum value because the electrons are scattered spin-dependently. For increasing values of the external magnetic field the magnetic moments are increasingly oriented along the magnetic field direction. Thereby, the spin-dependent scattering

of the electrons is reduced resulting in a decrease of the electrical resistance with further increasing external magnetic field. On the part of theory, according to [50], the GMR ratio can be calculated from magnetization curves according to the following equation (duplication of equation 2.13) as introduced in chapter 2.2.3 on the basis of the magnetic order.

$$\mathrm{GMR} = A_{\mathrm{GMR}} \left[1 - \left(\frac{M}{M_S} \right)^2 \right] \tag{7.2}$$

This equation can be applied to experimentally obtained magnetization curves as well as to simulated magnetization curves. Experimentally, the GMR properties of the particle-gel system in the solid state of the gel matrix are essential. For the simulation, this state can be represented by freezing the mechanical degrees of freedom which effectively corresponds to switching off the molecular dynamics part of the algorithm.
Subsequent to the full hybrid simulation that is presented in chapter 7.1, the final particle positions are written to a new structure file that can be used as an input for a pure spin dynamics simulation. This corresponds to the solid state of the gel that can be investigated by switching off the molecular dynamics part of the hybrid algorithm. For the spin dynamics simulation of AH41, 10^5 steps in time with a step length of 10^{-13} s are performed. In order to investigate the magnetization dynamics, the external in-plane magnetic field is ramped up from -0.2 T to 0.2 T and back down to -0.2 T during the simulation, in analogy to experimental investigations of similar structures. The simulated magnetization curve and the resulting GMR curve are shown in figure 7.3.

Figure 7.4 shows the experimental situation. Here, the same system that is used as a guideline for the determination of the model structure AH41 as shown in chapter 4.3 is investigated experimentally concerning its GMR properties. Therefore, a four point probe setup is used to determine the electrical resistance as a function of the external magnetic field according to chapter 2.2.3 at room temperature. The experimentally obtained GMR curves are shown in figure 7.4(b) as a function of the particle concentration. In the GMR curves, the maximum values of the electrical resistance correspond to the structure with a maximum disorder, i.e. the magnetic moment orientations are statistically distributed in the absence of an external magnetic field. By increasing the absolute value of the external magnetic field the magnetic moment orientations are gradually oriented and therefore, the GMR value drops to a minimum value that corresponds to a magnetic configuration with the maximum order.

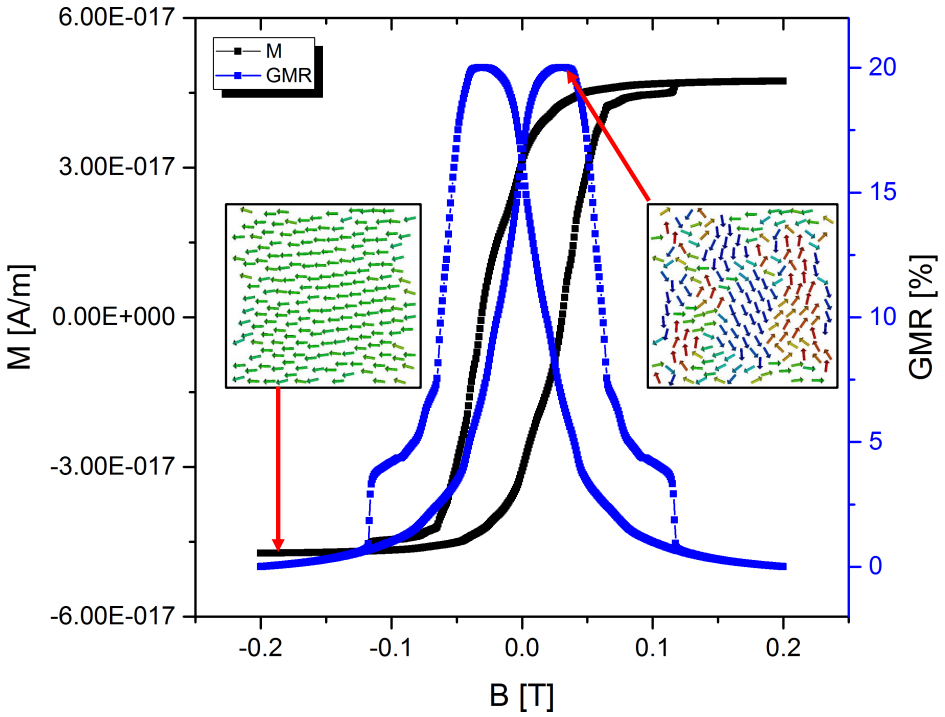

FIGURE 7.3: Calculated GMR curve (blue) for the simulated magnetization curve (black) of the final configuration of the hybrid molecular and spin dynamics simulation of the model structure AH41. The GMR curve is calculated from the magnetization data by equation 7.2. As stated in chapter 2.2.3, the GMR effect amplitude must be determined experimentally. Here, an effect amplitude of 20 % is assumed following the experimental investigations on similar structures as presented in [112]. This figure is reproduced from [112].

Finally, the theoretical results can be compared to the experimental results. It becomes apparent that the theoretically obtained GMR curves in figure 7.3 show a strong similarity with the experimentally obtained curve that is shown in figure 7.4(b). Provided that the simulated model system AH41 is greatly simplified compared to the real system, it is worth noting that the main features of the experimental GMR curve are reproduced in the simulation very well. There is a great correspondence between the curve shapes of the experimental and theoretical investigations. One crucial feature is the external field value of the least ordered magnetic configuration. On the theoretical side, this point can be found at about $0.04\ T$ and $-0.04\ T$ respectively. In the experimentally obtained GMR curve, the same point can be found at about $400\ Oe$ and $-400\ Oe$. Under the assumption of a relatively small particle fraction of the system, the overall relative permeability can be assumed to be close to 1. Thus, a magnetic field strength of 1 Oersted corresponds to a magnetic flux density of 1 Gauss. As 1 Gauss is equivalent to 10^{-4} Tesla in SI units, 1 Oersted is likewise equivalent to a magnetic flux density of 10^{-4} T. Hence, the experimentally determined magnetic field for the least magnetic order at ± 400 Oersted corresponds to a magnetic flux density of ± 0.04 T.

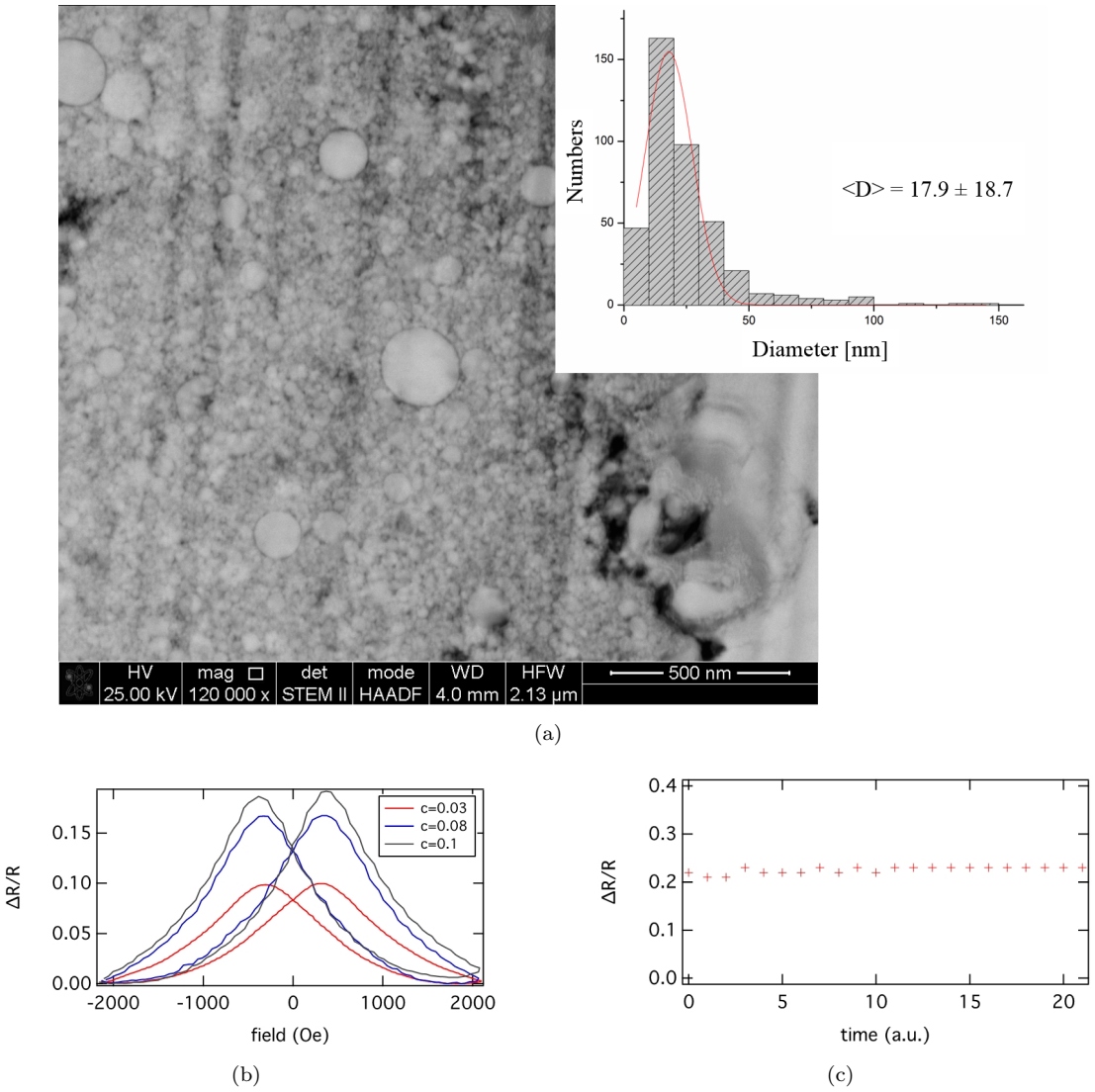

FIGURE 7.4: GMR measurement on cobalt particles embedded in agarose. (a) STEM image and particle size distribution of Co core / conductive C-shell nanoparticles that are used for AC GMR measurements; (b) Experimentally determined GMR curves as a function of the particle mass concentration. The GMR effect amplitude is given as $\frac{\Delta R}{R}$ with R the electrical resistance. This corresponds to an effect amplitude of about 10 to 20 %. The reliability of the measurement can be evaluated by means of repeated measurements as shown in (c). This figure is reproduced from [112].

In summary, a first, rough estimation of the magnetoresistive properties is possible by means of numerical simulations. Here, it is shown that there is substantial consensus between previous experimental results and the theoretically obtained GMR curves that are calculated from simulated magnetization curves. It has to be noted that due to the simplifications that are made for the particle configuration and the simplifying assumptions that are used for the calculation of the GMR from the magnetization without any consideration of electron transport through the system, the calculated GMR curves can only give a very basic indication of the GMR properties. [112]

7.3 Hybrid simulation and evaluation of GMR curve of AH41 summary

To sum up, the hybrid molecular and spin dynamics algorithm (see chapter 6) has been applied to the model structure AH41 that has been constructed to mimic real systems by abstraction and downsizing as presented in 4.3. In doing so, the particle trajectories have been calculated from a given initial to the final configuration. For the computation of the particle trajectories, the magnetic dipole-dipole interactions of the particles, hard particle interactions and interactions with the surrounding medium have been taken into account. With this method the self-assembly process of the magnetic particles in the liquid matrix can be investigated and visualized step by step. Depending on the particular simulation parameters, the magnetic moment orientations and particle positions can be observed for virtually any step in time. Thus, a crucial gap is closed because the experimental observation of the dynamical evolution of magnetic moments of single particles is yet not possible at this time. With the final evaluation of the magnetoresistive properties by means of an additional spin dynamics simulation, general features can be identified that lead to particularly good magnetoresistive properties.
With the example that is presented here it becomes clear that with the simulation tool chain that is presented in this thesis a route is opened up that shows clear similarities to the experimental experimental approach. The first step, of the experimental as well as the theoretical approach, is the preparation of the system. On the experimental side, the particles are mixed into the gel and the self-assembly process takes place. For the theoretical approach, the corresponding particle trajectories are calculated by means of the hybrid molecular and spin dynamics algorithm. After the self-assembly is finished, the gel matrix is dried out in the experiment whereas the molecular dynamics part of the theoretical method is switched off to mimic the particles that are embedded in the now rigid matrix material. After the system is prepared, experimentally or theoretically, the actual measurement is performed. Here, the crucial quantity of interest is the GMR ratio because in magnetoresistive sensor applications, the sensor sensitivity is dominated by the GMR characteristics. Experimentally, the GMR curve is determined in a four point probe setup by measuring the resulting voltage to a given current. On the theoretical side, the GMR curve is determined from a subsequently calculated magnetization curve. Here, it is shown with the example of the simplified model structure AH41 that *in silico* experiments can be used to complement and replace experiments on real systems. In doing so, a cheap and fast way to investigate combinations of particle materials, size distributions, concentrations, and matrix materials is created.

8

Suggestions for further experimental investigations

In chapter 7 it is shown that the hybrid molecular and spin dynamics algorithm can be used to compute the trajectories of self-assembling magnetic particles in viscous matrices due to magnetic dipole-dipole, viscous and hard sphere interactions. From the resulting topological and magnetic configurations, magnetization curves can be computed to determine first estimations of the GMR curves. Moreover, the hybrid algorithm can be applied to three-dimensional configurations and interesting effects can be revealed. As a consequence, one is able to predict highly promising structures for further experimental investigations. In addition to that, arbitrary three-dimensional nanoparticle arrangements can be investigated by the hybrid simulation method. In doing so, one is able to predict interesting experimental situations. In this chapter, different suggestions for further experimental and combined theoretical/experimental studies are made. All ideas that are presented here must be interpreted as first approaches that are based on rough estimations that are extrapolated from first, basic simulations.

8.1 Identification of promising configurations for the development of magnetoresistive sensor devices

As introduced in chapter 7.3, different combinations of particle materials, size distributions, concentrations and gel viscosities can easily be simulated and compared concerning their magnetoresistive properties by performing hybrid molecular and spin dynamics simulations and subsequent pure spin dynamics hysteresis simulations. Therefore, a comparison of one particle type in two different matrix scenarios has been drawn that is published in [148]. Therein, a system of 192 cobalt particles similar to the previously

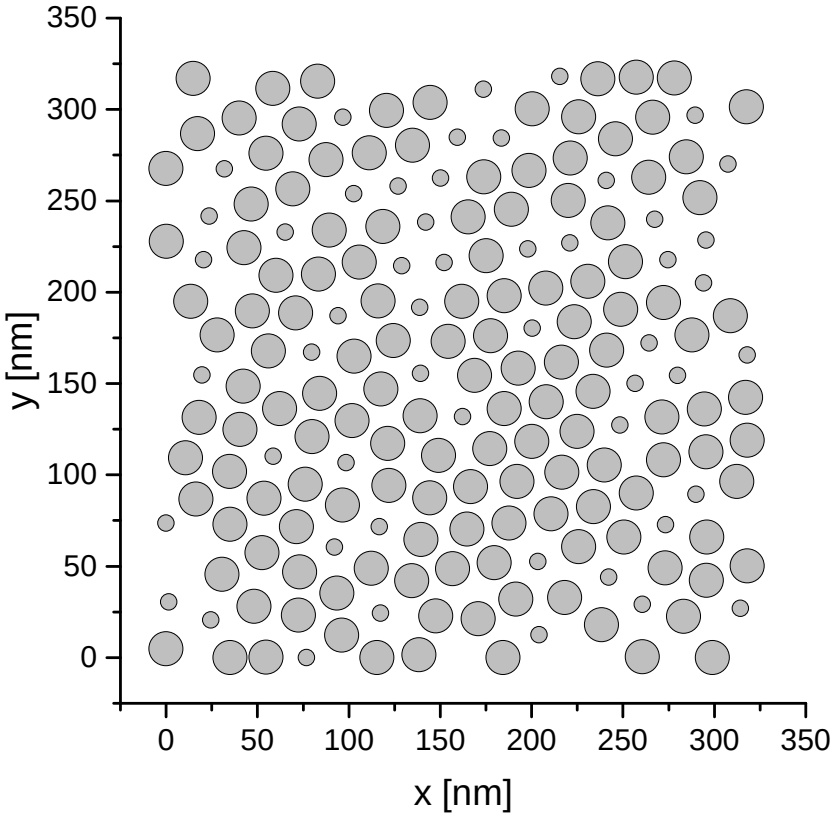

FIGURE 8.1: Model structure LT1 consisting of 192 Co nanoparticles that are distributed over an area of about 350 $nm \times 350$ nm. Here, 52 particles have diameters of 10 nm whereas 140 particles with diameters of 20 nm are used. The structures resembles the model structure AH41 but in contrast to AH41 two different particle diameters are used.

presented model structure AH41 is used in hybrid molecular and spin dynamics simulations and subsequent GMR effect estimations. In contrast to the monodisperse particles of AH41, here, two different particle sizes are used. The particle configuration which is named LT1 in the following is shown in figure 8.1.

In order to investigate the influence of the matrix viscosity on the GMR curve, the same structure LT1 is simulated twice. The first simulation considers the structure without any surrounding medium which corresponds to a matrix material with a dynamic viscosity of 0 $Pa \cdot s$. In a second simulation, the dynamic viscosity of the matrix is set to 0.11 $Pa \cdot s$ in order to mimic a 4% agarose matrix as proposed in the experimental studies that are published in [5, 6, 111]. Agarose is a seaweed extract that forms a hydrogel with a distinct liquid-solid transition that is commonly used for electrophoresis. Because of the liquid-solid transition properties and its electrical resistance, agarose is a good candidate for the application in printable, nanoparticular, magnetoresistive sensor systems.

At first, hybrid molecular and spin dynamics simulations of both systems, with and

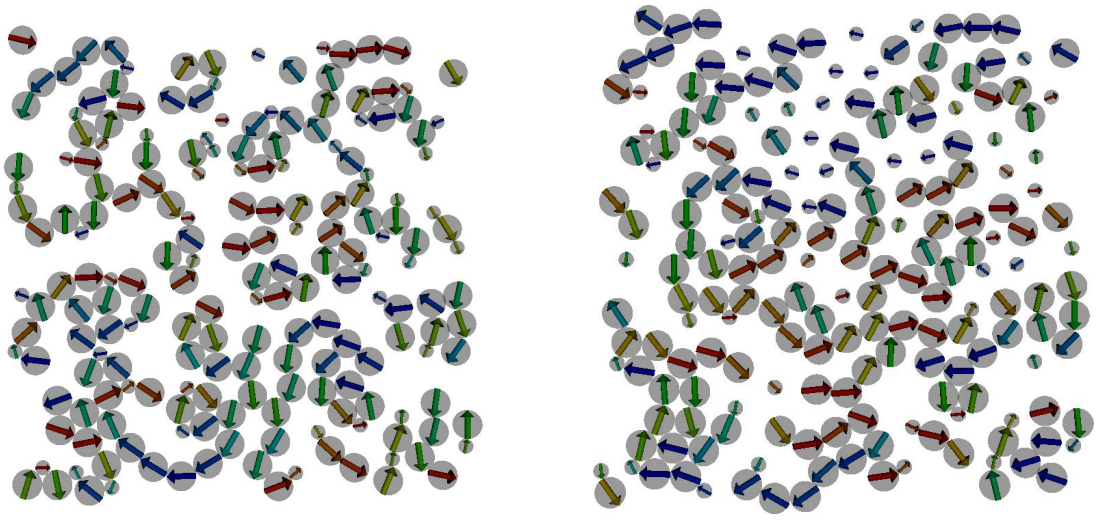

(a) (b)

FIGURE 8.2: Results of hybrid molecular and spin dynamics simulations of the model structure LT1 with and without a 4% agarose matrix. (a) The stable final configuration of the system without any matrix material is reached after $2 \cdot 10^7$ steps in time with a time step length of 10^{-14}, given in reduced Lennard-Jones units. The final configuration mainly consists of chains and particle rings that contain magnetic vortices. (b) For the system with an agarose matrix, the stable final configuration is obtained after $3 \cdot 10^7$ steps in time. The configuration, again, consist of particle chains and rings but in addition to that many small particles are isolated, in contrast to the system without matrix. This figure is reproduced from [148]. ©2015 IEEE

without agarose matrix, are performed from random initial configurations at room temperature. For both systems, a time step size of 10^{-14} τ (in reduced Lennard-Jones units) is chosen and spin dynamics runs are interposed every 10^4 steps in time. For the system without an agarose matrix, a total of $2 \cdot 10^7$ steps in time is required to reach a configuration that does not change with time any longer. For the system with the agarose matrix, the particles move slower due to the interaction with the gel matrix and therefore an extended simulation with $3 \cdot 10^7$ steps in time is required. For both systems, the hybrid simulation results in a particle configuration that consists of antiferromagnetically coupled chain fragments, ferromagnetically coupled areas, and particle rings that contain magnetic vortices as expected due to previous investigations as presented in chapter 7. The final configurations of hybrid simulations of both systems are shown in figure 8.2.

There is, however, an important difference between the final configurations of both systems. Qualitatively, for the system without an agarose matrix, nearly all particles are incorporated in chains and vortices and hardly any particles are isolated. In contrast to that, for the system with the 4 % agarose matrix many particles, especially small particles are isolated and therefore not included in the particle chains and vortices. As the only difference between these two systems is the presence or absence of the agarose

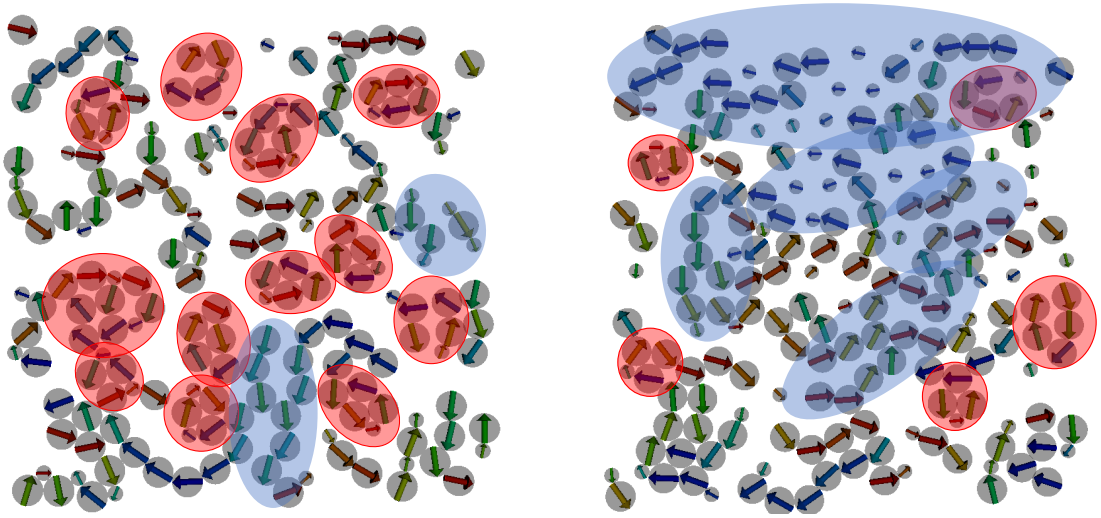

(a) (b)

FIGURE 8.3: Qualitative evaluation of the final configurations of hybrid molecular and spin dynamics simulations of the model structure LT1. (a) Simulation of LT1 without viscous matrix. The final configuration consists of a significant number of particle rings that contain magnetic vortices (red circles) and small ferromagnetically coupled areas (blue circles) and antiferromagnetically coupled chains. (b) With an agarose matrix, the simulation results in a structure that consists of a significantly reduced number of magnetic vortices (red circles). The viscous matrix inhibits particle motion and therefore, larger ferromagnetic areas and isolated small particles (blue circles) are present.

matrix that is incorporated in the model by the Stokes' drag (see chapter 3.2.2), the isolation of the particles must be due to the matrix viscosity. In this case, due to the viscous force of the matrix on the particles, the movement of the particles is slowed down and partially inhibited. Thus, as the smaller particles also have a smaller effective magnetic moment, the magnetic force is too small to overcome the viscous drag force. As a consequence, the number of particle vortices is reduced in favor of isolated particles and larger ferromagnetically coupled areas. At this point, the crucial question is whether isolated particles and ferromagnetically coupled areas are to be preferred or not. To answer this question, one has to define features that improve the GMR characteristics.

As introduced in chapter 2.2.3, the granular GMR effect can be considered as a relation of magnetic order and disorder. In figure 2.8 it is shown that a distinct GMR curve is the result of a distinct differentiation between the magnetically ordered configuration in saturation and the magnetically disordered configuration at the coercive field. As a consequence, in order to achieve good GMR properties, the magnetic configuration must be readily switchable in reasonable and experimentally producible external magnetic fields. In experimental investigations and theoretical studies by means of spin dynamics simulations, one can show that magnetic vortices are extremely stable to external magnetic

fields. Hence, in experimentally accessible external magnetic fields of a few thousand Oersted, these extremely stable vortex structures would not be switched at all. Therefore, the difference between the ordered and the disordered magnetic configurations is small compared to less stable particle configurations such as chains or ferromagnetically coupled areas. For this reason, stable vortices must be avoided in order to achieve good GMR properties. Going back to the topic of the two simulated systems under consideration, the viscosity of the gel matrix inhibits the particle movement and therefore a significant amount of isolated particles exists that, consequently, is not participating in stable vortices. In contrast to that, these isolated particles are very easily switchable even in small external magnetic fields. Hence, from theory, better GMR properties are expected for the system with the agarose matrix.

The assumption that a significant viscosity of the matrix material leads to better GMR characteristics can be supported by spin dynamics simulations. As presented in 7.2, the qualitative GMR characteristics can be derived from magnetization curves that can be obtained by means of pure spin dynamics simulations. For the system under consideration, the final configurations of the hybrid molecular and spin dynamics simulations of LT1 that are shown in figure 8.2 are used as input positions for two spin dynamics simulation. In order to mimic a conventional experimental situation, the external magnetic field is ramped up from $-0.2\ T$ to $+0.2\ T$ and back down to $-0.2\ T$. At the same time, the total magnetization of the system is observed. As shown in 7.2, with a reasonably chosen GMR effect amplitude, the GMR curve can be calculated from the magnetization curve according to equation 7.2. Here, in agreement with previous experiments (see figure 7.4), a GMR effect amplitude of $A_{GMR} = 20\%$ has been chosen for the evaluation. The magnetization curves of both systems are shown in figure 8.4 together with the resulting GMR curves. A comparison of the GMR curves of both systems is shown in figure 8.5. Here, it becomes apparent that a noticeable difference between the GMR curves of both systems can be identified. Whereas the GMR curve of the system without viscous matrix appears to be smeared out, the GMR curve of the system with the agarose matrix is characterized by clear and narrow peaks. For the application in magnetoresistive sensors, the sensor sensitivity is the most crucial parameter. For the system LT1, the sensitivity is increased by the application of an agarose matrix, manifesting in clearer GMR peaks. In the same manner, other particle materials and structures as well as different matrix materials can be investigated concerning their magnetoresistive properties. [148]

In summary, the simulation tool chain that involves hybrid molecular and spin dynamics simulations and subsequent GMR calculations provides an easy and cost-efficient way

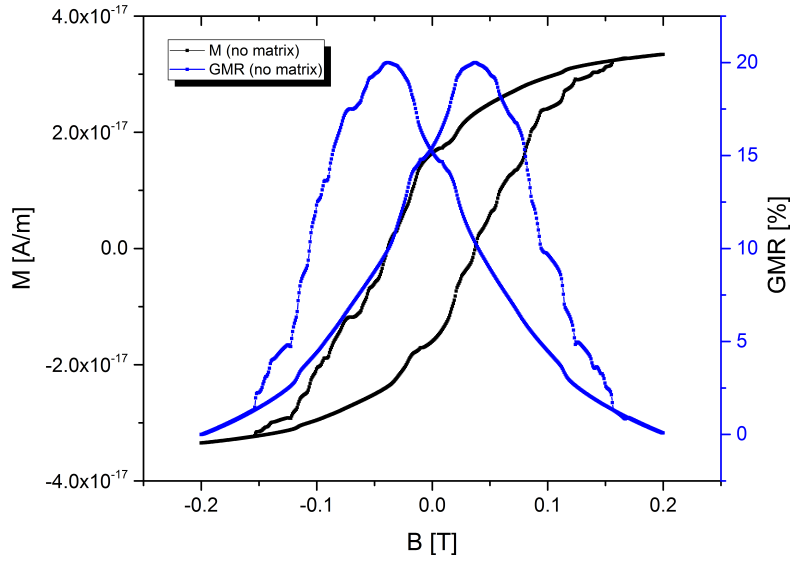

(a)

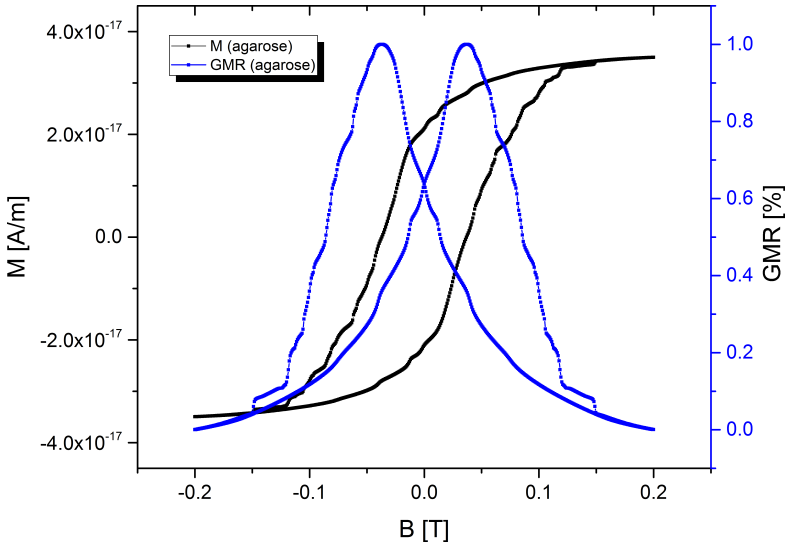

(b)

FIGURE 8.4: Results of spin dynamics simulations and subsequent GMR estimations of the structure LT1 (a) without and (b) with agarose matrix. The simulations are performed in an external magnetic field that is ramped up from $-0.2\ T$ to $+0.2\ T$ and back down to $-0.2\ T$. The resulting magnetization curves are shown in black. By means of equation 7.2, a qualitative estimation of the GMR curve (blue) can be obtained. Here, a GMR effect of 20% is assumed.

to identify promising combinations of magnetic particle materials, particle size distributions, particle concentrations and matrix material viscosities. Here, an exemplary investigation of the influence of the matrix viscosity on the GMR effect has been shown for a simple model system LT1 that contains 192 cobalt particles with diameters of 10 nm and 20 nm. It is shown that the topological differences of the structures with and without an agarose matrix result in different GMR characteristics. Thus, it is possible to make recommendations for further experimental investigations. At the same time,

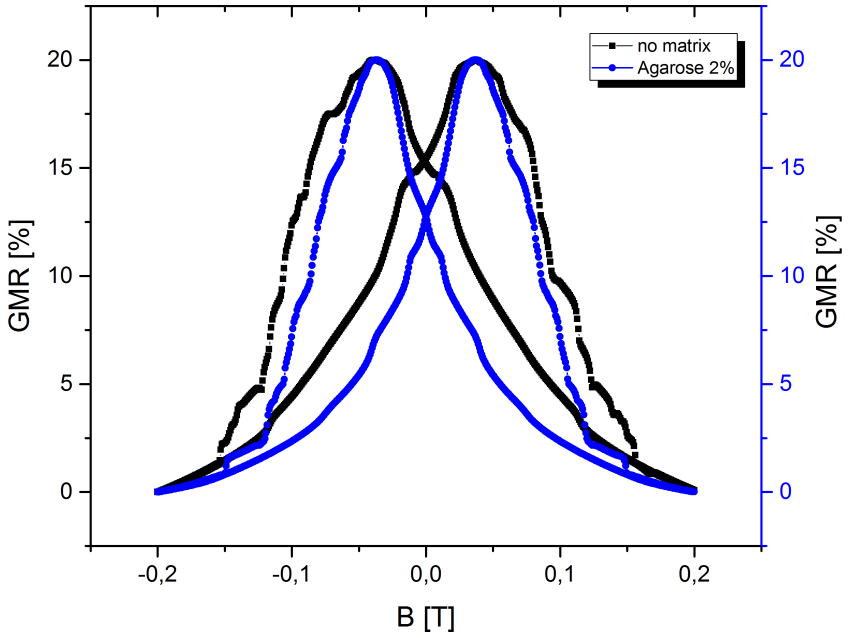

FIGURE 8.5: Comparison of the calculated GMR curves of the final configurations of the model structure AH41 without (a) and with agarose matrix (b). For the system with the agarose matrix, the GMR curve shows clear, narrow peaks, whereas the GMR curve of the system without matrix the peaks appear more smeared out. In agreement with previous considerations, the viscosity of the matrix material plays a crucial role for the GMR characteristics of systems of magnetic particles in gel matrices. This figure is taken from [148]. ©2015 IEEE

the single magnetic moment orientations can be monitored. As this is not possible in experiments, additional information can be generated by these simulations. In addition to that, the formulation of general rules for the design of nanoparticular magnetoresistive systems is enabled by this method.

8.2 Investigation of three-dimensional structures

As introduced in the previous chapters, ensembles of magnetic nanoparticles in viscous conductive matrices are particularly suitable for printable, low-cost magnetoresistive sensor devices for various applications. Therefore, quasi two-dimensional arrays of particles are prepared. In the course of the investigations of this work, small three-dimensional ensembles have been studied to test the algorithm and for rather didactic purposes. Surprisingly, very interesting results have been obtained that are presented in the following sections. With these results, novel and pioneering experiments may be predicted.

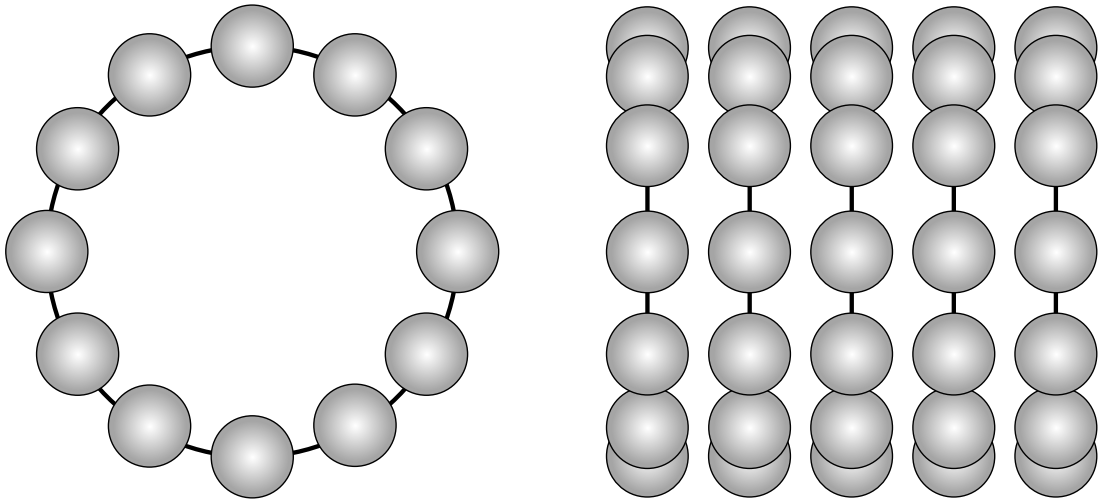

(a) (b)

FIGURE 8.6: Sketch of the tubular particle structure. The tube consists of 5 rings each containg 12 particles with diameters of 100 nm in a circular arrangement. The tube measures 500 nm in diameter whereas the separate rings are placed 125 nm apart. (a) Front view of the tube showing one particle ring. (b) Side view showing the positioning of the particle rings.

8.2.1 Nanoparticle tube

As an extension to the validation problem that is presented in chapter 6.5, here, equal rings are combined into a three-dimensional tubular structure. Therefore, five rings are assembled, each consisting of 12 cobalt particles with diameters of 100 nm. The diameter of each ring measures 500 nm. For the tube, the rings are positioned at a distance of 125 nm to the next ring. The particle configuration is shown true to scale in figure 8.6. Here, a zero viscosity matrix is assumed. For this structure, a complete, hybrid molecular and spin dynamics simulation is performed. Therefore, a molecular dynamics time step size of $dt = 1 \cdot 10^{-12}$ given in reduced Lennard-Jones units must be chosen. As previously introduced, the molecular dynamics part of the simulation is performed at room temperature which corresponds to a thermal energy of $T = 414.195 \cdot 10^{-23}$, given in reduced Lennard-Jones units again. A total of $5 \cdot 10^6$ molecular dynamics steps is required to drive the structure into a configuration that does not change with time any longer. After every 10^4 steps in time, a full spin dynamics run is intercalated. Therefore, 10^4 time steps with a step length of 10^{-14} s are performed at $T = 0$ K. The final configuration of the tubular particle arrangement is shown in figure 8.7(b). This stable configuration consists of connected, antiferromagnetically oriented particle chains in a zigzag arrangement. Instead of a distinct tube, the self-assembling process of the magnetic particles results in a slightly conical, tubular structure that is made of chains instead of rings.

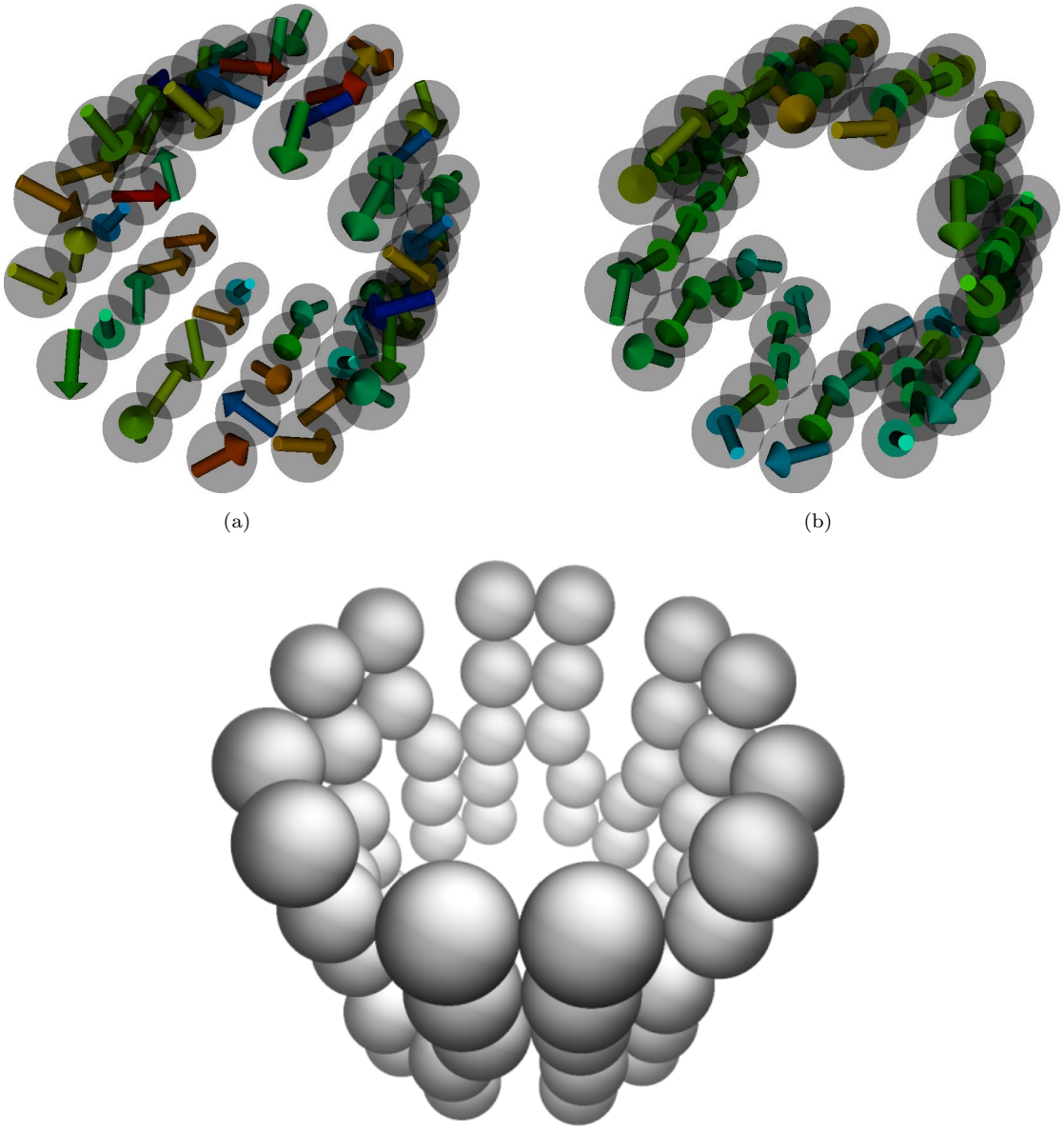

(a) (b)

(c)

FIGURE 8.7: Hybrid molecular and spin dynamics simulation of a tubular arrangement of cobalt nanoparticles in a matrix with zero viscosity according to the schematic representation in figure 8.6. (a) Initial particle positions and random magnetic moment orientations. (b) Final configuration of particle positions and magnetic moment orientations. In contrast to the initial configuration, the final structure obtains a slightly conical shape consisting of antiferromagnetically oriented chains. (c) Rotated view of the final configuration. To provide a clearer view of the structure the magnetic moment orientations are neglected here. It becomes apparent that the final configuration consists of connected particle chains in a zigzag arrangement.

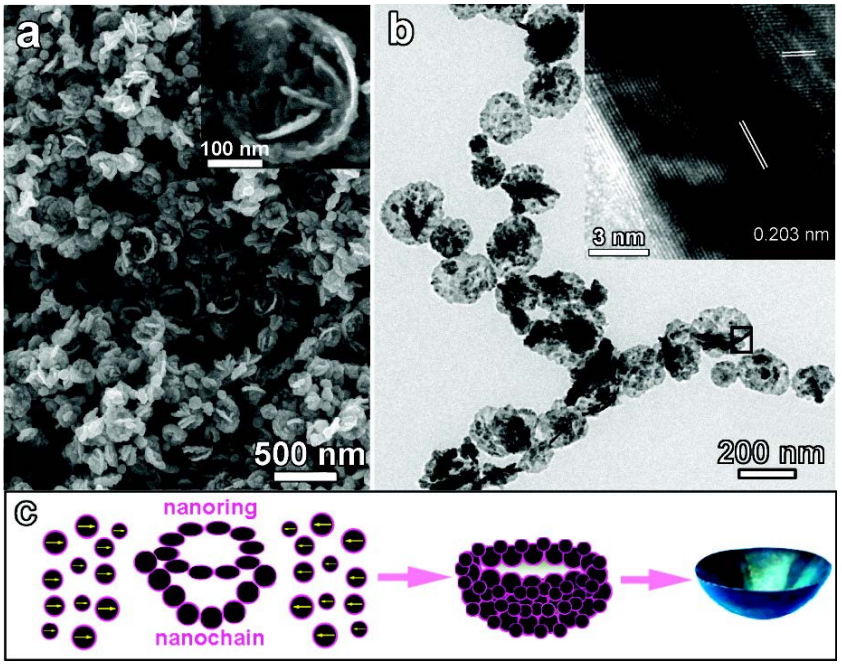

FIGURE 8.8: (a) SEM image of Ni bowls. The inset shows a typical bowl. (b) TEM image of Ni bowls with HRTEM image inserted corresponding to the marked frame in (b). (c) Illustration for the growth mechanism of Ni bowls. Reprinted with permission from [149]. Copyright 2011 American Chemical Society

The slightly conical shape of the tube resembles a bowl. There is technical interest in bowl-shaped nanostructures because of their outstanding properties concerning superhydrophobicity [150], optical properties [151], and particular phase behavior [152]. As reported in [149], the synthesis of bowl-shaped nanostructures is still challenging and one possible synthesis route is presented. The authors propose a growth mechanism that is shown in figure 8.8(c). This route could be retraced with the hybrid molecular and spin dynamics method. In addition to that, it is possible to optimize the particle material and surrounding medium material combination by means of simulation. Here, an enhancement of the bowl-shape can be found for a similar system with a reduced number of rings. Instead of combining five similar rings, three rings are combined to strengthen the shape of the bowl. The particle material and diameter, the diameter of the rings and the distance between the rings corresponds to the parameters that are chosen for the configuration of five rings. The simulation results are shown in figure 8.9. It becomes apparent that the shape of the bowl is much more pronounced than for the system that initially consists of five rings. To sum up, hybrid molecular and spin dynamics simulations can be used to retrace and explain mechanism that lead to the self-assembly of bowl-shaped nanostructures. Moreover, the simulation results can be used to identify suitable particle materials and properties of the surrounding medium.

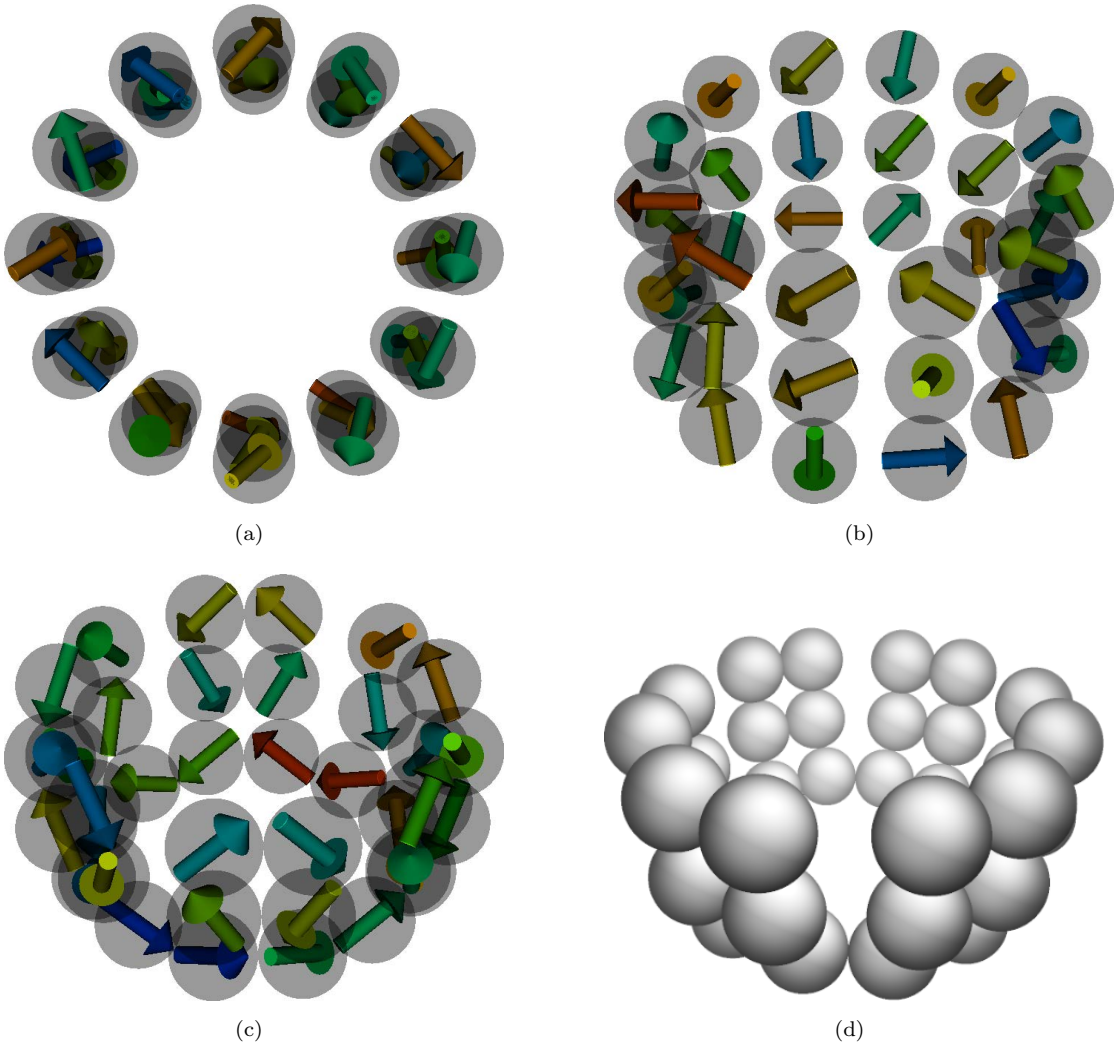

(a) (b)

(c) (d)

FIGURE 8.9: Hybrid molecular and spin dynamics simulation results of a tubular configuration that consists of three rings each containing 12 cobalt particles similar to the configuration of five rings that is shown in figure 8.7: (a) front view of the initial configuration with randomly oriented magnetic moments of the particles, (b) tilted view of the initial configuration, (c) final, bowl-shaped configuration and (d) representation of the final configuration with hidden magnetic moment orientations.

8.2.2 Nanoparticle cube

A very regular self-assembly process can be identified in the case of a perfectly cubical arrangement of eight cobalt particles with diameters of 100 nm in a zero-viscosity surrounding medium at room temperature. The edges of the fictitious cube measure 250 nm. As expected, the magnetic particles are attracted until they make contact. Hence, the resulting stable configuration again is a cubical arrangement that consists of two particle squares that contain magnetic vortices with opposite orientations. Figure 8.10 shows the inital and the final configuration of the particle positions together with the magnetic moment orientations.

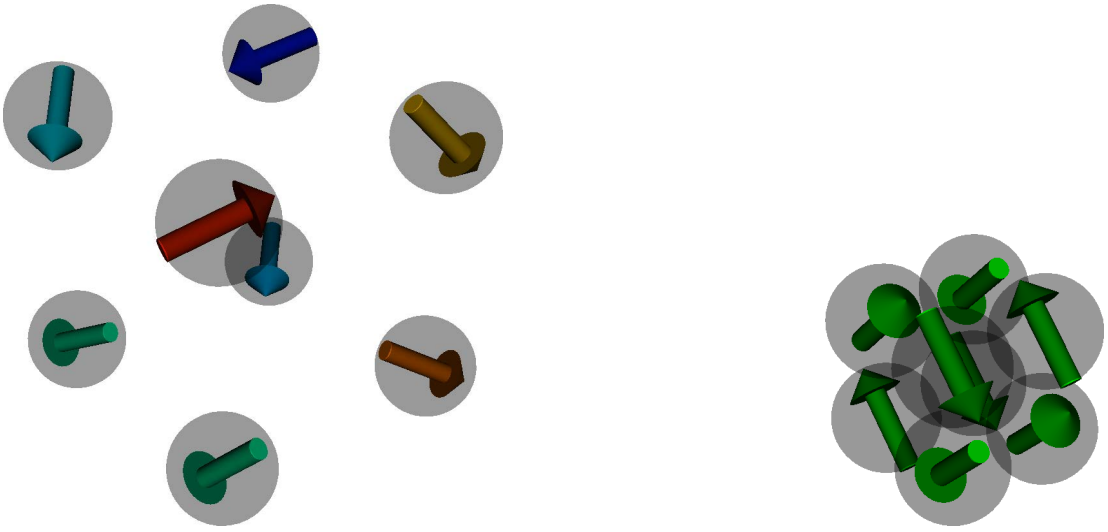

(a) (b)

FIGURE 8.10: Hybrid molecular and spin dynamics simulation of a cubical arrangement of 8 cobalt nanoparticles according to the schematic representation in figure 8.6. (a) Initial particle positions and random magnetic moment orientations. (b) Final configuration of particle positions and magnetic moment orientations. Due to the magnetic dipole-dipole interactions between the particles, the magnetic nanoparticles attract each other resulting in a densely-packed cubical arrangement.

A very interesting observation can be made by surveying the same cubical particle arrangement with an additional particle that is placed at a randomly chosen position on one face of the cube. It has to be noted that for the observation that is presented in the following, an artificially high magnetic dipole-dipole contribution was assumed for test purposes. Here, the magnetic dipole-dipole energy is increased by a factor of 10^4. Nevertheless, these results are remarkable and maybe could be reproduced experimentally for a different material combination at a different temperature.

The initial configuration for this simulation is shown in figure 8.11(a). The cobalt particles again have diameters of 100 nm and the edges of the fictitious cube measure 250 nm. The fictitious cube edges are shown as red lines to guide the eye. The self-assembly process of the cubic particle arrangement with the additional asymmetric defect particle results in a low energy configuration that consists of a ring and an approximately perpendicular, curved chain fragment at the center of the ring as outlined in figure 8.11(g). This state is reached after about 50% of the total number of steps in time of the simulation. This configuration can be reproduced for different simulation parameters. After the assembly process is completed, two different scenarios can occur. In the first scenario, the curved chain fragment rotates rapidly inside the particle ring while the ring performs a wave-like motion. In the second, opposed scenario, the ring rotates slowly around the chain fragment which, however, corresponds to the same situation. The rotation does

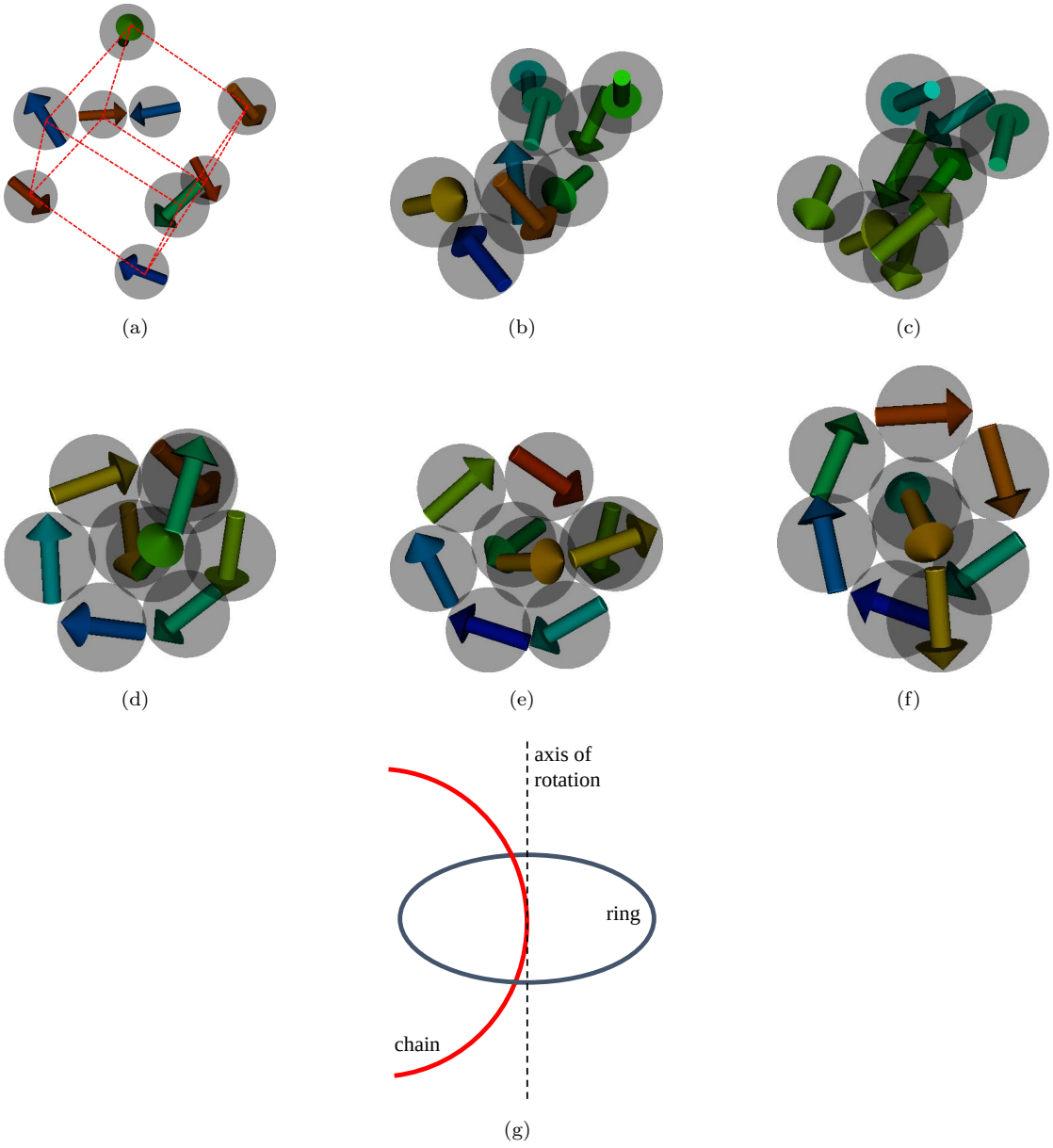

FIGURE 8.11: Visualization of the self-assembly process of an initially cubical arrangement of 8 cobalt particles with diameters of 100 nm similar to the configuration shown above. Here, an additional particle is included at a randomly chosen position. In total, $15 \cdot 10^7$ hybrid simulation time steps have been performed. The stable rotation starts at about 50% of the total number of time steps. (a) Inital particle position and magnetic moment orientations. The edges of the fictitious cube are shown in red to guide the eye. (b) Intermediate configuration after 5% of the time steps. (c) Intermediate configuration after 10% of the time steps. (d)-(f) Stable configuration consisting of a particle ring and a curved chain fragment. Here, the chain fragment rotates clockwise inside the ring. (g) Schematic representation of the ring and chain configuration.

not stop, even for very long simulation times. Hence, the question arises if the first law of thermodynamics is violated because the system seems to endlessly produce energy. The rotation is shown in figure 8.11(d-f). In fact, as the system is directly connected to the Nosé-Hoover thermostat of the molecular dynamics algorithm, there is evidence that energy is transferred to the system artificially. These fluctuations can be monitored indirectly by measuring the total magnetic energy of the system during the simulation. Indeed, it is a characteristic property of the applied Nosé-Hoover thermostat to generate periodical oscillations of the system's energy. By definition, the Nosé-Hoover thermostat does not strictly fix the temperature but allows for fluctuations in order to keep the *average* temperature constant. Because the particle ensemble consists of a very small number of particles, the fluctuations do not cancel out. Hence, large energy fluctuations are downright expected. However, these very energy fluctuations can likewise be generated in experimental situations by the application of "heat pulses". As a preliminary conclusion, the particular rotation of the particle ensemble can be attributed to energy fluctuations that are characteristic for the Nosé-Hoover thermostatting of small systems. Nevertheless, as these fluctuations can be reproduced experimentally, the system still shows remarkable behavior that should be focus for further investigations.

After the self-assembly process, the unidirectional rotation can be explained similar to a *Brownian motor* that has been previously presented in the literature [153–156]. One could argue that directed motion is only accessible in the presence of a temperature gradient which brings us back to the very early days of Brownian motion theory [157–160]. However, it has been shown in [154] that for far from equilibrium energy fluctuations, directed motion can be generated in an asymmetric potential as already predicted at the beginning of the 20th century. A characterization of a Brownian motor can be found in [153]. This characterization can be transferred to the magnetic nanoparticle system that is considered here.

The curved chain fragment and the ring form an energetically favorable state of the particle ensemble. The magnetic moments of the particles that are incorporated in the ring are oriented along the circumference of the ring. At the same time, the magnetic moments of the chain particles are oriented along the chain direction, i.e. upwards or downwards. As a consequence, the interaction of the ring and the chain by means of their magnetic dipole-dipole interactions can only lead to a unidirectional motion of the chain relative to the ring and vice versa. Due to the rotation of the chain and the wave-like motion of the ring, an asymmetrical potential is given. To emphasize the asymmetrical characteristics, the total magnetic energy of the system is evaluated in figure 8.12. Therein, the saw tooth shape of the magnetic energy in the rotating state of the system is shown. It becomes apparent that only very small energy fluctuations

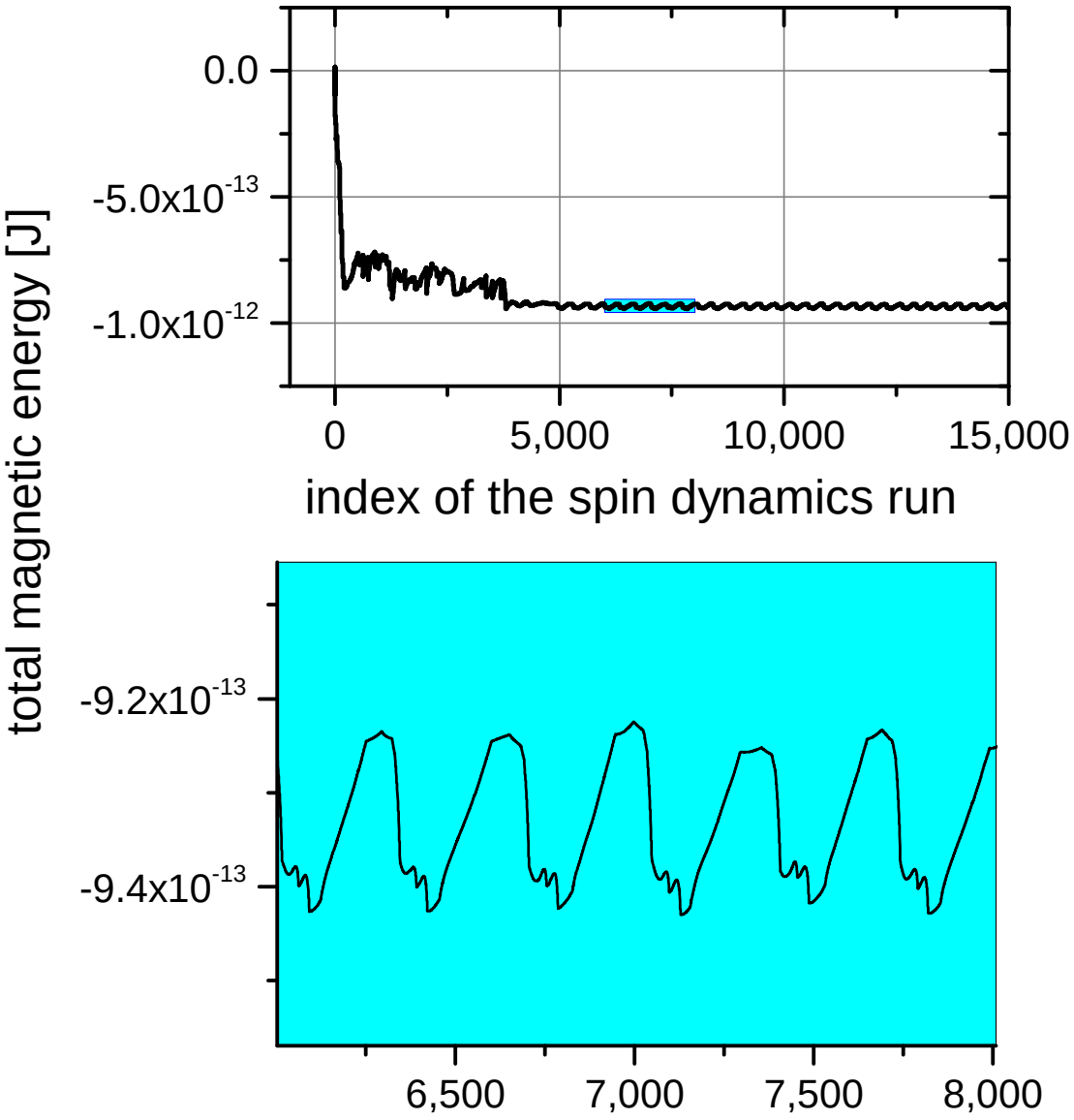

FIGURE 8.12: The total magnetic energy of the initially cubic particle arrangement with one additional particle. All the magnetic dipole-dipole energy contributions are summed up after every intercalated spin dynamics run. Here, these energies are plotted over the index of the respective spin dynamics run. Starting from a high energy of the initial configuration, the energy is gradually reduced until the stable configuration consisting of ring and chain is reached. As the rotation of the chain inside the ring starts, very small fluctuations in the magnetic energy can be observed. These fluctuations have an asymmetric saw tooth profile which is characteristic for a so-called Brownian motors [153]. One segment of the saw tooth profile in the rotating state of the system in the upper graph (blue) is displayed enlarged in the lower graph.

are required to drive the system out of its current state and rotate the chain relative to the ring by one section of the ring. Hence, this magnet particle-chain system can be compared to a ratchet mechanism.
It has to be noted that this is only a first, rough description of the recent findings and further investigations have to be carried out in the future.

8.3 Printed containers for magnetic spheres

As predicted by the previously presented simulations, small, three-dimensional ensembles of magnetic particles in liquids provide an interesting topic for experimental investigations. Therefore, one has to find a way to precisely position the particles in the liquid and simultaneously release them to start the self-assembly process. It must be noted that the suggestions that are made in this section are yet to be worked out and therefore, only rough ideas can be given here.
A first, simple approach for the investigation of interacting magnetic dipole self-assembly could be to use macroscopic magnetic spheres of various materials that can be purchased with different diameters from about 2 mm upwards. These magnetic spheres are mostly made of $Nd_2Fe_{14}B$ which is a common material for permanent magnets for industrial and private use. The density of $Nd_2Fe_{14}B$ is $400\frac{kg}{m^3}$. Thus, these magnetic spheres do not float on most liquids. In order to study self-assembling processes of magnetic macrospheres on water, one has to enable floating of these spheres on the water surface. This could be realized by incorporating the magnetic spheres in containers that are made of floating materials such as wood, cork, or plastic. For this approach, it is conceivable that spherical plastic containers are fabricated by means of 3D printing techniques. The containers could be designed to include the magnetic sphere at its center in order to obtain a central magnetic moment. In addition to that, air pockets could be designed to enable stable floating of the container. For the observation of the magnetic moment orientations, the magnetic moment orientation of the fixed magnetic spheres could be marked on the outside of the container.
With these encapsulated, floating magnetic spheres, one would be able to study self-assembly processes of arrangements of magnetic moments on a larger scale. Obviously, this method is restricted to two-dimensional particle arrangements. In addition to that, interface effects must be taken into account. Nevertheless, a very simple and efficient way to study small numbers of particles is given here.

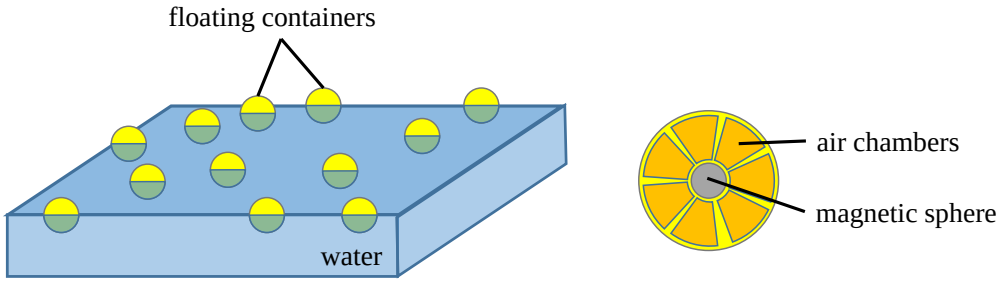

FIGURE 8.13: Sketch of suggested experimental setup for the investigation of two-dimensional magnetic particle arrangements. Instead of magnetic nanoparticles, macroscopic magnetic spheres are investigated. To realize floating magnets, the magnetic spheres are placed inside of plastic containers with air chambers.

8.4 Particle positioning via DNA-functionalization

As presented in [161] magnetic nanoparticles are frequently used in biotechnological and medical applications for therapy, imaging, and diagnostics. One important task is to deliver genes and drugs to specific locations in the body, e.g. to tumor locations for the magnetic hyperthermia of cancer tissue. In addition to that, magnetic nanoparticles find application in magnetic resonance imaging (MRI) and magnetic immunobeads [162]. For most of these applications, it is required to bind different kinds of molecules to magnetic particles that can be used for guiding mechanisms or to ensure biocompatibility. For this reason, the magnetic particles are commonly coated by biomolecules such as antibodies, amino acids, sugars or deoxyribonucleic acid (DNA), thus, forming nanobiocomposite materials [12].

According to [163], DNA can be carrier of information, can be characterized by molecular recognition, is physicochemically and mechanically stable and may form building blocks that can precisely be manipulated by hybridization and enzymatic processes. Therefore, DNA is a good candidate for the positioning of magnetic nanoparticles. One possible approach for the precise positioning of nanoparticles via DNA is presented in [164, 165]. Therefore, DNA patterns are prepared on chemically modified surfaces by nanoliter dispensing devices. By functionalization of the nanoparticles with complementary DNA, as shown in figure 8.14, a nanoparticle pattern can be produced that follows the shape of the DNA pattern. As DNA can easily be modified and different types can be used at the same time, it is possible to create complex patterns. The DNA binding can be broken by heating up the sample above the melting temperature. At this temperature, the DNA double-strands are separated into single strands because the bonds between the bases are broken up. Therefore, the release of bound nanoparticles can be directed by means of temperature.

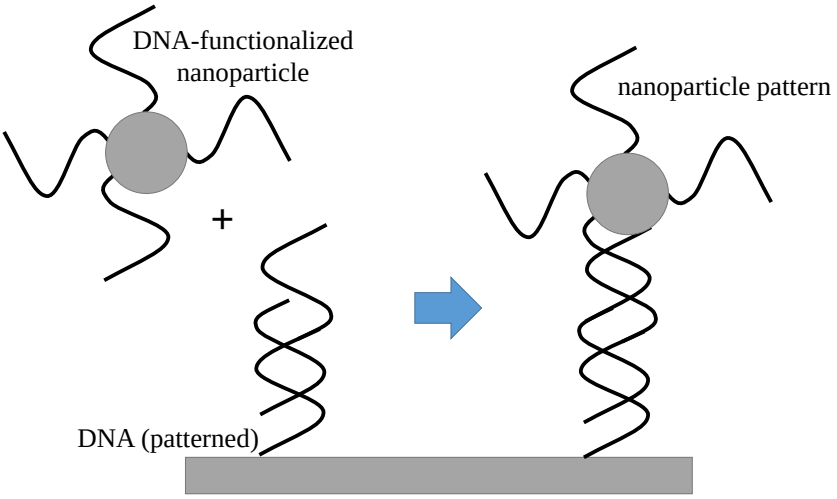

FIGURE 8.14: Schematic representation of the precise positioning of nanoparticles by dip-pen nanolithography. Therefore, DNA strands are placed on a surface by a nanoliter dispensing device. By functionalization of nanoparticles with complementary DNA, a nanoparticle pattern can be produced that follows the shape of the DNA pattern. [164, 165]

To apply the DNA-based nanoparticle positioning approach to the systems that are introduced in the previous sections of this chapter, one would be able to create patterned ensembles of magnetic particles by attaching DNA strands of required length to a functionalized substrate. With this approach, it would be possible to precisely position three-dimensional systems. The self-assembly process can easily be triggered by heating up the sample above the melting temperature of the DNA.

8.5 Encapsulation of magnetic particles in liquid metals

As presented previously in this chapter, for the experimental investigation of self-assembling magnetic moments, a macroscopic approach with floating magnetic spheres could be used. Because the density of the magnetic sphere is much higher than the density of most liquids, floating containers are required. Taking this idea further, systems of magnetic particles and liquid matrices with high densities could provide an interesting framework for further studies. High-density liquids are liquid metals. The term *liquid metal* is attributed to metals that are liquid at room temperature with mercury being the most prominent example with a melting temperature of $-38,83°C$. Other metallic elements with comparable properties are francium, gallium, caesium, and their alloys. Eutectic gallium-indium (EGaIn) with 75% gallium and 25% indium is a frequently used liquid metal alloy with a melting temperature of about 15.5°C [166]. EGaIn is a commercially available, electrically conductive liquid metal with a low toxicity. One particular feature of EGaIn is its ability to rapidly form a thin gallium oxide skin that

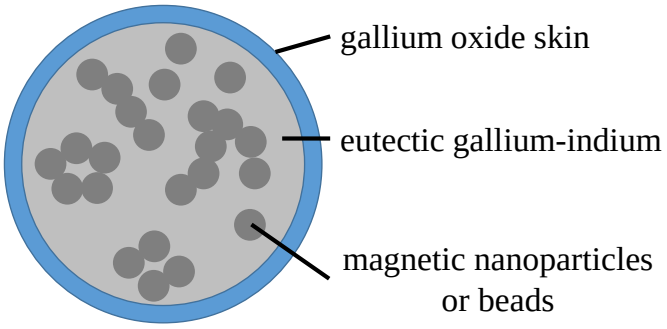

FIGURE 8.15: Schematic representation of possible experimental situation. Magnetic nanoparticles are mixed in liquid, eutectic gallium-indium at room temperature and a sphere of the mixture is formed with a syringe. Because gallium is highly reactive to oxygen, a skin of gallium oxide rapidly forms around the sphere which prevents the bulk material from further oxidization. Hence, the magnetic particles are free to move while being encapsulated in a low-viscosity liquid.

protects the bulk material from further oxidation and that mechanically stabilizes the structure. Thus, EGaIn can be used to print free-standing, stable microstructures such as wires or spheres [167].

In a possible experimental setup, magnetic particles could be included in the EGaIn matrix and the properties of the EGaIn could be used to form or print well-defined structures of the mixture. Afterwards, a gallium oxide skin forms around the structure which provides mechanical stability and at the same time ensures that the bulk EGaIn stays liquid. Hence, with this method one is able to create stable structures of liquid metals with oxide skins that contain magnetic particles. Due to the liquid metal core of the structures, the magnetic particles are able to move freely and self-assembly processes as well as interactions with external magnetic fields could be studied. Because the EGaIn structures are opaque, simulations could provide, again, crucial information about the particle microstructure and the magnetic moment orientations.

8.6 Suggestions for further experimental investigations summary

In conclusion, the hybrid molecular and spin dynamics method that is presented in this thesis can be applied to arbitrary ensembles of magnetic particles. Therefore, it provides a cost-efficient way for the investigation of suitable material combinations for gel-based GMR sensor devices. In addition to that, even systems that are currently not accessible experimentally can be investigated concerning their self-assembly properties and theoretically interesting systems can be identified. In doing so, prospective experimental activities can be motivated.

9 Conclusion and outlook

In summary, a novel, hybrid method for the simulation of self-assembly processes of interacting magnetic nanoparticles in viscous matrices has been presented in this work. In general, the mechanical and the magnetic degrees of freedom of the system have to be considered simultaneously. In this work, it has been shown that the relevant relaxation time scales of the mechanical and magnetic degrees of freedom are separated by several orders of magnitude for realistic particle diameters and matrix viscosities. Based on this separation of the time scales, a hybrid simulation process has been developed. Therefore, the system is initialized with given particle positions and random magnetic moment orientations. In a first step, the spin equations of motion are solved for a small step in time while the particle positions are assumed to be fixed. This is done by means of spin dynamics. In the next step, the new magnetic moment orientations are used together with the initial particle positions to solve the mechanical equations of motion by means of molecular dynamics for another small step in time. These steps are repeated until a predefined number of steps in time is reached. In doing so, one is able to investigate the time development of arbitrary ensembles of magnetic nanoparticles in viscous matrices. The trajectories and the magnetic moment orientations can be observed at the same time, providing detailed insight in the self-assembly process that cannot be provided experimentally. In addition to that, it has been shown that model structures can be designed to mimic real structures that are prepared experimentally. The microstructure can be revealed in detail by means of three-dimensional reconstruction techniques. With these reconstructions, the positions and diameters of all particles in a system can precisely be determined and used as input for hybrid simulations. In order to reduce the computational effort, model structures with a reduced number of particles can be designed. In this work, it has been shown that general features of real systems can be reproduced with these simple model structures very well. With the methods that are presented in this work, all stages of the experimental sensor preparation can be considered. Experimentally, the sensor is prepared by immersing the magnetic particles in the

liquid gel and placing the particle-gel mixture on a substrate. In the liquid state of the gel, the particles are free to move. Therefore, a self-assembly process takes place that is driven by the magnetic interactions between the particles and the viscous interactions between the particles and the gel. The self-assembly stops when a local energy minimum of the particle configuration is reached or when the gel matrix is dried out. This preparation stage corresponds to the hybrid molecular and spin dynamics simulation. Hence, one is able to investigate the preparation of the particle-gel system and observe the self-assembly process in detail. The actual GMR measurement takes place in the solid state of the gel where the particle positions are fixed. This stage can be considered by pure spin dynamics simulations. These resulting magnetization curves can finally be used to extract the GMR curves of the magnetic nanoparticle configurations. To sum up, one is able to observe the self-assembly of the magnetic particles and conclude from the resulting magnetization curves on the resulting GMR properties. Thus, general features can be identified that lead to good magnetoresistive properties and, hence, can be used to optimize the sensitivity of the final sensor devices. The same method can be used to investigate arbitrary three-dimensional particle configurations. In this work, it has been shown that interesting effects can be revealed by simulations and, thereby, promising experiments can be designed.

In addition to the suggestions for further experimental investigations, there are many open issues concerning the simulation method that should be addressed in the future. First and foremost, external magnetic fields should be included in the hybrid molecular and spin dynamics method. While homogeneous external magnetic fields can easily be included in the hybrid algorithm because there is no additional force contribution, for the consideration of inhomogeneous magnetic fields, an additional potential energy or force contribution must be defined in the molecular dynamics algorithm. Recent findings show that there is strong interest in the numerical investigation of the decoration of magnetic domains of recording media by magnetic nanoparticle ensembles in solution [168–170]. Therefore, high magnetic field gradients must be considered in the simulation. In addition to external magnetic fields, it would be important to include non-spherical particle geometries. Currently, hard sphere dynamics is realized by the Weeks-Chandler-Andersen (WCA) potential. The WCA potential is purely isotropic, i.e. the potential energy of the hard sphere interaction of two particles only depends on their (scalar) distance and not on their orientations. For this reason, only spherical objects can be considered by the hybrid method in its current form. For fundamental research as well as for technical applications, non-spherical, magnetic nanoparticles are of great importance. Just to mention a few examples, self-assembly processes of non-spherical nanoparticles result in sophisticated superstructures such as helical structures with promising technical applications [171–174]. In particular, cubic and cylindrical nanoparticles would be of great importance. From today's perspective, it is unclear

whether a hard particle potential formulation can be constructed for cubic and cylindrical particles. Instead of a potential function, an event-based collision detection could be implemented.

To conclude, with the realization of the hybrid molecular and spin dynamics method, the foundation for prospective theoretical and experimental research activities has been laid.

A

Hybrid molecular and spin dynamics program description

The program package that has been developed in the context of this thesis provides an environment for the simulation of interacting magnetic particles that are immersed in a viscous matrix. In general, magnetic particles with sizes on different scales can be simulated from magnetic nanoparticles over larger magnetic beads up to macroscopic, spherical magnetic objects. However, without loss of generality, only magnetic particles at the nanoscale are considered in this thesis. The self-assembly of magnetic nanoparticles in viscous matrices is driven by the magnetic dipole-dipole forces and forces due to the interplay of the moving particles and the viscosity of the matrix. In order to compute the trajectories of the particles, the magnetic and the mechanical degrees of freedom must be considered. As shown in this thesis, these two types of degrees of freedom can be treated separately because of their deviating time scales. Therefore, the magnetic and mechanical degrees of freedom are addressed by two different computer programs that are combined into one new hybrid molecular and spin dynamics simulation program. For the magnetic degrees of freedom, a classical spin dynamics algorithm is used that is documented in [75, 76]. A short description is given in chapter 3.1. For this algorithm, the magnetic particles are assumed to be fixed in space for a short period of time and the resulting magnetic moments are calculated. The mechanical degrees of freedom are addressed by the open-source molecular dynamic program package HOOMD-blue [107–109]. Again, a short summary of the main ingredients of the algorithm is given in chapter 3.2. The theoretical prerequisites and a description of the realization of the coupling is given in chapter 6. In addition to that, supplementary information about the modifications that have been made to both program packages as well as information about the relevant input and output files are given here.

A.1 Input files

In order to start a hybrid molecular and spin dynamics simulation with the program package that is presented here, three different input files are required, one to set up the spin dynamics simulation parameters, one file that contains the geometry data, and one file to set up the molecular dynamics simulation parameters and control the coupling of both algorithms. All of these files are simple, human readable text files.

Geometry data - *structure.xml*

The geometry parameters must be provided in one XML file. This file contains the size of the simulation box, the initial particle positions, diameters, and masses. Beforehand, the masses have to be calculated manually. The parameters are organized in so-called nodes resulting in a very clear representation of the system's geometry. Moreover, XML files are easily machine readable and can be generated and processed automatically in a very efficient way. With this geometry input format, the definition of a system is very clear and straightforward. In addition to that, snapshots of the system can be exported at different stages of the simulation in a similar format. As an example, the structure file of the ring-shaped validation problem of chapter 6.5 is shown in the following.

```
<?xml version="1.0" encoding="UTF-8"?>
<hoomd_xml version="1.5">
<configuration time_step="0" dimensions="2" natoms="12" >
<box lx="10000" ly="10000" lz="10000"/>
<position>
0 250 0
125 216.50635095 0
216.50635095 125 0
250 0 0
216.50635095 -125 0
125 -216.50635095 0
0 -250 0
-125 -216.50635095 0
-216.50635095 -125 0
-250 0 0
-216.50635095 125 0
-125 216.50635095 0
</position>
```

```
<orientation>
1 0 0 0 1 0 0 0 1 0 0 0 1 0 0 0 1 0 0 0 1 0 0 0
1 0 0 0 1 0 0 0 1 0 0 0 1 0 0 0 1 0 0 0 1 0 0 0
</orientation>
<type>
A A A A A A A A A A A A
</type>
<mass>
4.6600291e-18 4.6600291e-18 4.6600291e-18 4.6600291e-18
4.6600291e-18 4.6600291e-18 4.6600291e-18 4.6600291e-18
4.6600291e-18 4.6600291e-18 4.6600291e-18 4.6600291e-18
</mass>
<diameter>
100 100 100 100 100 100 100 100 100 100 100 100
</diameter>
</configuration>
</hoomd_xml>
```

Spin dynamics parameters - *mm.dat*

All parameters that are related to the spin dynamics part of the algorithm and, hence, the magnetic degrees of freedom are included in a textfile named *mm.dat*. In this file, the time step length, the total number of steps in time of each spin dynamics run, and the particle material's saturation magnetization are provided. In addition to that, the number of magnetic particles in the system is supplied. Furthermore, the temperature of the spin dynamics heat bath is defined in this file. As introduced in chapter 6.3, in this thesis, the spin temperature is set to 0 K. However, for further investigations, the temperature can be set to any finite value or time-dependent temperature profiles can be provided.

Molecular dynamics and coupling parameters - *input.hoomd*

The main input files has the file extension *.hoomd*. In this file, the parameters for the molecular dynamics part of the algorithm are recorded. The main parameters are the time step length, the total number of simulation time steps, the heat bath temperature and the interval length at which spin dynamics simulations are interposed. In addition to that, the physical system is defined here by composing the potential energy contributions such as the magnetic dipole-dipole interaction and the viscous contribution and

information on the kind of the ensemble is given. In principle, the entire range of functions of HOOMD-blue is available at this point. As this input file is written in Python, one can use the full functionality of Python here to set up complex simulations, precalculate values or define customized functions. In the following, the simulation script of the simulation of the ring for validation purposes is shown.

```
from hoomd_script import *

#read xml
system = init.read_xml(filename="12_p_circle.xml")

# specify between particle pairs
ddww = pair.ddww(r_cut=1000)
ddww.pair_coeff.set('A', 'A', mux=1.0, muy=1.0)

slj = pair.slj(r_cut=2**(1/6), d_max = 100.0)
slj.pair_coeff.set('A', 'A', epsilon=1.0, sigma=1.0)

dump.xml(filename="trajectory.dump", period=10000)
dump.dcd(filename="trajectory.dcd", period=10000)

# integrate at constant temperature
all = group.all();
integrator = integrate.mode_standard(dt=1e-12);
integrator = integrate.nvt(group=all, tau=1.0, T=414.1946439e-23)

# run 10000 time steps
run(0)
```

A.2 Output files

During and after the simulation four main output files are generated. Two of these files provide visualizations of the time development of the system whereas the other two files contain the values of different parameters.

Log file for total magnetic energies - *energy_log*

The total magnetic energies, i.e. the sum of all the magnetic dipole-dipole energy contributions of the system are evaluated in every spin dynamics run. Thus, one value is available for every spin dynamics interval of the simulation. These values are collected in the text file *energy_log*. With this file, one is able to monitor the time development of the magnetic energy over the complete simulation as shown in figure 8.12.

Log file for particle positions and magnetic moment orientations - *x3d_temp*

At every cross-over between the molecular and spin dynamics algorithm during the hybrid simulation, the particle positions and the magnetic moment orientations are communicated between the two programs. For further investigations and visualizations, all these values are stored in the text file *x3d_temp*. This file is usually very large but it provides a full description of the time development of the system.

Trajectory file - *output.dcd*

The hybrid molecular and spin dynamics program package that is presented here has no graphical user interface. Therefore, there is no real time visualization of the system and its time development. In order to get an impression of the system at any point in time during the simulation, a trajectory file *output.dcd* is generated and actualized after every specified interval of the hybrid simulation. This file can easily be imported into the open-source software VMD - Visual Molecular Dynamics [175]. VMD provides a program package for the three-dimensional visualization, animation, and analysis of biomolecular systems. The basic advantage comes with the fact that the visualization is available during the simulation run. Thus, the particle positions and the time development of the system can be examined at an early stage instead of waiting for a complete simulation run to finish. With VMD, the magnetic moment orientations cannot be displayed. As shown for example in figures 8.7(c) and 8.9(d) that have been generated by VMD, only the particles are displayed. The dcd file format is a binary format that results in very small filesizes.

Three-dimensional, interactive visualization - *output.x3d*

After the last step of a hybrid molecular and spin dynamics simulation is completed, the program collects all the values of the particle positions and the magnetic moment orientations that have been recorded in *x3d_temp* during the simulation. With these

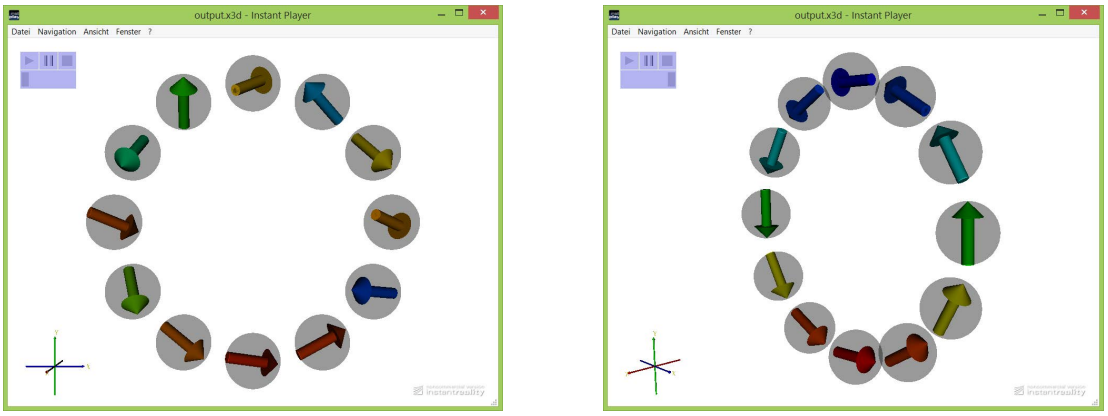

(a) (b)

FIGURE A.1: Visualization of the particle system with the x3d instantreality player [110]. The magnetic particles are displaced together with their magnetic moment orientations. The view can be rotated freely. (a) Front view and (b) rotated view.

files, an x3d file is constructed. The x3d files that are generated here are based on the x3d files that are generated in the standalone version of the spin dynamics code that was recently implemented by Irina Stockem. The x3d file format is a standard file format for the representation of three-dimensional computer graphics. Here, the Fraunhofer specifications are used for the visualization of the file in the *instantreality* player [110]. For the x3d visualization, the particle coordinates and magnetic moment orientations from the log file are taken and the player interpolates automatically between these values. The animation can be started directly from the file, intermediate stages can be frozen, and the view can be rotated at will.

A.3 Modifications to the spin dynamics algorithm

In contrast to the stand-alone version of the spin dynamics algorithm, here, the system is initialized from from a buffer file that is generated by HOOMD-blue. This file contains the particle positions and the effective magnetic moments. After the spin dynamics run is completed, the new magnetic moment orientations are written to the same buffer file.

A.4 Modifications to HOOMD-blue

The complete process of the hybrid molecular and spin dynamics simulations is controlled by HOOMD-blue, i.e. HOOMD-blue initializes the system, generates the files for the communication with the spin dynamics algorithm, starts the interposed spin dynamics runs, and finally generates the output files. Therefore, major modifications

to HOOMD-blue have been made. The workflow of the hybrid simulation is shown in figure 6.4. This workflow has been included in HOOMD-blue. In addition to that, the magnetic dipole-dipole interaction which is innately not included in HOOMD-blue has been included as well as a classical potential function formulation. Because the magnetic dipole-dipole interaction depends on the orientations of the magnetic moments, the handling of potential energy functions generally had to be modified. In HOOMD-blue, only scalar distances can be considered for the calculation of potential energy contributions. This has been changed to a vectorial representation of the interparticular distances throughout the program.

Bibliography

[1] M. N. Baibich, J. M. Broto, A. Fert, F. N. Van Dau, F. Petroff, P. Etienne, G. Crouzet, A. Friederich, and J. Chazelas. Giant Magnetoresistance of (001)Fe/(001)Cr Magnetic Superlattices. *Phys. Rev. Lett.*, 61:2472, 1988.

[2] G. Binasch, P. Grünberg, F. Saurenbach, and W. Zinn. Enhanced magnetoresistance in layered magnetic structures with antiferromagnetic interlayer exchange. *Phys. Rev. B*, 39:4828, 1989.

[3] J. Q. Xiao, J. S. Jiang, and C. L. Chein. Giant magnetoresistance in nonmultilayer systems. *Phys. Rev. Lett.*, 68:3749, 1992.

[4] A. E. Berkowitz, J. R. Mitchell, M. J. Carey, A. P. Young, S. Zhang, F. E. Spada, F. T. Parker, A. Hutten, and G. Thomas. Giant magnetoresistance in heterogeneous Cu-Co alloys. *Phys. Rev. Lett.*, 68:3745, 1992.

[5] J. Meyer, T. Rempel, M. Schäfers, F. Wittbracht, C. Müller, A. V. Patel, and A. Hütten. Giant magnetoresistance effects in gel-like matrices. *Smart Mater. Struct.*, 22:025032, 2013.

[6] J. Meyer. *Giant magnetoresistance effects in granular systems with gel matrices.* PhD thesis, Bielefeld University, Germany, November 2013.

[7] C. M. Hurd. Varieties of Magnetic Order in Solids. *Contemp. Phys.*, 23:469–493, 1982.

[8] J. M. D. Coey. *Magnetism and magnetic materials.* Cambridge Univ. Press, New York, NY, 2010.

[9] E. C. Stoner and E. P. Wohlfarth. A Mechanism of Magnetic Hysteresis in Heterogenous Alloys. *Philos. Trans. Roy. Soc. A*, 240:599–642, 1948.

[10] L. Néel. Théorie du trainage magnétique des ferromagnétiques au grains fin avec application aux terres cuites. *Ann. Geophys.*, 5:99–136, 1949.

[11] C. P. Bean and J. D. Livingstone. Superparamagnetism. *J. Appl. Phys.*, 30:120–129, 1959.

[12] S. P. Gubin, editor. *Magnetic Nanoparticles.* WILEY-VCH Verlag GmbH & Co. KGaA, 2009.

[13] D. L. Leslie-Pelecky and R. D. Rieke. Magnetic Properties of Nanostructured Materials. *Chem. Mater.*, 8:1770–1783, 1996.

[14] C. Kittel. Physical Theory of Ferromagnetic Domains. *Rev. Mod. Phys.*, 21:541–583, 1949.

[15] B. Barbara. Single-particle nanomagnetism. *Solid State Sci.*, 7:669–681, 2005.

[16] S. Chikazumi and C. D. Graham. *Physics of Ferromagnetism.* International Series of Monographs on Physics. Clarendon Press, 1997.

[17] G. Toulouse. Theory of the frustration effect in spin glasses: I. *Commun. Phys.*, 2:115, 1977.

[18] E. Ising. Beitrag zur Theorie des Ferromagnetismus. *Z. Phys.*, 31:253–258, 1925.

[19] R. Moessner and A. P. Ramirez. Geometrical frustration. *Physics Today*, 59:24–29, 2006.

[20] S. T. Bramwell and M. J. P Gingras. Spin Ice State in Frustrated Magnetic Pyrochlore Materials. *Science*, 294:1495–1501, 2001.

[21] C. Castelnovo, R. Moessner, and S. L. Sondhi. Magnetic monopoles in spin ice. *Nature*, 451:42–45, 2008.

[22] P. A. M. Dirac. Quantized Singularities in the Electromagnetic Field. *Proc. Roy. Soc. A*, 133:60–72, 1931.

[23] A. A. Minakov, I. A. Zaitsev, and U. I. Lesnih. Critical Behaviour of Magnetic Fluids Near Superparamagnetic-Dipole-Glass Transition. *J. Magn. Magn. Mater.*, 85:60–62, 1990.

[24] R. G. Palmer. Broken ergodicity. *Adv. Phys.*, 31:669–735, 1982.

[25] J. Villain. Insulating spin-glasses. *Z. Phys. B*, 33:31–42, 1979.

[26] K. Binder and A. P. Young. Spin glasses: Experimental facts, theoretical concepts, and open questions. *Rev. Mod. Phys.*, 58:801–976, 1986.

[27] V. Cabuil. Phase behavior of magnetic nanoparticles dispersions in bulk and confined geometries. *Curr. Opin. Colloid Interface Sci.*, 5:44–48, 2000.

[28] P. Poddar, T. Telem-Shafir, T. Fried, and G. Markovich. Dipolar interactions in two- and three-dimensional nanoparticle arrays. *Phys. Rev. B*, 66:060403, 2002.

[29] M. S. Seehra, H. Shim, P. Dutta, A. Mannivannan, and J. Bonevich. Interparticle interaction effects in the magnetic properties of NiO nanorods. *J. Appl. Phys.*, 97:10J509, 2005.

[30] S. L. Tripp, S. V. Pusztay, A. E. Ribble, and A. Wei. Self-Assembly of Cobalt Nanoparticle Rings. *J. Am. Chem. Soc.*, 124:7914–7915, 2002.

[31] J.-G. Zhu, Y. Zheng, and G. A. Prinz. Ultrahigh density vertical magnetoresistive random access memory. *J. Appl. Phys.*, 87:6668–6673, 2000.

[32] Yu. A. Koksharov, G. B. Khomutov, E. S. Soldatov, D. Suyatin, I. Maximov, L. Montelius, and P. Carlberg. Magnetostatic interactions in planar ring-like nanoparticle structures. *Thin Solid Films*, 515:731–734, 2006.

[33] A. Wei, T. Kasama, and R. E. Dunin-Borkowsky. Self-assembly and flux closure studies of magnetic nanoparticle rings. *J. Mater. Chem*, 21:16686–16693, 2011.

[34] P. Jund, S. G. Kim, D. Tománek, and J. Hetherington. Stability and Fragmentation of Complex Structures. *Phys. Rev. Lett.*, 74:3049–3052, 1995.

[35] W. Wen, F. Kun, K. F. Pál, D. W. Zheng, and K. N. Tu. Aggregation kinetics and stability of structures formed by magnetic microspheres. *Phys. Rev. E*, 59:R4758–R4761, 1999.

[36] A. Ghazali and J.-C. Lévy. Two-dimensional arrangements of magnetic nanoparticles. *Phys. Rev. B*, 67:064409, 2003.

[37] N. F. Mott. The Electrical Conductivity of Transition Metals. *Proc. R. Soc. Lond. Ser. A*, 153:699–717, 1936.

[38] N. F. Mott. The Resistance and Thermoelectric Properties of the Transition Metals. *Proc. R. Soc. Lond. Ser. A*, 156:368–382, 1936.

[39] E. Hirota, H. Sakakima, and K. Inomata. *Giant magneto-resistance devices.* Springer series in surface sciences, vol. 40. Springer, Berlin, Germany, 2002.

[40] T. Shinjo, editor. *Nanomagnetism and spintronics.* Elsevier, Amsterdam, The Netherlands, 2009.

[41] P. Grünberg, R. Schreiber, Y. Pang, M. B. Brodsky, and H. Sowers. Layered Magnetic Structures: Evidence for Antiferromagnetic Coupling of Fe Layers across Cr Interlayers. *Phys. Rev. Lett*, 57:2442–2445, 1986.

[42] S. S. P. Parkin, N. More, and K. P. Roche. Oscillations in exchange coupling and magnetoresistance in metallic superlattice structures: Co/Ru, Co/Cr, and Fe/Cr. *Phys. Rev. Lett*, 64:2304–2307, 1990.

[43] M. A. Rudermann and C. Kittel. Indirect Exchange Coupling of Nuclear Magnetic Moments by Conduction Electrons. *Phys. Rev.*, 96:99–102, 1954.

[44] T. Kasuya. A Theory of Metallic Ferro- and Antiferromagnetism on Zener's Model. *Prog. Theor. Phys.*, 16:45–57, 1956.

[45] K. Yosida. Magnetic Properties of Cu-Mn Alloys. *Phys. Rev.*, 106:893–898, 1957.

[46] M. Rührig, R. Schäfer, A. Hubert, R. Mosler, J. A. Wolf, S. Demokritov, and P. Grünberg. Domain Obervations on Fe-Cr-Fe Layered Structures: Evidence for a biquadratic coupling effect. *phys. stat. sol. (a)*, 125:635–656, 1991.

[47] M. D. Stiles. Interlayer exchange coupling. *J. Magn. Magn. Mater.*, 200:322–337, 1999.

[48] P. Bruno. Interlayer exchange coupling: a unified physical picture. *J. Magn. Magn. Mater.*, 121:248–252, 1993.

[49] M. D. Stiles. Exchange coupling in magnetic heterostructures. *Phys. Rev. B*, 48:7238–7258, 1993.

[50] N. Wiser. Phenomenological theory of the giant magnetoresistance of superparamagnetic particles. *J. Magn. Magn. Mater.*, 159:119–124, 1996.

[51] J. Korringa. On the calculation of the energy of a Bloch wave in a metal. *Physica*, 13:392–400, 1947.

[52] W. Kohn and N. Rostoker. Solution of the Schrödinger Equation in Periodic Lattices with an Application to Metallic Lithium. *Phys. Rev.*, 94:1111–1120, 1954.

[53] P. Zahn, J. Binder, I. Mertig, R. Zeller, and P. H. Dederichs. Origin of Giant Magnetoresistance: Bulk or Interface Scattering. *Phys. Rev. Lett.*, 80:4309–4312, 1998.

[54] E. E. Fullerton, M. J. Conover, J. E. Mattson, C. H. Sowers, and S. D. Bader. 150-Percent Magnetoresistance in Sputtered Fe/Cr(100) Superlattices. *Appl. Phys. Lett.*, 63:1699–1701, 1993.

[55] D. H. Mosca, F. Petroff, A. Fert, P. A. Schroeder, W. P. Pratt, and R. Laloee. Oscillatory Interlayer Coupling and Giant Magnetoresistance in Co/Cu Multilayers. *J. Magn. Magn. Mater.*, 94:L1–L5, 1991.

[56] S. S. P. Parkin, R. Bhadra, and K. P. Roche. Oscillatory Magnetic Exchange Coupling Through Thin Copper Layers. *Phys. Rev. Lett.*, 66:2152–2155, 1991.

[57] B. Dieny, V. S. Speriosu, S. Metin, S. S. P. Parkin, B. A. Gurney, P. Baumgart, and D. R. Wilhoit. Magnetotransport Properties of Magnetically Soft Spin-Valve Structures. *J. Appl. Phys.*, 69:4774–4779, 1991.

[58] C. Reig, M.-D. Cubells-Beltrán, and D. R. Muñoz. Magnetic Field Sensors Based on Giant Magnetoresistance (GMR) Technology: Applications in Electrical Current Sensing. *Sensors*, 9:7919–7942, 2009.

[59] J. P. Sebastiá, J. A. Lluch, J. R. L. Vizcaíno, and J. S. Bellon. Vibration detector based on GMR sensors. *IEEE Trans. Instrum. Meas.*, 58:707–712, 2009.

[60] S. Arana, N. Arana, R. Gracia, and E. Castaño. High sensitivity linear position sensor developed using granular Ag-Co giant magnetoresistances. *Sens. Actuat. A: Phys.*, 123:116–121, 2005.

[61] S. Arana, E. Castaño, and F. J. Gracia. High temperature circular position sensor based on a giant magnetoresistance nanogranular Ag_xCo_{1-x} alloy. *IEEE Sens. J.*, 4:221–225, 2005.

[62] A. J. López-Martín and A. Carlosena. Performance tradeoffs of three novel GMR contactless angle detectors. *IEEE Sens. J.*, 9:191–198, 2009.

[63] D. R. Baselt, G. U. Lee, M. Natesan, S. W. Metzger, P. E. Sheehan, and R. J. Colton. A biosensor based on magnetoresistance technology. *Biosens. Bioelectron.*, 13:731–739, 1998.

[64] J. C. Rife, M. M. Miller, P. E. Sheehan, C. R. Tamanaha, M. Tondra, and L. J. Whitman. Design and performance of GMR sensors for the detection of magnetic microbeads in biosensors. *Sensor. Actuat. A: Phys.*, 107:209–218, 2003.

[65] J. Schotter, P. B. Kamp, A. Becker, A. Puhler, G. Reiss, and H. Bruckl. Comparison of a prototype magnetoresistive biosensor to standard fluorescent DNA detection. *Biosen. Bioelectron.*, 19:1149–1156, 2014.

[66] D. L. Graham, H. A. Ferreira, and P. P. Freitas. Magnetoresistive-based biosensors and biochips. *Trends biotechnol.*, 22:455–462, 2004.

[67] Y. W. Jun, J. W. Seo, and J. Cheon. Nanoscaling laws of magnetic nanoparticles and their applicabilities in biomedical sensors. *Acc. Chem. Res.*, 41:179–189, 2008.

[68] K. H. Bae, M. Park, M. J. Do, N. Lee, J. H. Ryu, G. W. Kim, C. Kim, T. G. Park, and T. Hyeon. Chitosan oligosaccharide-stabilized ferrimagnetic iron oxide nanocubes for magnetically modulated cancer hyperthermia. *ACS Nano*, 6:5266–5273, 2012.

[69] S. D. Kong, W. Zhang, J. H. Lee, K. Brammer, R. Lal, M. Karin, and S. Jin. Magnetically Vectored Nanocapsules for Tumor Penetration and Remotely Switchable On-Demand Drug Release. *Nano Lett.*, 10:5088–5092, 2010.

[70] A. Weddemann, I. Ennen, A. Regtmeier, C. Albon, A. Wolff, K. Eckstädt, N. Mill, M. K.-H. Peter, J. Mattay, C. Plattner, N. Sewald, and A. Hütten. Review and outlook: from single nanoparticles to self-assembled monolayers and granular GMR sensors. *Beilstein J. Nanotechnol.*, 1:75–93, 2010.

[71] A. Weddemann, J. Meyer, and A. Hütten. Numerical Study of Nanoscaled Granular Giant Magnetoresistance Sensors for the Limit Case of Dipolar Coupled Nanoparticles. *JBAP*, 2:60–67, 2013.

[72] L. Teich, C. Schröder, J. Meyer, A. Hütten, C. Müller, and A. Patel. Efficient Calculation of Low Energy Configurations of Nanoparticle Ensembles for Magnetoresistive Sensor Devices by Means of Stochastic Spin Dynamics and Monte Carlo Methods. *Acta Phys. Pol. A*, 127:374–376, 2015.

[73] G. R. Nabiyouni. Design and Fabrication of Nanomagnetic Sensors Based on Electrodeposited GMR Materials. *Metrol. Meas. Syst.*, 16:519–529, 2009.

[74] B. Eickenber, J. Meyer, L. Helmich, D. Kappe, A. Auge, A. Weddemann, F. Wittbracht, and A. Hütten. Lab-on-a-Chip Magneto-Immunoassays: How to Ensure Contact between Superparamagnetic Beads and the Sensor Surface. *Biosensors*, 3:327–340, 2013.

[75] C. Schröder. *Numerische Simulationen zur Thermodynamik magnetischer Strukturen mittels deterministischer und stochastischer Wärmebadankopplung.* PhD thesis, Osnabrück University, Germany, November 1998.

[76] L. Engelhardt and C. Schröder. *Simulating Computationally Complex Magnetic Molecules.* World Scientific Publishers, Singapore, 2011.

[77] A. Bulgac and D. Kusnezov. Classical limit for lie algebras. *Ann. Phys.*, 199:187–224, 1990.

[78] J. Stöhr and H. C. Siegmann. *Magnetism: From Fundamentals to Nanoscale Dynamics*. Springer-Verlag, Berlin, Germany, 2006.

[79] L. Landau and E. Lifshitz. On the theory of magnetic permeability in ferromagnetic bodies. *Phys. Z. der Sow.*, 8:153–169, 1935.

[80] T. L. Gilbert. A Lagrangian formulation of the gyromagnetic equation of the magnetization field. *Phys. Rev.*, 100:1243, 1955.

[81] D. Wei. *Micromagnetics and Recording Materials*. SpringerBriefs in Applied Sciences and Technology. Springer, Berlin, Germany, 2012.

[82] M. E. Tuckerman. *Statistical Mechanics: Theory and Molecular Simulation*. Oxford University Press, 2010.

[83] A. Einstein. Über die von der Molekularkinetischen Theorie der Wärme Geforderte Bewegung von in Ruhenden Flüssigkeiten suspendierten Teilchen. *Ann. Phys.*, 17:549–560, 1905.

[84] P. Langevin. On the Theory of Brownian Motion. *C. R. Acad. Sci.*, 146:530–533, 1908.

[85] D. Wei. *The Langevin and Generalised Langevin Approach to the Dynamics of Atomic, Polymeric and Colloidal Systems*. Elsevier, Amsterdam, The Netherlands, 2007.

[86] W. T. Coffey, Y. P. Kalmykov, and J. T. Waldron. *The Langevin Equation: With Applications in Physics, Chemistry and Electrical Engineering*. World Scientific Publishing, Singapore, 1996.

[87] G. N. Milstein and M. V. Tretyakov. Numerical methods in the weak sense for stochastic differential equations with small noise. *SIAM J. Numer. Anal.*, 34:2142–2167, 1997.

[88] J. E. Jones. On the Determination of Molecular Fields. II. From the Equation of State of a Gas. *Proc. R. Soc. Lond. A*, 106(738):436–477, 1924.

[89] D. Frenkel and B. Smit. *Understanding Molecular Simulation*. Academic Press, Inc., Orlando, FL, USA, 2nd edition, 2001.

[90] D. C. Rapaport. *The Art of Molecular Dynamics Simulation*. Cambridge University Press, New York, NY, USA, 2nd edition, 2004.

[91] J. D. Weeks, D. Chandler, and H. C. Andersen. Role of Repulsive Forces in Determining the Equilibrium Structure of Simple Liquids. *J. Chem. Phys.*, 54:5237–5247, 1971.

[92] L. Verlet. Computer "Experiments" on Classical Fluids. I. Thermodynamical Properties of Lennard-Jones Molecules. *Phys. Rev.*, 159:98–103, 1967.

[93] P. Schofield. Computer simulation studies of the liquid state. *Comp. Phys. Comm.*, 5:17–23, 1973.

[94] D. E. Knuth. *The Art of Computer Programming, Volume 1 (3rd Ed.): Fundamental Algorithms*. Addison Wesley Longman Publishing Co., Inc., Redwood City, CA, USA, 1997.

[95] I. Newton. *Philosophiae naturalis principia mathematica*. J. Societatis Regiae ac Typis J. Streater, 1687.

[96] J. C. Butcher. *Numerical Methods for Ordinary Differential Equations*. John Wiley & Sons, New York, USA, 2003.

[97] R. W. Hockney and J. W. Eastwood. *Computer Simulations Using Particles*. Taylor & Francis, Inc., Bristol, PA, USA, 1988.

[98] W. H. Press, S. A. Teukolsky, W. T. Vetterling, and B. P. Flannery. *Numerical Recipes in C: The Art of Scientific Computing*. Cambridge University Press, New York, NY, USA, 2nd edition, 1992.

[99] W. C. Swope, H. C. Andersen, P. H. Berens, and K. R. Wilson. A computer simulation method for the calculation of equilibrium constants for the formation of physical clusters of molecules: Application to small water clusters. *J. Chem. Phys.*, 76(1):637–649, 1982.

[100] H. J. C. Berendsen and W.F. van Gunsteren. *Practical algorithms for dynamics simulations*. North-Holland Elsevier Science Publisher, Amsterdam, The Netherlands, 1987.

[101] H. C. Andersen. Molecular dynamics at constant temperatur and/or pressure. *J. Comp. Phys.*, 93:189–223, 1980.

[102] H. J. C. Berendsen, J. P. M. Postma, W. F. van Gunsteren, A. Dinola, and B. Haak. Molecular dynamics with coupling to an external heat bath. *J. Chem. Phys.*, 81:3684–3690, 1984.

[103] W. G. Hoover. Canonical dynamics: equilibrium phase-space distribution. *Phys. Rev. A*, 31:1695–1697, 1985.

[104] J. M. Thijssen. *Computational Physics*. Cambridge University Press, Cambridge, UK, 2007.

[105] K. Cho and J. D. Joannopoulos. Ergodicity and dynamical properties of constant-temperature molecular dynamics. *Phys. Rev. A*, 45:7089–7097, 1992.

[106] P. H. Hünenberger. Thermostat algorithms for molecular dynamics simulations. *Adv. Polym. Sci.*, 173:105–149, 1985.

[107] J. A. Anderson. Hoomd-blue. *http://codeblue.umich.edu/hoomd-blue*.

[108] J. A. Anderson, C. D. Lorenz, and A. Travesset. General purpose molecular dynamics simulations fully implemented on graphics processing units. *J. Comp. Phys.*, 227:5342–5359, 2008.

[109] J. Glaser, T. D. Nguyen, J. A. Anderson, P. Liu, F. Spiga, J. A. Millan, D. C. Morse, and S. C. Glotzer. Strong scaling of general-purpose molecular dynamics simulations on GPUs. *Comput. Phys. Commun.*, 192:97–107, 2015.

[110] The Fraunhofer Institute for Computer Graphics Research IGD. instantreality.org. *http://www.instantreality.org/story/what-is-it/*, (Accessed 13 August 2015).

[111] T. Rempel, J. Meyer, L. Teich, M. Gottschalk, K. Rott, D. Kappe, C. Schröder, and A. Hütten. Giant Magnetoresistance Effects in Gel-like Matrices: Comparing Experimental and Theoretical Data. *submitted for publication*, 2015.

[112] L. Teich, D. Kappe, T. Rempel, J. Meyer, C Schröder, and A. Hütten. Modeling of Nanoparticular Magnetoresistive Systems and the Impact on Molecular Recognition. *Sensors*, 15:9251–9264, 2015.

[113] Z. Budrikis, J. P. Morgan, J. Akerman, A. Stein, P. Politi, S. Langridge, C. H. Marrows, and R. L. Stamps. Disorder strength and field-driven ground state domain formation in artificial spin ice: experiment, simulation and theory. *Phys. Rev. Lett.*, 109:037203, 2012.

[114] X. Ke, J. Li, C. Nisoli, P. E. Lammert, W. McConville, R. F. Wang, V. H. Crespi, and P. Schiffer. Energy Minimization and ac Demagnetization in a Nanomagnet Array. *Phys. Rev. Lett.*, 101:037205, 2008.

[115] C. Phatak, A. K. Patford-Long, and O. Heinonen. Nanoscale structure of the magnetic induction at monopole defects in artificial spin-ice lattices. *Phys. Rev. B*, 83:174431, 2011.

[116] V. P. Antropov, M. I. Katsnelson, M. van Schilfgaarde, and B. N. Harmon. Ab Initio Spin Dynamics in Magnets. *Phys. Rev. Lett.*, 75:729–732, 1995.

[117] I. P. Omelyan, I. M. Mryglod, and R. Folk. Algorithm for Molecular Dynamics Simulations of Spin Liquids. *Phys. Rev. Lett.*, 86:898–901, 2001.

[118] P.-W. Ma and C. H. Woo. Large-scale simulation of the spin-lattice dynamics in ferromagnetic iron. *Phys. Rev. B*, 78:024434, 2008.

[119] P. Thibaudeau and D. Beaujouan. Thermostatting the atomic spin dynamics from controlled demons. *Physica A*, 391:1963–1971, 2012.

[120] M. J. Benítez Romero. *Self-assembled Magnetic Nanostructures: Synthesis and Characterization.* PhD thesis, Ruhr-Universität Bochum, Germany, December 2009.

[121] M. I. Bodnarchuk, M. V. Kovalenko, W. Heiss, and D. V. Talapin. Energetic and Entropic Contributions to Self-Assembly of Binary Nanocrystal Superlattices: Temperature as the Structure-Directing Factor. *J. Am. Chem. Soc.*, 132:11967–11977, 2010.

[122] S. Singamaneni, V. N. Bliznyuk, C. Binek, and E. Y. Tsymbal. Magnetic nanoparticles: recent advances in synthesis, self-assembly, and applications. *J. Mater. Chem.*, 21:16819–16845, 2011.

[123] V. Skumryev, S. Stoyanov, Y. Zhang, G. Hadhipanayis, D. Givord, and J. Nogués. Beating the superparamagnetic limit with exchange bias. *Nature*, 423:850–853, 2003.

[124] R. H. Kodama. Magnetic nanoparticles. *J. Magn. Magn. Mater.*, 200:359–372, 1999.

[125] U. Häfeli, W. Schütt, J. Teller, and M. (Eds.) Zborowski. *Scientific and Clinical Applications of Magnetic Materials.* Plenum, New York, USA, 1997.

[126] V. P. Antropov, M. I. Katsnelson, B. N. Harmon, M. van Schilfgaarde, and D. Kusnezov. Spin dynamics in magnets: Equation of motion and finite temperature effects. *Phys. Rev. B.*, 54:1019–1035, 1996.

[127] I. P. Omelyan, I. M. Mryglod, and R. Folk. Molecular dynamics simulations oof spin and pure liquids with preservation of all the conservation laws. *Phys. Rev. E*, 64:016105, 2001.

[128] I. P. Omelyan, I. M. Mryglod, and R. Folk. Construction of high-order force-gradient algorithms for integration of motion in classical and quantum systems. *Phys. Rev. E*, 66:026701, 2002.

[129] A. Satoh, R. W. Chantrell, G. N. Coverdale, and S. Kamiyama. Stokes dynamics simulations of ferromagnetic colloidal dispersions in a simple shear flow. *J. Colloid Interface Sci.*, 203:233–248, 1998.

[130] H. Morimoto, T. Maekawa, and Y. Matsumo. Brownian dynamics analysis of cluster structures and magnetic characteristics of ferromagnetic particles subjected to a shear flow. *Int. J. Mod. Phys. B*, 15:823–828, 2001.

[131] Z. Wang, C. Holm, and H. W. Müller. Molecular dynamics study on the equilibrium magnetization properties and structure of ferrofluids. *Phys. Rev. E*, 66:021405, 2002.

[132] P. Ilg, E. Coquelle, and S. Hess. Structure and rheology of ferrofluids: simulation results and kinetic models. *J. Phys. Condens. Mat.*, 18:S2757, 2006.

[133] A. Y. Polyakov, T. V. Lyutyy, S. Denisov, V. V. Reva, and P. Hänggi. Large-scale Ferrofluid Simulations on Graphics Processing Units. *Comp. Phys. Commun.*, 184:1483–1489, 2013.

[134] L. Teich and C. Schröder. Hybrid molecular and spin dynamics simulations for ensembles of magnetic nanoparticles for magnetoresistive systems. *accepted for publication*, 2015.

[135] B. Dünweg and A. J. C. Ladd. Lattice Boltzmann simulations of soft matter systems. *Adv. Polym. Sci.*, 221:89–166, 2009.

[136] M. Born and R. Oppenheimer. Zur Quantentheorie der Molekeln. *Ann. Phys.*, 389:457–484, 1927.

[137] G. K. Batchelor. Brownian diffusion of particles with hydrodynamic interaction. *J. Fluid. Mech.*, 74:1–29, 1976.

[138] A. P. Philipse. Notes on brownian motion. *http://userpages.umbc.edu/~dfrey1/ench630/philipse_notes_on_brownian_motion.pdf*, (Accessed 14 August 2015).

[139] W. B. Russel, D. A. Saville, and W. R. Schowalter. *Colloidal Dispersions*. Cambridge University Press, Cambridge, UK, 1995.

[140] B. Fischer, B. Huke, M. Lücke, and R. Hempelmann. Brownian relaxation of magnetic colloids. *J. Magn. Magn. Mater.*, 289:74–77, 2009.

[141] R. E. Rosensweig. *Ferrohydrodynamics*. Dover Publications Inc., Mineola, NY, USA, 2014.

[142] S. Thomas, N. Kalarikkal, A. M. Stephan, and B. Raneesh. *Advanced Nanomaterials: Synthesis, Properties and Applications.* CRC Press, Boca Raton, FL, USA, 2014.

[143] M. Lingenheil, Denschlag R., R. Reichold, and P. Tavan. The "Hot-Solvent/Cold-Solute" Problem Revisited. *J. Chem. Theory Comput.*, 4:1293–1306, 2008.

[144] R. Car and M. Parrinello. Unified Approach for Molecular Dynamics and Density-Functional Theory. *Phys. Rev. Lett.*, 55:2471–2474, 1985.

[145] D. Marx and J. Hutter. *Ab initio molecular dynamics: basic theory and advanced methods.* Cambridge University Press, Cambridge, UK, 2009.

[146] S. L. Tripp, R. E. Dunin-Borkowsky, and A. Wei. Flux Closure in Self-Assembled Cobalt Nanoparticle Rings. *Angew. Chem. Int. Ed.*, 42:5591, 2003.

[147] A. Wei. Calixarene-encapsulated nanoparticles self-assembly into funtional nanomaterials. *Chem. Commun.*, pages 1581–1591, 2006.

[148] L. Teich and C. Schröder. Numerical Investigation of the Magneto-Dynamics of Self-Organizing Nanoparticle Ensembles: a Hybrid Molecular and Spin Dynamics Approach. *IEEE T. Magn.*, PP:1, 2015.

[149] W. Zhou, L. Lin, D. Zhao, and L. Guo. Synthesis of Nickel Bowl-like Nanoparticles and their Doping for Inducing Planar Alignment of a Nematic Liquid Crystal. *J. Am. Chem. Soc.*, 133:8389–8391, 2011.

[150] J. C. Love, B. D. Gates, D. B. Wolfe, K. E. Paul, and G. M. Whitesides. Fabrication and Wetting Properties of Metallic Half-Shells with Submicron Diameters. *Nano Lett.*, 2:891–894, 2002.

[151] M. Marechal, R. J. Kortschot, A. F. Demiro, A. Imhof, and M. Dijkstra. Phase Behavior and Structure of a New Colloidal Model System of Bowl-Shaped Particles. *Nano Lett.*, 10:1907–1911, 2010.

[152] J. Liu, A. I. Maaroof, L. Wieczorek, and M. B. Cortie. Fabrication of Hollow Metal "Nanocaps" and Their Red-Shifted Optical Absorption Spectra. *Adv. Mater.*, 17:1276–1281, 2008.

[153] P. Reimann and P. Hänggi. Introduction to the physics of Brownian motors. *Appl. Phys. A*, 75:169–178, 2002.

[154] R. D. Astumian. Thermodynamics and Kinetics of a Brownian motor. *Science*, 276:917–922, 1997.

[155] R. D. Astumian and P. Hänggi. Brownian motors: Thermal motion combined with input energy gives rise to a channeling of chance that can be used to exercise control over microscopic systems. *Physics Today*, 55:33–39, 2002.

[156] P. Hänggi, F. Marchesoni, and F. Nori. Brownian motors. *Ann. Phys.*, 14:51–70, 2005.

[157] J. C. Maxwell. *Theory of Heat*. Longmans, Green and Co., London, UK, 1872.

[158] M. Smoluchowski. Experimentell nachweisbare, der üblichen Thermodynamik widersprechende Molekularphänomene. *Phys. Z.*, 13:1069–1080, 1912.

[159] L. Brillouin. Can the Rectifier Become a Thermodynamical Demon? *Phys. Rev.*, 78:627, 1950.

[160] R. P. Feynman, R. B. Leighton, and M. Sands. *The Feynman Lectures*. Addison-Wesley, Reading, MA, USA, 1963.

[161] S. C. McBain, H. H. P. Yiu, and J. Dobson. Magnetic nanoparticles for gene and drug delivery. *Int. J. Nanomedicine*, 3:169–180, 2008.

[162] S. Mornet, S. Vasseur, F. Grasset, and E. Duguet. Magnetic nanoparticle design for medical diagnosis and therapy. *J. Mater. Chem.*, 14:2161–2175, 2004.

[163] G. Schmid. *Nanoparticles: from Theory to Applications*. Wiley, Weinheim, Germany, 2010.

[164] C. M. Niemeyer, B. Ceyhan, S. Gao, L. Chi, S. Peschel, and U. Simon. Site-selective immobilization of gold nanoparticles functionalized with DNA oligomers. *Colloid Polym. Sci.*, 279:68–72, 2001.

[165] L. M. Demers, S. J. Park, T. A. Taton, Z. Li, and C. A. Mirkin. Orthogonal Assembly of Nanoparticle Building Blocks on Dip-Pen Nanolithographically Generated Templates of DNA. *Angew. Chem. Int. Ed.*, 40:3071–3073, 2001.

[166] M. D. Dickey, R. C. Chiechi, R. J. Larsen, E. A. Weiss, D. A. Weitz, and G. M. Whitesides. Eutectic Gallium-Indium (EGaIn): A Liquid Metal Alloy for the Formation of Stable Structures in Microchannels at Room Temperature. *Adv. Funct. Mater.*, 18:1097–1104, 2008.

[167] C. Ladd, J. H. So, J. Muth, and M. D. Dickey. 3D Printing of Free Standing Liquid Metal Microstructures. *Adv. Mater.*, 25:5081–5085, 2013.

[168] J. Henderson, S. Shi, S. Cakmaktepe, and T. M. Crawford. Pattern transfer nanomanufacturing using magnetic recording for programmed nanoparticle assembly. *Nanotechnology*, 23:185304, 2012.

[169] L. Ye, B. Qi, T. Pearson, Y. Cordeau, O. T. Mefford, and T. M. Crawford. Real time monitoring of superparamagnetic nanoparticle self-assembly on surfaces of magnetic recording media. *J. Appl. Phys.*, 115:17B513, 2014.

[170] A. R. Mohtasebzadeh, L. Ye, and T. M. Crawford. Magnetic Nanoparticle Arrays Self-Assembled on Perpendicular Magnetic Recording Media. *Int. J. Mol. Sci.*, 16:19769–19779, 2015.

[171] G. Singh, H. Chan, A. Baskin, E. Gelman, N. Repnin, P. Král, and R. Klajn. Self-assembly of magnetite nanocubes into helical superstructures. *Science*, 345:1149–1153, 2014.

[172] J. C. Love, A. R. Urbach, M. G. Prentiss, and G. M. Whitesides. Three-Dimensional Self-Assembly of Metallic Rods with Submicron Diameters Using Magnetic Interactions. *J. Am. Chem. Soc.*, 125:12696–12697, 2003.

[173] M. Chen, T. Pica, Y.-B. Jiang, Li. P., K. Yano, J. P. Liu, A. K. Datye, and H. Fan. Synthesis and Self-Assembly of fcc Phase FePt Nanorods. *J. Am. Chem. Soc.*, 129:6348–6349, 2007.

[174] M. Tanase, D. M. Silevitch, A. Hultgren, L. A. Bauer, P. C. Searson, G. J. Meyer, and D. H. Reich. Magnetic trapping and self-assembly of multicomponent nanowires. *J. Appl. Phys.*, 91:8549, 2002.

[175] University of Illinois at Urbana Champaign. VMD - Visual Molecular Dynamics. *http://www.ks.uiuc.edu/Research/VMD*.

[176] J. H. Rodrigues, L. A. S. Mol, W. A. Moura-Melo, and A. R. Pereira. Efficient demagnetization protocol for the artificial triangular spin ice. *Appl. Phys. Lett.*, 103:092403, 2013.

[177] M. Kardar. *Statistical Physics of Fields*. Cambridge University Press, 2007.

[178] J. A. Ewing. On the Production of Transient Electric Currents in Iron and Steel Conductors by Twisting them when Magnetised or by Magnetising them when Twisted. *Proc. Roy. Soc.*, 33:21–23, 1881.

[179] A. P. Guimarães and I. S. Oliveira. *Magnetism and magnetic resonance in solids*. John Wiley & Sons, INC., New York, NY, 1998.

[180] C. Reig, S. Cardoso, and S. Mukhopadhyay. *Giant Magnetoresistance (GMR) Sensors: From Basis to State-of-the-Art Applications*. Smart Sensors, Measurement and Instrumentation, Vol. 6. Springer-Verlag, Berlin, Germany, 2013.

[181] C. Lacroix, P. Mendels, and F. Mila, editors. *Introduction to Frustrated Magnetism: Materials, Experiments, Theory (Springer Series in Solid-State Sciences)*. Springer, 2011.

[182] T. Shinjo and H. Yamamoto. Large Magnetoresistance of Field-Induced Giant Ferrimagnetic Multilayers. *J. Phys. Soc. Jpn.*, 59:3061–3064, 1990.

[183] D. Karnaushenko, D. Makarov, Y. Chenglin, R. Streubel, and O. G. Schmidt. Printable giant magnetoresistive devices. *Adv. Mater.*, 24:4518–4522, 22.

[184] H. Yan, Z. Chen, Y. Zheng, C. Newman, J. R. Quinn, F. Dötz, and M. Kastler. A high-mobility electron-transporting polymer for printed transistors. *Nature*, 457:679–687, 2009.

[185] A. C. Arias, J. D. MacKenzie, I. McCulloch, J. Rivnay, and A. Scalleo. Materials and Applications for Large Area Electronics. *Chem. Rev.*, 110:3–24, 2010.

[186] D. Karnaushenko, D. Makarov, M. Stöber, D. D. Karnaushenko, S. Baunack, and O. G. Schmidt. High-Performance Sensorics for Printable and Flexible Electronics. *Adv. Mater.*, 27:880–885, 2015.

[187] M. Kaltenbrunner, T. Sekitani, J. Reeder, T. Yokota, K. Kuribara, T. Tokuhara, M. Drack, R. Schwödiauer, I. Graz, S. Bauer-Gogonea, S. Bauer, and T. Someya. An ultra-lightweight design for imperceptible pastic electronics. *Nature*, 499:458–463, 2013.

[188] S. D. Bond, B. J. Leimkuhler, and B. B. Laird. The Nosé-Poincaré method for constant temperature molecular dynamics. *J. Comp. Phys.*, 151:114–134, 1999.

[189] K. N. (Ed.) Trohidou. *Magnetic Nanoparticle Assemblies*. Taylor & Francis, Boca Raton, FL, USA, 2015.

[190] M. P. Allen and D. J. Tildesley. *Computer Simulation of Liquids*. Clarendon Press, Oxford, UK, 1987.

[191] A. G. Pershina, A. E. Sazanov, and V. D. Filimonov. Magnetic nanoparticles - DNA interactions: design and applications of nanobiohybrid systems. *Russ. Chem. Rev.*, 83:299–322, 2014.

Danksagung

Zu guter letzt möchte ich mich für die Unterstützung bedanken, die ich von so vielen Seiten bei der Erstellung dieser Arbeit bekommen habe.

Zuerst bedanke ich mich für fachliche Unterstützung, organisatorische Hilfe, Motivation und die Chance, mich intensiv mit einem so spannenden Thema auseinander zu setzen bei Prof. Dr. Christian Schröder (Fachhochschule Bielefeld) und Prof. Dr. Andreas Hütten (Universität Bielefeld). Ich habe mich in beiden Arbeitsgruppen zu Hause gefühlt und habe die gute Kooperation sehr geschätzt.

Diese Arbeit ist im Rahmen der Forschungskooperation *MoRitS - Modellbasierte Realisierung intelligenter Systeme in der Nano- und Biotechnologie* im Teilprojekt 1 *Magnetoresistive Sensorik auf der Basis von Nanopartikeln in neuartigen Siliziumgelen* entstanden. Mein Dank gilt allen Mitarbeitern, die zum Gelingen des Teilprojekts beigetragen haben, allen voran Dr. Judith Meyer. Für eine gelungene Kooperation danke ich auch Dr. Christiane Müller und Marianne Bartke. Ebenfalls aus den Reihen der Forschungskooperation MoRitS danke ich Sabine Wolf-Homeyer, Bettina Krammer und Vanessa Homburg für Unterstützung abseits des Fachlichen. Für die finanzielle Unterstützung danke ich dem Ministerium für Innovation, Wissenschaft und Forschung des Landes Nordrhein-Westfalen.

Auf Seiten der Fachhochschule Bielefeld danke ich allen Weggefährten der Arbeitsgruppe Computational Materials Science & Engineering. Insbesondere danke ich Irina Stockem für die tolle Bürogemeinschaft, die Vorarbeiten zur Visualisierung im x3d-Format und die Unterstützung bei der Anpassung im Rahmen dieser Arbeit, gemeinsame Reisen,

Fehlersuche und noch vieles mehr. Desweiteren danke ich Thomas Hilbig für seine Hilfe bei allen Fällen von PC- und Clusterproblemen sowie organisatorischen Fragen. Ebenfalls danken möchte ich Simon Bekemeier für die Portierung der Molekulardynamik in die aktuellste Version und die Implementierung in der virtuellen Maschine. Daniel Kleinehanding danke ich für die große Unterstützung bei der Grundzustandssuche und seine außerordentliche Zuverlässigkeit bei seinen Projektarbeiten und der Masterarbeit.

In der AG Dünne Schichten & Physik der Nanostrukturen der Universität Bielefeld danke ich Thomas Rempel für die gute Zusammenarbeit und die Möglichkeit der Verzahnung von Theorie und Experiment. Für die große Hilfe bei allen Formalitäten der Promotion danke ich Elke Siedlaczek.

Last but not least: Mein unendlicher Dank gilt meinem Mann Matthias, meinen Eltern Petra und Dietmar sowie meinen Geschwistern Merle und Niklas von denen jeder auf seine Art und Weise dazu beigetragen hat, dass ich diese Arbeit schreiben konnte.